FABRICATION AND CHARACTERIZATION OF

POROUS SHAPE MEMORY ALLOYS

A Thesis

by

LUKE EDWARD PENROD

Submitted to the Office of Graduate Studies of
Texas A&M University
in partial fulfillment of the requirements for the degree of

MASTER OF SCIENCE

December 2003

Major Subject: Aerospace Engineering

FABRICATION AND CHARACTERIZATION OF

POROUS SHAPE MEMORY ALLOYS

A Thesis

by

LUKE EDWARD PENROD

Submitted to Texas A&M University
in partial fulfillment of the requirements
for the degree of

MASTER OF SCIENCE

Approved as to style and content by:

_____
Dimitris C. Lagoudas
(Chair of Committee)

_____
Luis San Andres
(Member)

_____
Ibrahim Karaman
(Member)

_____
Thomas C. Pollock
(Member)

_____
Walter E. Haisler
(Head of Department)

December 2003

Major Subject: Aerospace Engineering

ABSTRACT

Fabrication and Characterization of Porous Shape Memory Alloys. (December 2003)

Luke Edward Penrod, B.S., Texas A&M University

Chair of Advisory Committee: Dr. Dimitris C. Lagoudas

This work details an investigation into the production of porous shape memory alloys (SMAs) via hot isostatic press (HIP) from pre-alloyed powders. HIPing is one of three main methods for producing porous SMAs, the other two are conventional sintering and self-propagating high-temperature synthesis (SHS). Conventional sintering is characterized by its long processing time at near atmospheric pressure and samples made this way are limited in porosity range. The SHS method consists of pre-loading a chamber with elemental powders and then initiating an explosion at one end, which then propagates through the material in a very short time. HIPing provides a compromise between the two methods, requiring approximately 5 hours per cycle while operating in a very controlled environment. The HIPing method gives fine control of both temperature and pressure during the run which allows for the production of samples with varying porosity as well as for fine-tuning of the process for other characteristics. By starting with pre-alloyed powder, this study seeks to avoid the drawbacks while retaining the benefits of HIPing with elemental powders.

In an extension of previous work with elemental powders, this study will apply the HIP method to a compact of pre-alloyed powders. It is hoped that the use of these powders will limit the formation of alternate phases as well as reducing oxidation formed during preparation. In addition, the near-spherical shape of the powders will encourage an even pore distribution. Processing techniques will be presented as well as a detailed investigation of the thermal and mechanical properties of the resulting material.

To Aleisha, my wife, best friend and greatest supporter.

ACKNOWLEDGMENTS

First, I would like to thank to Dr. Lagoudas for his advice and insight into the many technical problems that we faced. His guidance gave this project life and gave me the inspiration to complete it. My committee members Dr. Pollock, Dr. Karaman and Dr. San Andres deserve many thanks as well. Their critical review and technical advice opened new paths for investigation and helped to keep the project moving in a meaningful direction.

Special thanks goes to Bill Merka of the glass shop for helping develop an effective annealing procedure and for always being able to slip in a quick job even when he was busy. Thanks also to Rick Allen and Rodney Inmon, who can do anything for anyone and never get enough recognition. I also want to thank the many members of the aerospace engineering department staff, who are always there with advice and information. Thanks especially to Pam McConal, Natalie Willyard, Karen Knabe, and Andrea Loggins, to whom I will bring no more emergencies.

My friends and fellow researchers deserve the most thanks of all. Working and learning with all of them has been an unforgettable experience. It was a pleasure working and learning with with the likes of Pavlin Entchev, Ersin Karaca, Mughees Khan, Parikshith Kumar, and Tony Menn and the many others who shared experience, advice, and lunch. Thanks to Björn Kiefer, for putting his extraordinary intelligence to good use and for never insulting my golf game in front of me. Darren Hartl contributed more than he knows. Thanks for being the best officemate I could ask for. JJ Mayes, Eric Vandygriff, and Justin Strelec paved the way. Thanks for being great friends and sharing everything you know.

Finally, I would like to thank my family. I am grateful to my parents for providing the education I needed to get here and the money I needed to stay and to my brother for being my best childhood friend. Thank you to Aleisha for being everything a husband could ever want.

TABLE OF CONTENTS

LIST OF TABLES

LIST OF FIGURES

CHAPTER I

INTRODUCTION

In recent years an increased effort in engineering has been directed toward multifunctional materials and so-called "smart structures". A smart structure is defined by Srinivasan as an "assembly (or its components) which serve an engineering function" in which the structure possesses an "inherent ability to sense, diagnose, and actuate in order to perform their function" [1]. Perhaps the best examples of smart structures are found in biological systems. The leaves on a tree, for example, must both be open to collect sunlight and survive severe winds in a storm. To meet this end, the leaves have the ability to rapidly change shape under load while returning to the open position when the load is removed. Although the idea of multifunctionality originated in biological systems, it is not limited to them. In the case of an airplane wing, for example, the main purpose is to provide lift but it also serves as a container for the fuel.

A.   Shape Memory Alloys

One of the recent discoveries in multifunctional materials is "Shape Memory Alloys" (SMAs). This phrase describes a unique group of materials which execute a solid to solid phase transformation of their crystallographic structure, from the parent phase to monoclinic and back, in response to temperature or stress [2, 3, 4]. This property allows the material to be heavily deformed and regain its original shape upon heating. The acceptance of SMAs into industry applications had been slower than originally expected, and once earned them the reputation of "the solution looking for a problem" [5]. Duerig goes on to say, however, that this reputation is undeserved if one considers that the fundamental

---

The journal model is *IEEE Transactions on Automatic Control.*

properties are different from a "normal" material. Such a radical difference from normal materials has slowed the early adoption, but now SMAs are finding applications in many different industries.

One of the first large scale application of SMA was for a hydraulic pipe coupling on the Grumman F-14 [6], but the first area to see a large amount of applications was the biomedical industry. This is due to the fact that body temperature is the perfect range for operation of SMAs in the pseudoelastic range. Applications of this type include stents, filters, angioplasty guidewires, scissors, and graspers, to name a few [7, 8, 9, 10]. Some other applications include: underwater propulsion [11, 12], aviation [13], vibration suppression [14, 15, 16], and even valves and coupling devices for petroleum applications [17]. These applications capitalize on either the material's ability to undergo large strains with little or no permanent deformation or its ability to produce strains when exposed to temperature [18, 2, 3]. In addition, some applications rely on the hysteretic stress-strain response of SMAs under load.

The shape memory effect can be observed in several different alloys to differing degrees an example stress-strain graph of a material exhibiting the shape memory effect can be seen in Fig. 1. Although the parent phase is ordered in many of those alloys, this is not the main criteria for shape memory. In addition, the martensite-austenite transformation must involve a small volume change and the martensite must accommodate by twinning without slip. Even though there are several alloys which meet these requirements, there are only three systems which are currently of commercial importance: Cu-Zn-Al, Cu-Al-Ni, and Ni-Ti [19]. In addition to the shape memory effect, SMAs can exhibit a related temperature-independent behavior called pseudoelasticity, an example of this response is shown in Fig. 2.
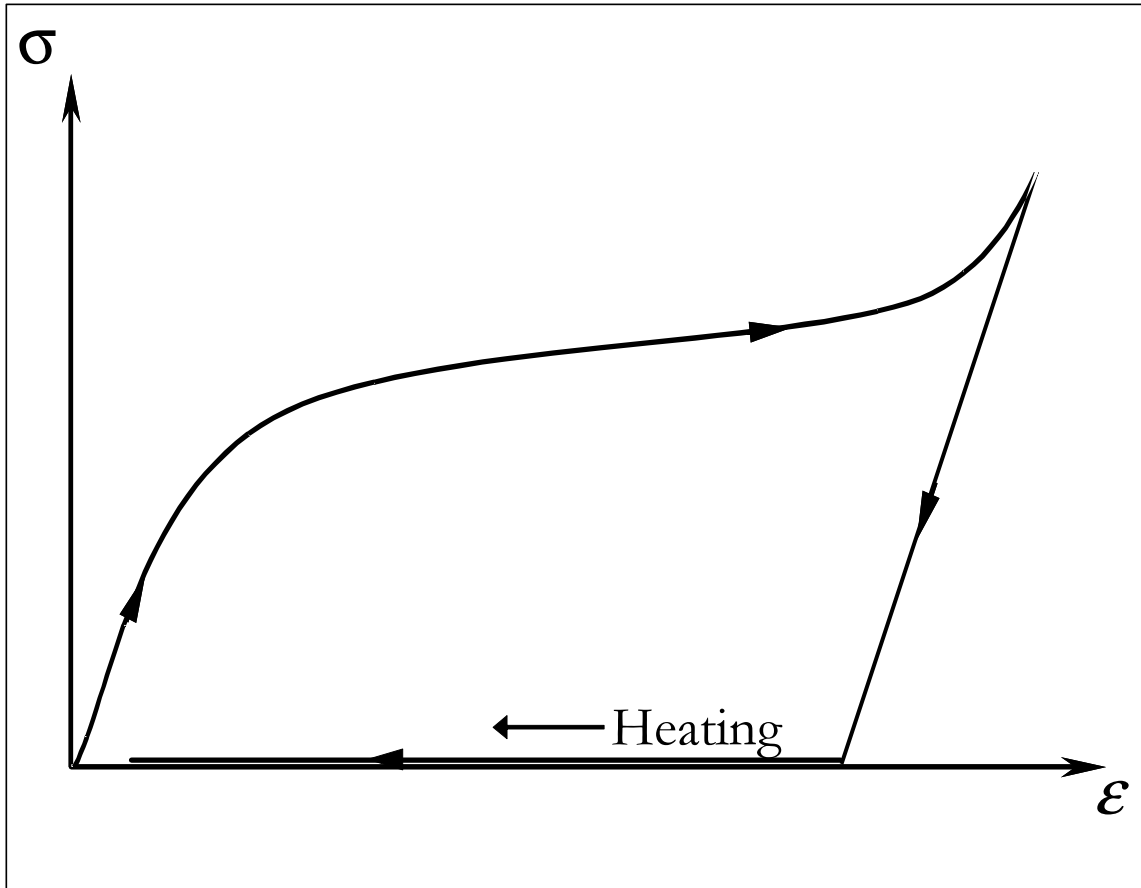
Fig. 1. Schematic of typical shape memory effect loading path.
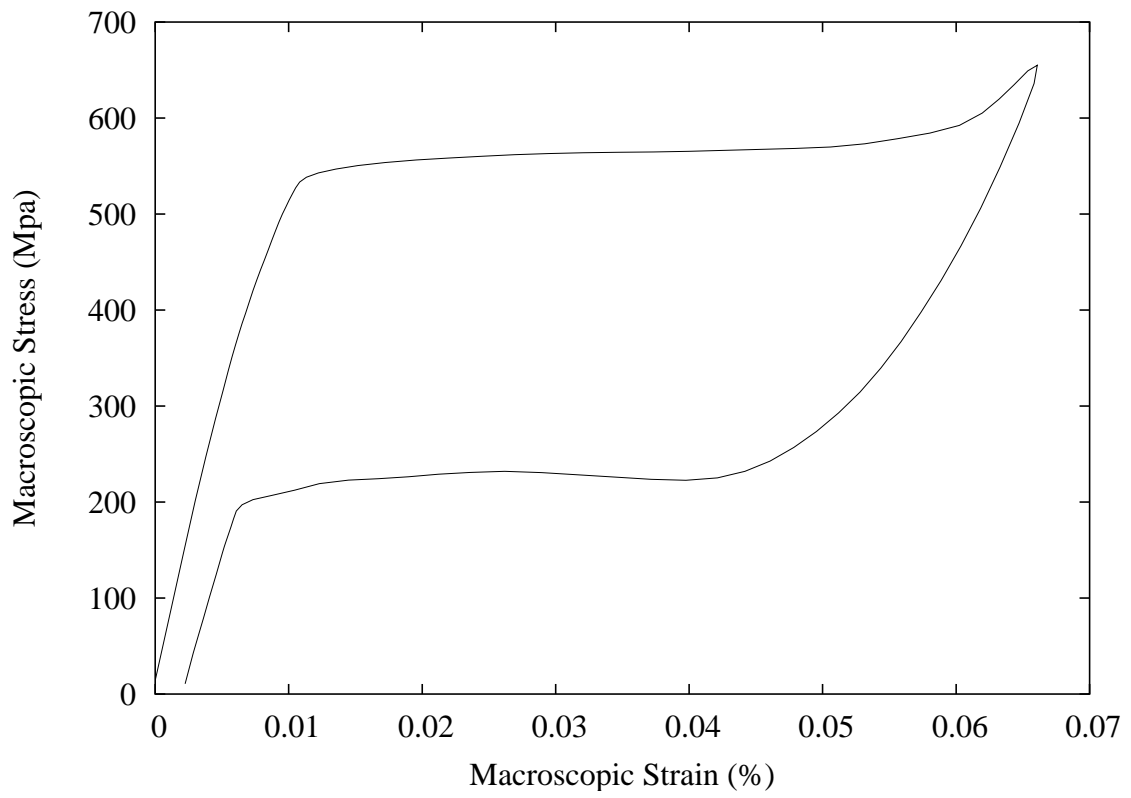
Fig. 2. Typical pseudoelasticity loading path.

1.   History

Although the components of shape memory were first observed in 1932, the effect its self was not observed until 1951, in a bar of gold-cadmium [20]. In 1962, Buehler et al. discovered the shape memory properties of the nickel-titanium system while working at the Naval Ordinance Laboratory (NOL). Buehler et al. named the nickel-titanium family of alloys Nitinol in reference to their workplace [21]. Nitinol was found to have excellent shape memory properties when composed of equal atomic quantities of nickel and titanium. Also, some properties could be finely controlled by the addition of extra nickel atoms. This and other desirable properties of Nitinol have rapidly accelerated its development for use in commercial applications. At this point the available commercial products use Nitinol almost exclusively. As such, this work is focused on nearly-equiatomic NiTi.

2.   NiTi Crystallography

The ability for a material to exhibit shape memory is a product of its ability to transform easily from the parent phase to martensite and back. Because this transformation does not modify the chemical composition, it is a non-diffusive process. This *displacive* transformation occurs at the speed of sound in the material and is completely reversible, but exhibits a hysteresis, a useful feature for energy absorption [22]. The high temperature state is called *Austenite* and in NiTi has a $B2$ structure. The low temperature phase, *Martensite*, has a complex monoclinic structure which is most commonly $B19'$. A schematic representation of the two phases can be seen in Fig. 3. The transformation from the parent phase introduces internal stresses as the shape of the martensitic region is not the same shape as the surrounding austenite. This stress is accommodated either by slip, as in a normal material, or by twinning, through lattice-invariant shear. Twinned martensite can be seen on the bottom left of Fig. 3. The phase change criteria is defined by four stress-dependant pa-
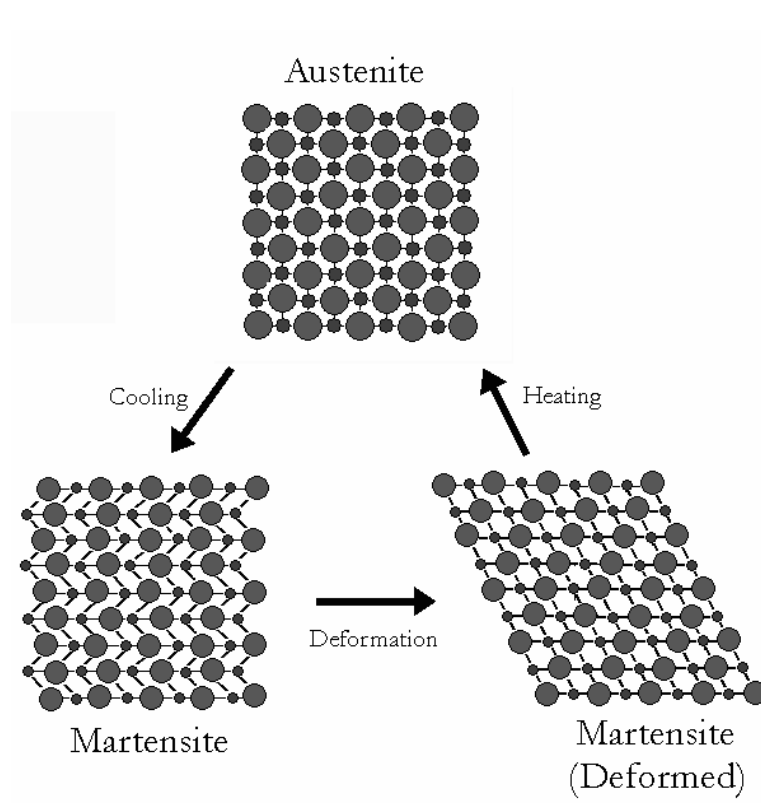
Fig. 3. Schematic representation of the crystal phases.

rameters: These parameters are collectively known as the "transformation temperatures". In the stress–temperature space they appear as the diagonal lines in Fig. 4. Changing the temperature of an SMA in the absence of external applied stress will result in crystal structure changes. As the material is cooled down to M_s, the cubic ($B2$) austenite arrangement begins to change to the monoclinic ($B19'$) arrangement. Although the local change is almost instant, the bulk of the material does not complete transformation until M_f is reached. Because there is no applied stress to effect an overall chape change, internal stresses are created which force newly forming martensite to accommodate the existing shape by forming twins. The net effect is a new crystal structure with no net shape change. It should be noted that there are 24 different variants of the $B19'$ structure. Self-accommodated martensite has equal probability of forming any of the different variants, the feature which allows twinning. Once heat is added to the twinned martensite, the atoms will again rearrange to their previous cubic orientation. Cubic cell symmetry ensures that only one path for reforming austenite exists, thereby ensuring that the original configuration will be regained [23].

3. Shape Memory Effect

To this point, the shape memory effect (SME) has been mentioned in several contexts without being fully explained. Now that the appropriate terminology has been explained, a full discussion of SME is warranted. By applying stress to twinned martensite, the alternating twin structures can be "flipped". By applying enough stress to flip most the twins in the same direction, an overall shape change will result. This is the first of two distinct steps in the shape memory effect and is called "detwinning" the martensite. When the stress is removed and the material heated, the crystal structure reforms into the cubic austenite. Since the force produced by this transformation is quite high, the material recovers the strain introduced through detwinning [24]. As mentioned above, there is one unique path by which the austenite can be formed due to the high symmetry of the $B2$ arrangement. Therefore,
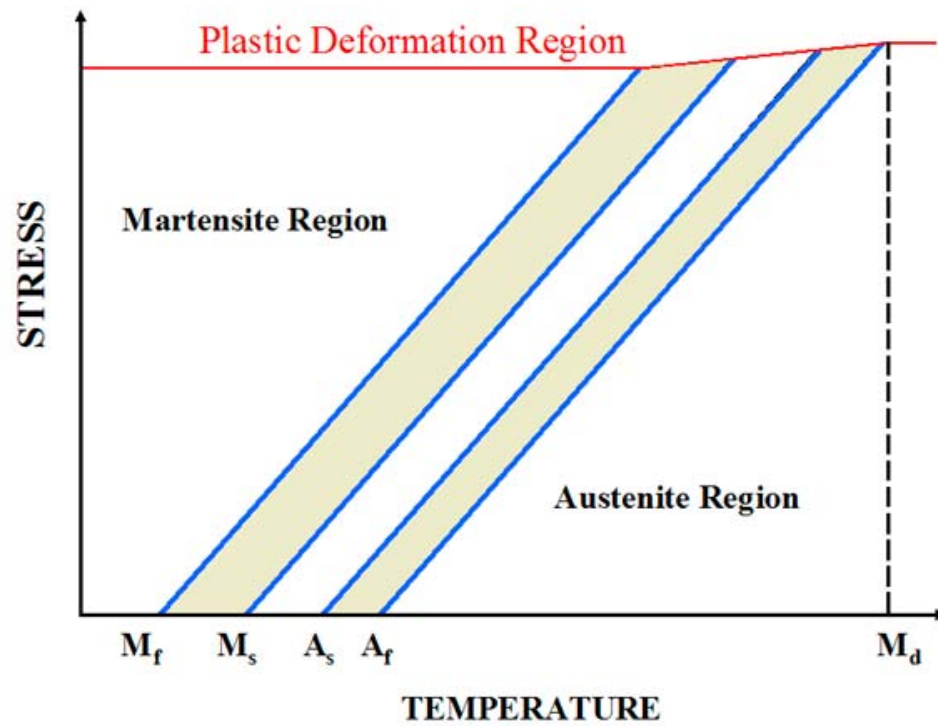
Fig. 4. Transformation temperature variation with applied stress showing M_d and regions of austenite and martensite.

regardless of the direction of stress applied during detwinning the same original shape will be recovered.

4.   Pseudoelasticity

The closely related transformation mechanism is called pseudoelasticity. Unlike SME where the process is both mechanical and thermal, pseudoelasticity is temperature independent. The appearance of this behavior over SME depends on the temperature of the material during the process, although that is not always the only requirement [25] If the material is maintained at a temperature just above A_f, it will start in austenite instead of in twinned martensite as before. Looking at Fig. 4, it can be seen that with applied stress and constant temperature, the material will eventually cross the M_s and M_f transformation boundaries. It is also readily apparent that the amount of stress required to cause this transformation will increase with an increase in temperature. An examination of Fig. 5 will reveal that the transformation is from austensite to detwinned martensite with no intermediate step. This type of transformation is called stress-induced martensite (SIM) [19]. The amount of recoverable strain varies with each sample, but this can be as high as 8% in tension and around 3.5% in compression [26, 27, 28, 24]. Pseudoelastic behavior is limited in temperature range, only attainable up to a fifth temperature, M_d. M_d is defined as the temperature above which martensite cannot be stress-induced [18]. The reason for this is that the stress level required for SIM is above the yield strength of the austenite, as can be seen in Fig. 4. When mechanical testing is performed at a temperature above M_d for that material, the performance will be similar to a standard elastic material where the properties are that of the austenitic phase.
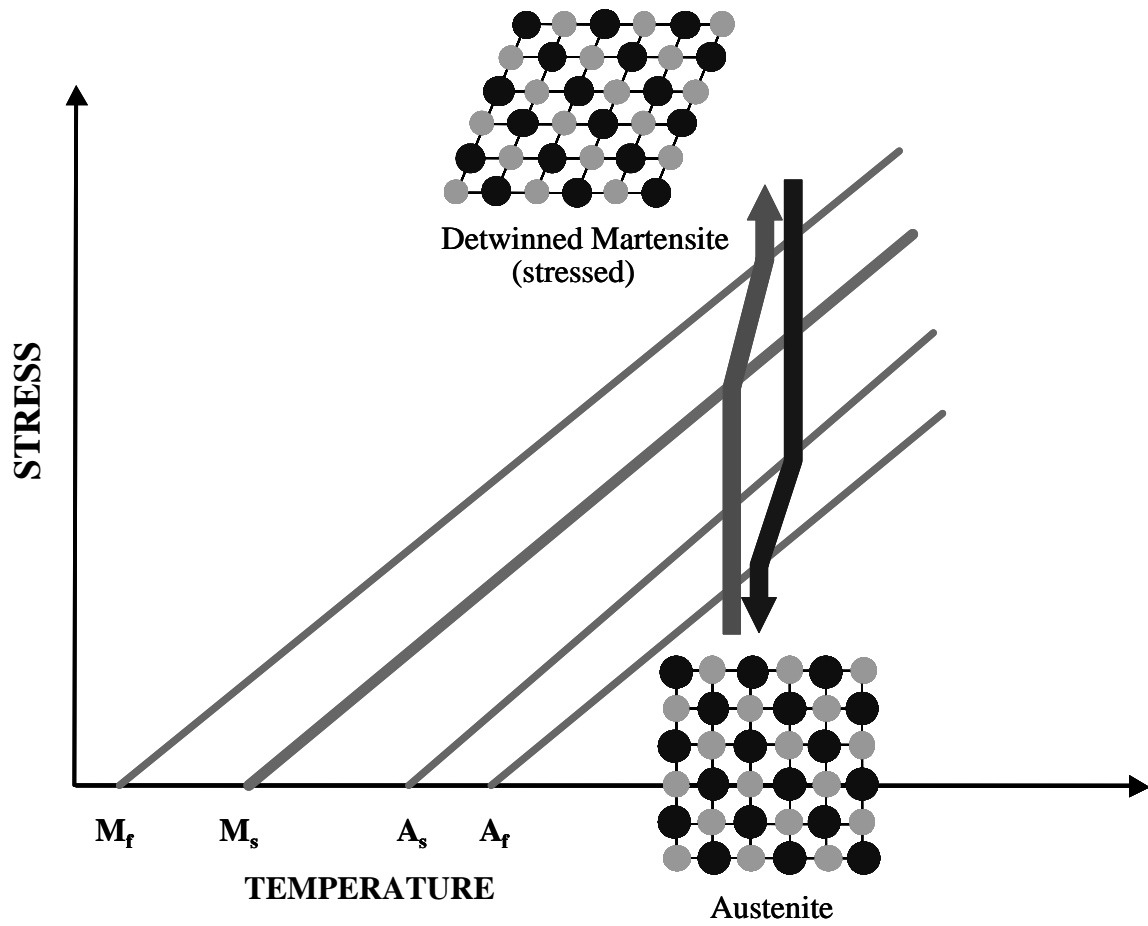
Fig. 5. Pseudoelasticity and stress-induced martensite.

5. Thermomechanical Treatments of NiTi

The A_f temperature of a Ti-50at.%Ni alloy is approximately 110°C. By changing that ratio to 51at.%, this temperature can be changed to below 0°C [24]. To achieve a desired set of properties, a manufacturer must control the composition to within between 0.1% and 0.01%. By comparison, the amount of Chromium in an 18/8 stainless steel must be controlled to within only 2% [29]. This presents a challenge for manufacturers but also gives them a reliable means for producing repeatable materials. An increase in nickel above the 50at.% level will lead to lower A_f temperatures and higher yield strength for the austensite. Generally NiTi is found with Ni concentrations up to 51.5at.% because above this the yield strength of the austenite is too high to allow the material to be drawn or cold worked [24]. Within this seemingly small range, however, a huge variation in properties can be found. In addition to their sensitivity to composition, NiTi alloys are extremely sensitive to thermomechanical treatments. Any single treatment can have a dramatic effect on strength, ductility, and the transformation temperatures.

Thermal treatments are one effective means towards achieving a specific set of transformation temperatures or for increasing the material's strength. This effectiveness is linked to the precipitations formed by excess nickel in nickel-rich compositions, called "precipitation hardening", which is a well-known phenomenon [30]. When such material is aged at temperatures as low as 350°C, nickel atoms will begin to pull from the matrix and form Ni_4Ti_3 precipitates [31]. This can dramatically alter the transformation temperatures. For example, the author has shown it is possible to lower the A_f temperature as much as 100°C through a simple heat treatment. In addition to modifying the transformation temperatures, the ability of the material to transform and back-transform can be enhanced through aging, especially in heavily Ti-rich compositions. Specifically, the formation of some small $NiTi_2$ precipitates can introduce internal stresses to limit the range

of martensitic plate growth while at the same time helping them to back-transform [32].

Another way to influence the behavior or properties of an SMA is through mechanical deformation. For example, some researchers have found that deforming NiTi in martensite resulted in a more stable martensitic state. This led to a larger hysteresis and a higher heat of reverse transformation, an important result where the temperature required to actuate is critical [33, 34, 35]. Some researchers are combining the methods used in thermal and mechanical processing to increase the performance of SMAs.

A process called "marforming" is a two step process used to enhance the properties of SMAs, especially where precipitation hardening is not appropriate due to a near equiatomic composition. First the material is heavily deformed while fully in the martensite stage. This is done either with ice water or liquid nitrogen. After the deformation, the material is tempered for a predetermined time at a temperature between 350 and 600°C. In the case of NiTi alloys with low nickel content, the deformation introduces dislocations which enhance pseudoelasticity performance by introducing internal stresses to promote back transformation [36, 37]. This type of processing can also be done to enhance two-way SME [38]. In addition, the deformation can be done at different material conditions which will produce differing resultant microstructures [39].

6.   Porous Shape Memory Alloys

Continuing the long-standing effort to decrease weight while increasing performance, researchers are beginning to study the properties of porous shape memory alloys [40, 41, 42, 43]. Porous SMAs exhibit all the same properties as their dense counterparts, but with the added benefit of low density and the ability to undergo larger deformation before failure. Some uses of NiTi in the body were mentioned earlier. With proven biocompatibility, NiTi is being investigated as an implant material for bone replacement [44]. In porous form, NiTi shows greater promise for bone replacement as the pores allow bone in-growth and

therefore stronger adhesion [45, 46].

As mentioned above, SMAs show promise as materials for energy absorption and vibration isolation [16]. This ability has been applied in several applications including in bridges as passive absorbers [47, 48], as a component of base isolation systems [49], as a means of tuning the response of composite beams [50, 51], and in isolation systems for spacecraft payloads [52]. An isolation system designed around porous SMA would take advantage of the inherent damping of shape memory alloys while at the same time providing structural rigidity and decreased weight. Porous SMA may be manufactured with graded porosity for specific biological applications, impedance matching, or thermal protection.

Porous SMAs are manufactured several different ways and depending on the application, the structure and properties can be adjusted to meet a specific need. One such case is the need for a pore structure for use in bone implants. Porous SMA can be manufactured with both types of pores, open and closed, but it had been found that bone growth is promoted by an open structure, which has lower density and better permeability [46, 45]. Several methods exist for creating porous metals [53] but they are not all appropriate for the production of porous NiTi. Some examples are Metal Injection Moulding (MIM) [54] and Spark Plasma Sintering (SPS) [55], both of which produce acceptable dense NiTi, but are not easily modified to produce porous material. A few methods have emerged as both efficient and reliable: Self-propagating High-temperature Synthesis (SHS), conventional sintering, and sintering at elevated pressure (HIPing).

a. Self-Propagating High-Temperature Synthesis

Self-propagating High-temperature Synthesis (SHS), or combustion synthesis, has also been used to produce porous NiTi from elemental powders [56, 43, 57]. A compact is packed into a container and a self-sustaining reaction is initiated by either an explosion

or by heating the compact to a high enough temperature [58]. This process relies on the exothermic reaction of Ni and Ti diffusion to propagate. During the reaction, the material is heated over several hundred degrees and subjected to a shock pressure of approximately 17 GPa [59, 60]. Combustion Synthesis is extremely quick, which means that all control of porosity and composition must be done prior to starting the reaction. Although the porosity in materials formed through SHS can be as high as 65%, the samples are often not fully reacted or contain precipitates due to the short forming time and high heating rates [61, 62].

b.   Conventional Sintering

The method of conventional sintering is a near-atmospheric pressure process in which elemental powders of Ni and Ti are pre-packed into a canister and then heated to near-melting temperatures. The temperature is held for a long time (e.g. 48 hours) during which the powders diffuse to form a solid compact [41, 63]. The porosity of the formed compact is controlled by two factors: the initial packing and the particle size and shape. Conventional sintering provides no other vehicle for controlling the porosity during the process and as a result the porosity is usually limited to about 40%. In addition, the material often contains many intermetallic phases which affect the overall performance [64].

c.   Hot Isostatic Pressing

Tackling some issues with conventional sintering, Kearns et al. in 1988 showed that it was possible to increase the porosity of a HIPed compact by heat-treating after compaction. If the sample was first subjected to high pressure Argon before heating, the argon would be compressed during the HIP run and would provide force to expand the small pores during later heat-treatment. This method produced porosities up to 40% in Ti-6Al-4V, much higher than could have been produced via conventional sintering. In addition, the compact could be cold worked prior to pore expansion in order to bias the expansion direction or to modify

shape and microstructure [65].

His work was later expanded by Schwartz [66] and then Davis et al. expanded on this work be examining the methods by which the expansion occurred and the effect of different temperatures on the process. In addition, the work expanded knowledge of the effects of tension and thermal cycling during expansion [67]. In the same time, McNeese et al. experimented with creating fully dense NiTi parts in a HIP. This work increased the knowledge of how NiTi behavior was affected by the HIPing process and sought to create material with properties identical to that of vacuum induction melted and vacuum arc remelted material with moderate success [42]. Vandygriff et al. combined the work done by McNeese et al. with that of Kearns et al. to create porous NiTi by HIPing. material produced by Vandygriff showed some degree of SMA performance, but was limited in ability due to the large amount of precipitates in the final material. This material, as most made from elemental powders, contained other intermetallic phases, namely Ni_3Ti, $NiTi_2$, Ni_4Ti_3 and Ni_3Ti_4. Even with this, the advantages of HIPing over conventional sintering and SHS were clear. Vandygriff found that this process allowed for the variation of pore size and porosity independent of one another. The use of the HIP proved an advantage over SHS in allowing more complete reactions to occur as well as more control during the process while taking much less total time. Because the powders require a long period of mixing prior to HIPing, oxides were allowed to form on with the Ti. In addition, even very long mixing times did not ensure complete mixture of the Ni and Ti and this contributed to the formation of the mentioned secondary phases during HIPing. The creation of secondary phases is a recurring problem in all three described methods. This is primarily due to the narrow region in which NiTi is the stable phase. This is clearly illustrated by examination of the binary phase diagram (Fig. 6) which shows that the only way to ensure having only NiTi is to quench from a high temperature, something that is not possible if the material is being fabricated in a HIP.
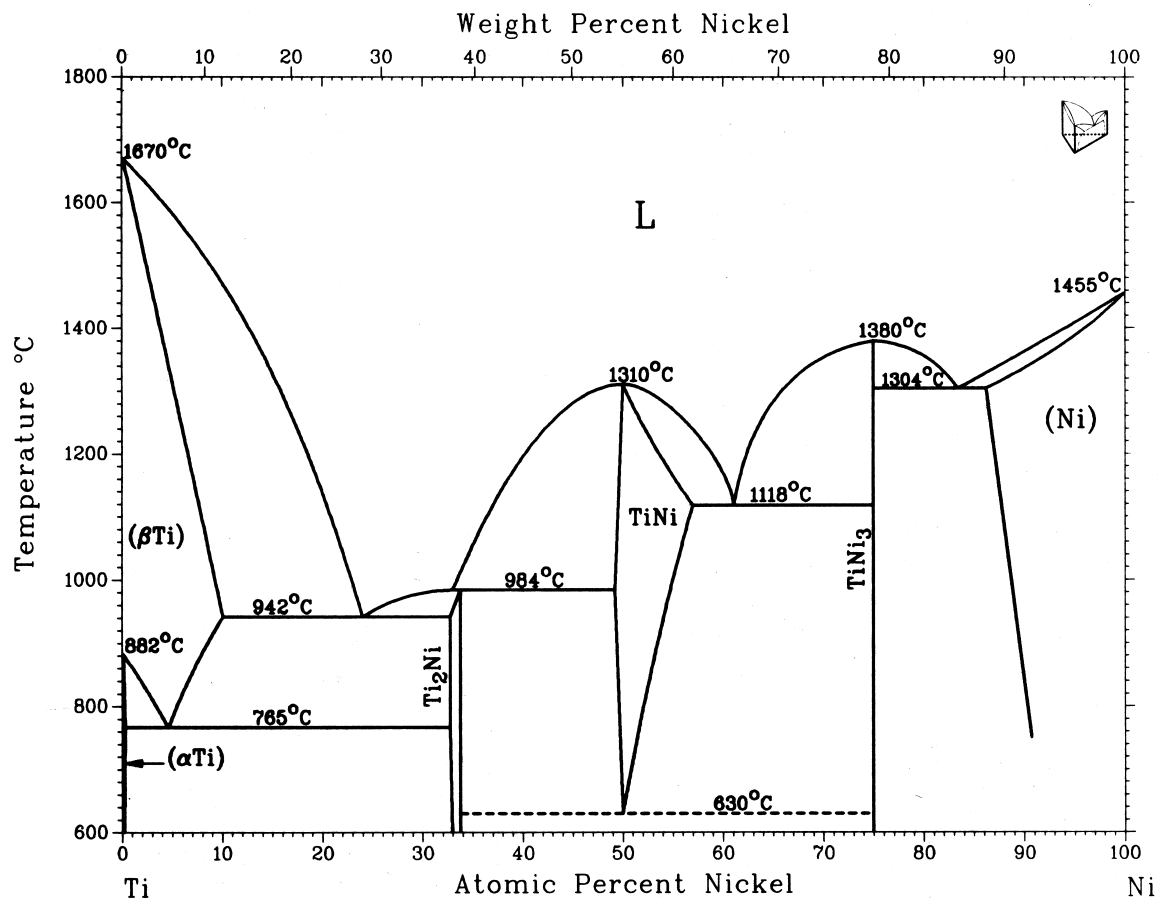
Fig. 6. Phase diagram of NiTi.

CHAPTER II

FABRICATION OF POROUS SMA

In addition to the work on elemental powders, some attention is being paid to the consolidation of pre-alloyed powders [68]. This effort is influenced by the ease of preparation and handling of pre-alloyed powders compared to that of elemental powders. Although pre-alloyed powder is more expensive, the advantages of its use outweigh the cost. When preparing a compact of elemental powders for HIPing, for example, the powders must be precisely measured and then mixed for many hours to ensure complete dispersion. Even long mixing times, however, do not guarantee complete combination of the powders and may harm the powders as they are exposed to oxygen which will readily combine with the Ti powder, making the composition nickel-rich. By comparison, preparing a compact of pre-alloyed powders is simple. This procedure only requires pouring the appropriate amount of powder into the HIP canister. Because of this simple method, and the cleanliness of the powder production process, the powder is virtually oxidation free. This was verified via microprobe analysis by comparison with a sample which was visibly oxidized. Also, handling elemental nickel is potentially harmful as it is a known carcinogen [69]. This chapter will present background information on materials used in this study as well as the procedures used to process the powders and prepare the porous SMA for study.

A. Pre-alloyed Powders

Powders used in this work are produced by the Plasma Rotating Electrode Process (PREP) from Starmet, Inc. PREP is one of the rotating electrode processes, chosen for NiTi powders in this study due to the lack of a traditional electrode which can contaminate the material with tungsten. All the rotating electrode processes (REPs) are widely recognized as acceptable processes for producing titanium powders due to their minimization of prob-

lems due to the activity of titanium in the molten state [68]. The PREP process consists of spinning a section of bar stock, in this case NiTi, past a current source. The stock used in this study were fabricated by Flowserve Corp. in the form of three approximately 11lb bars of nearly binary NiTi. After investigation, however, it was discovered that the bars were not behaving as Ti-50.2at.%Ni. By examining the material in a Cameca SX50 Electron Microprobe, the composition is clearly understood. A visually striking method is through images created by backscattered electrons, as is shown in Fig. 7, where the intensity of electrons scattered by a material depends on the material's composition. In this case, a light-colored matrix can be seen containing a darker second phase. Through other functions of the microprobe, more information about the composition can be found. Two techniques are used for quantitative investigation, Wave-Dispersive X-ray Spectrometer (WDS) and Energy-Dispersive X-ray Spectrometer (EDS). Because the two analyses provide similar information and WDS gives better resolution, the EDS results will not be included here. Instead the WDS analysis is presented in Table I, which shows one analysis of the light region and one analysis each of two separate dark areas. These results clearly show that the matrix (lighter area) is NiTi and the second phase (darker area) is $NiTi_2$. Using image analysis, it can be determined that the lower magnification image (Fig. 7) is composed of 8% $NiTi_2$. The clear conclusion seems to be that the electrode material is rich in titanium. When an arc is started from the source to the spinning bar stock, it becomes an electrode and molten metal leaves the bar in droplets which then solidify in the argon atmosphere. As the droplets fall, they are sorted through meshes. While it is not possible to form a single size particle, a different median size may be obtained simply by adjusting the rotational speed of the bar. Although the supplied powders from Starmet were of three sizes, the powders chosen for this study were 105–$180\mu m$. The other two sizes available were $< 105\mu m$ and $> 180\mu m$ and it was thought that the intermediate range would give a more consistent particle size as well as a smaller overall variation. An SEM photograph of
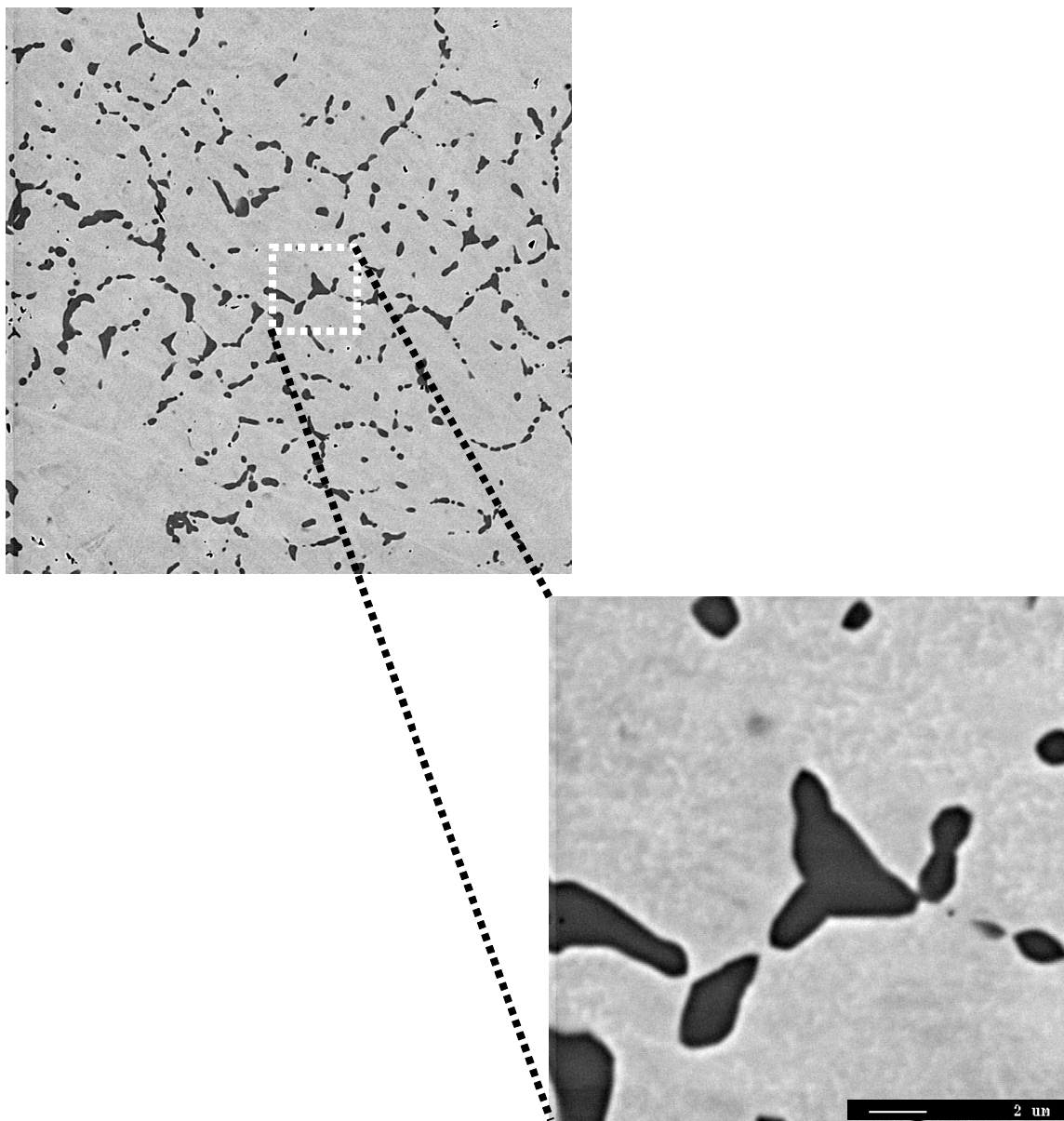
Fig. 7. BSE images of Flowserve electrodes. Inset: 700X magnification of highlighted area.

Table I. Elemental analysis of two phases within electrodes using WDS analysis (error: $\pm 1\%$).

	Ni (at%)	Ti (at%)
NiTi	49.07	50.93
First analysis of NiTi$_2$	34.70	65.30
Second Analysis of NiTi$_2$	33.19	66.81

the powders as received is shown in Fig. 8 which shows that they are predominately, but not completely, spherical. This can be attributed to the high cooling rate of the metal during the forming process, a rate which is not widely documented, but has been reported as high as $10^{-4} K sec^{-1}$. Another effect of the high cooling rate is to solidify the particles before they have reached equilibrium [70]. In the case of NiTi powders, this leads to the dendritic morphology which can be seen in Fig. 9. This structure has been observed as well by Apgar and Eylon in other titanium alloys formed via the PREP method [71]. In Fig. 9, the darker regions were again confirmed to be Ti-rich, occurring because of the composition of the starting material. The powders were shipped to Texas A&M in three containers, one for each size. Storage of the containers is easier than that of the elemental powders due to the low activity of the material at room temperature, but care is still exercised as oxidation is possible. After each time a container is opened for use, it is placed inside a small vacuum chamber, pumped completely, then backfilled with argon and resealed. Resealing this way
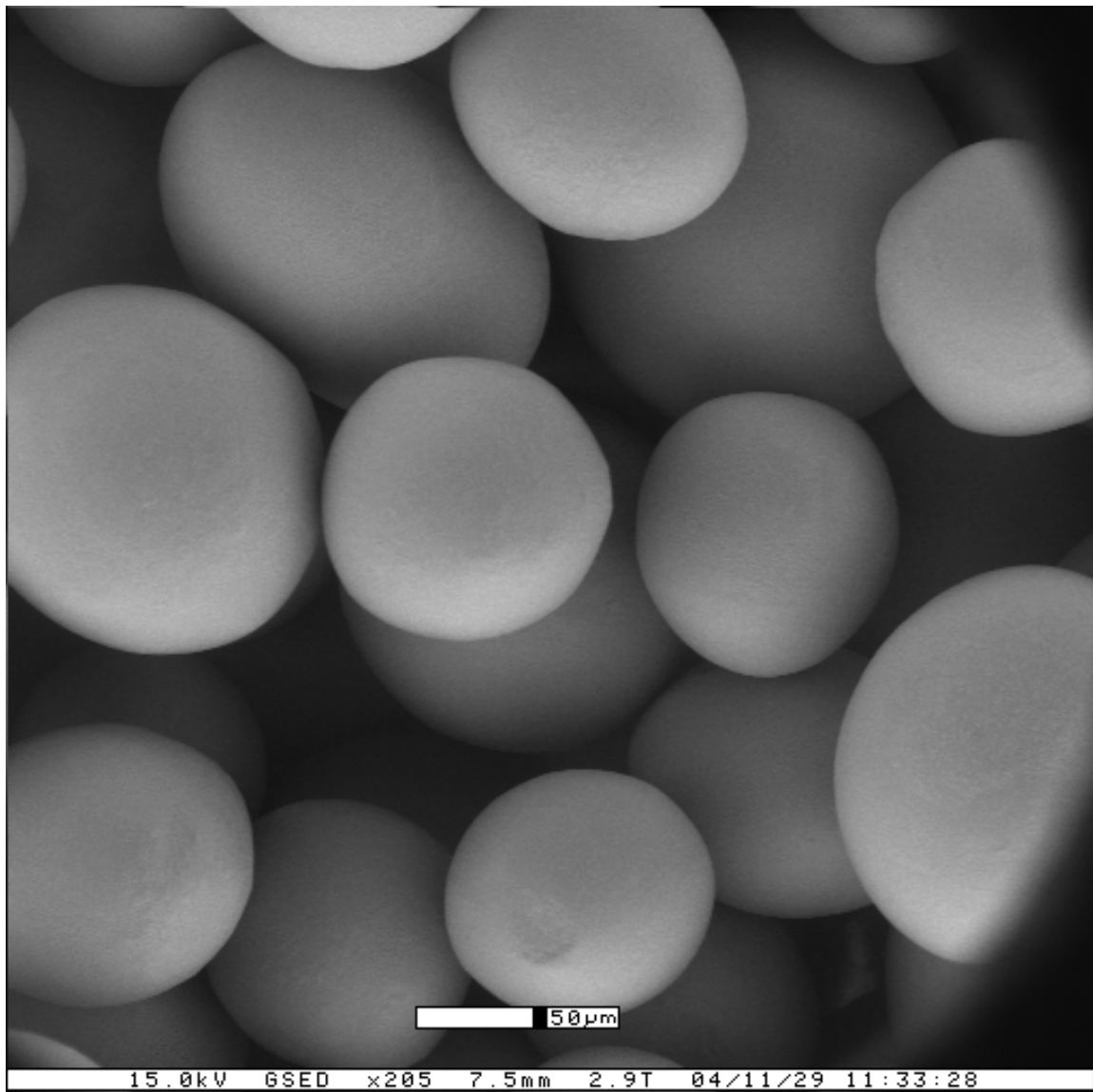
Fig. 8. Scanning electron microscope photograph of NiTi powder.

20 um
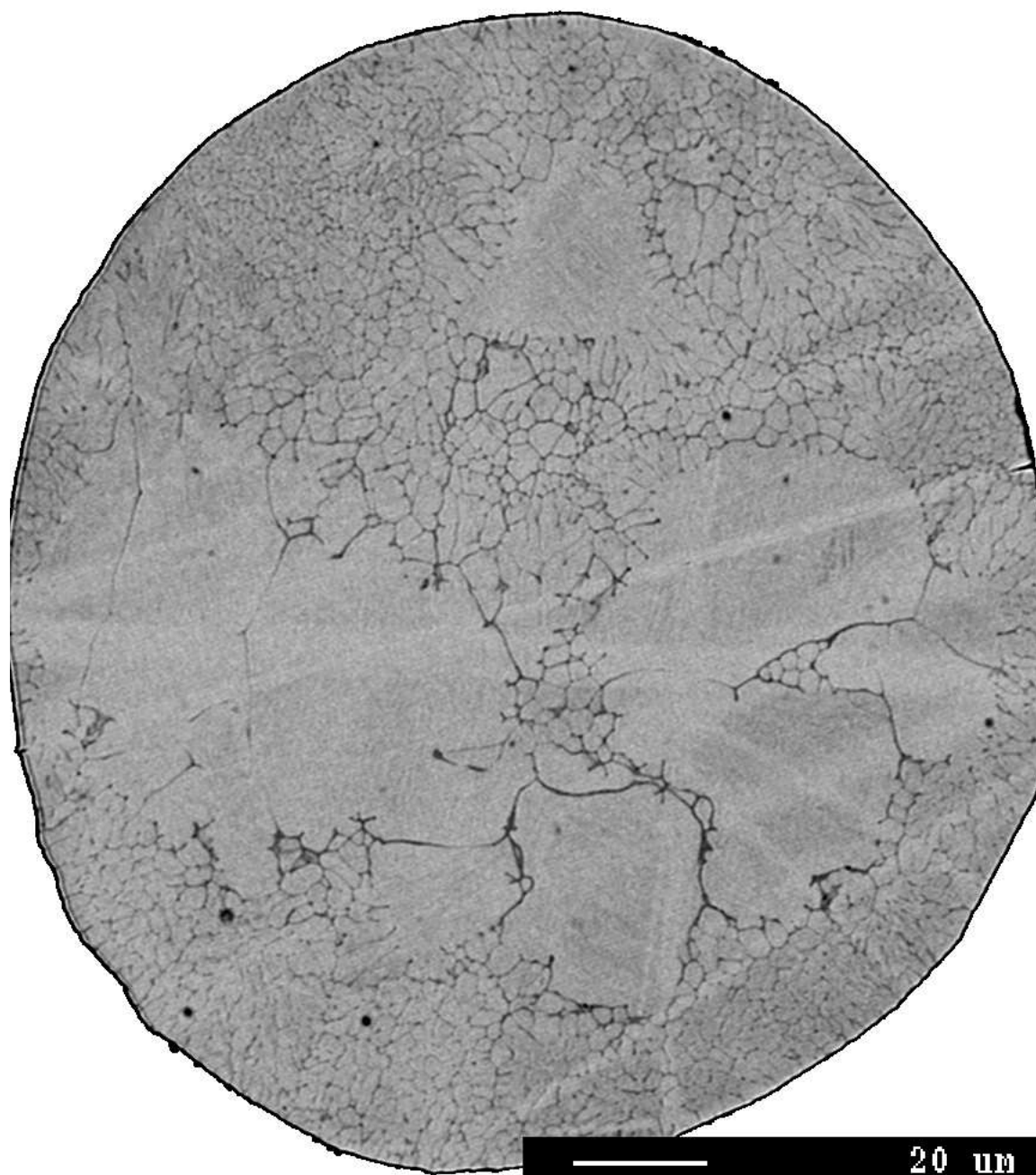
Fig. 9. BSE image showing dendritic morphology of powders.

has proved effective in minimizing the oxidation layer on the surface of the spheres. In fact, a comparison of the powders and a consolidated and heat treated sample indicates a lack of oxidation or at least a minimal thickness. Fig. 10 illustrates this comparison. The lower picture in this figure is of a consolidated sample which was then heat treated. The consolidated sample grew a visible oxidation layer during heat treating which can also be seen in backscatter by adjusting contrast to wash out features within the interior of the material. In the upper picture, the contrast had been adjusted similarly while examining a cross section of powders before any processing. As no similar oxidation region is visible, the powders lack a similar oxidation layer. Once the container is resealed, it is first shaken vigorously then placed back onto a shelf in a different orientation than when it was retrieved. This approach is taken to minimize the effects of long-term storage on the powders. In fact, these handling procedures are much simpler than what is required for elemental powders, leaving only one real negative argument dealing with the higher cost of elemental powders. This cost cannot be avoided and is nearly twice that of elemental powders. With the number of ease-of-use issues and the quality of the finished product, however, this cost is justified.

Fig. 10. Comparison of oxidation levels between powders (upper) and consolidated sample (lower).

B. Hot Isostatic Pressing

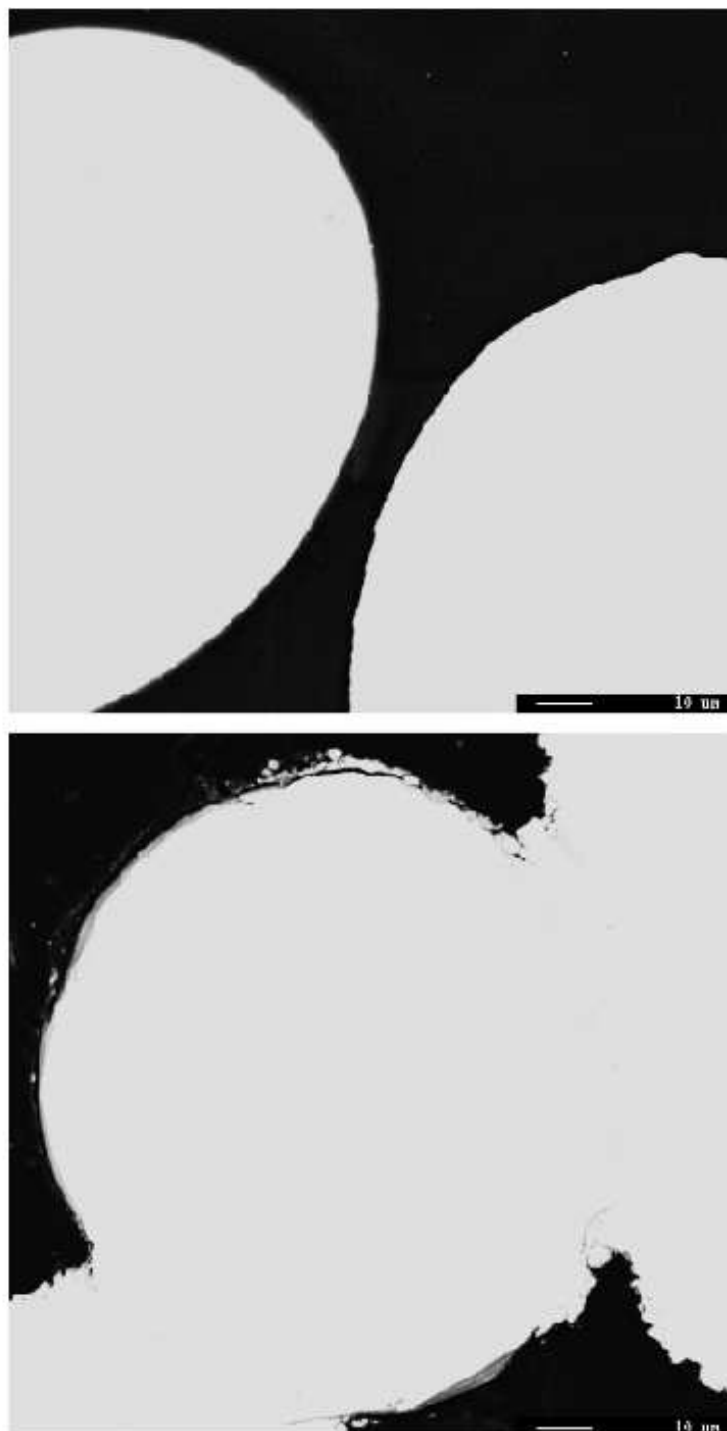To prepare a compact for HIPing, a canister is machined following the design of Vandy-griff et al. [72]. The canister is approximately $3''$ long with an outer diameter of $5/8''$ and an inner diameter of $1/2''$. A diagram of the canister can be seen in Fig. 11a. Each end of the can is sealed with a cap machined from material identical to that of the canister, which in this case is 316 Stainless Steel. The lower cap is welded completely to make an airtight seal. The top, however, is only spot welded in two spots, on opposite sides of the can. This loose attachment is used to allow the passage of Argon in and out of the canister during HIPing. The weld locations and types can be seen in Fig. 11b. Unlike traditional HIPing methods, this method does not produce a crushed canister which must be machined away to allow the material to expand in the post-HIP heat treatment. Once the canister is machined and the bottom cap is welded into place, it is first sand blasted to remove the contamination caused by welding and then cleaned thoroughly in an acetone bath by an ultrasonic cleaner to remove machining oils and other dirt. After this, the canister is filled almost completely with pre-alloyed powders. During the filling, the canister is constantly tapped to pack the powders more tightly than is achieved through pouring. The top cap is then tack welded in place as described above and the canister is loaded into the HIP. Because of the open can design, argon pressure is applied directly onto the powders after having travelled through the slightly open lid. The effect of this is that the pressure can be released and the porosity increased while the part is still in the HIP and still at high temperature instead of during a post HIPing heat treatment. It is obvious from some micrographs that this expansion is taking place. Fig. 12 shows a bridge has formed between neighboring powders. Because of the application of pressure early in the cycle, this bridge must have been formed when the argon expanded within the pores and pushed the powders apart slightly.

Texas A&M University maintains an Asea Brown Boveri QIH-3 Mini-hipper capable
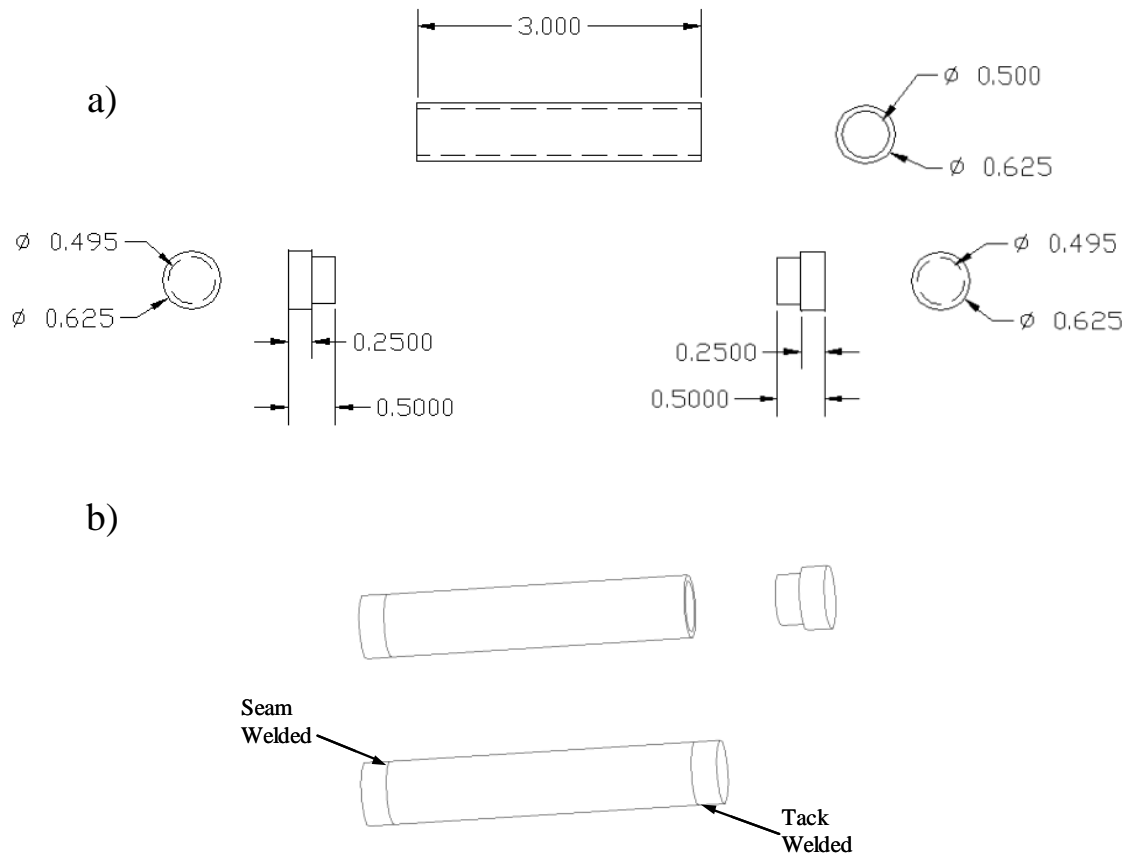
Fig. 11. HIP canister design. (a) Diagram and dimensions of HIP canister and (b) assembled canister showing weld locations.
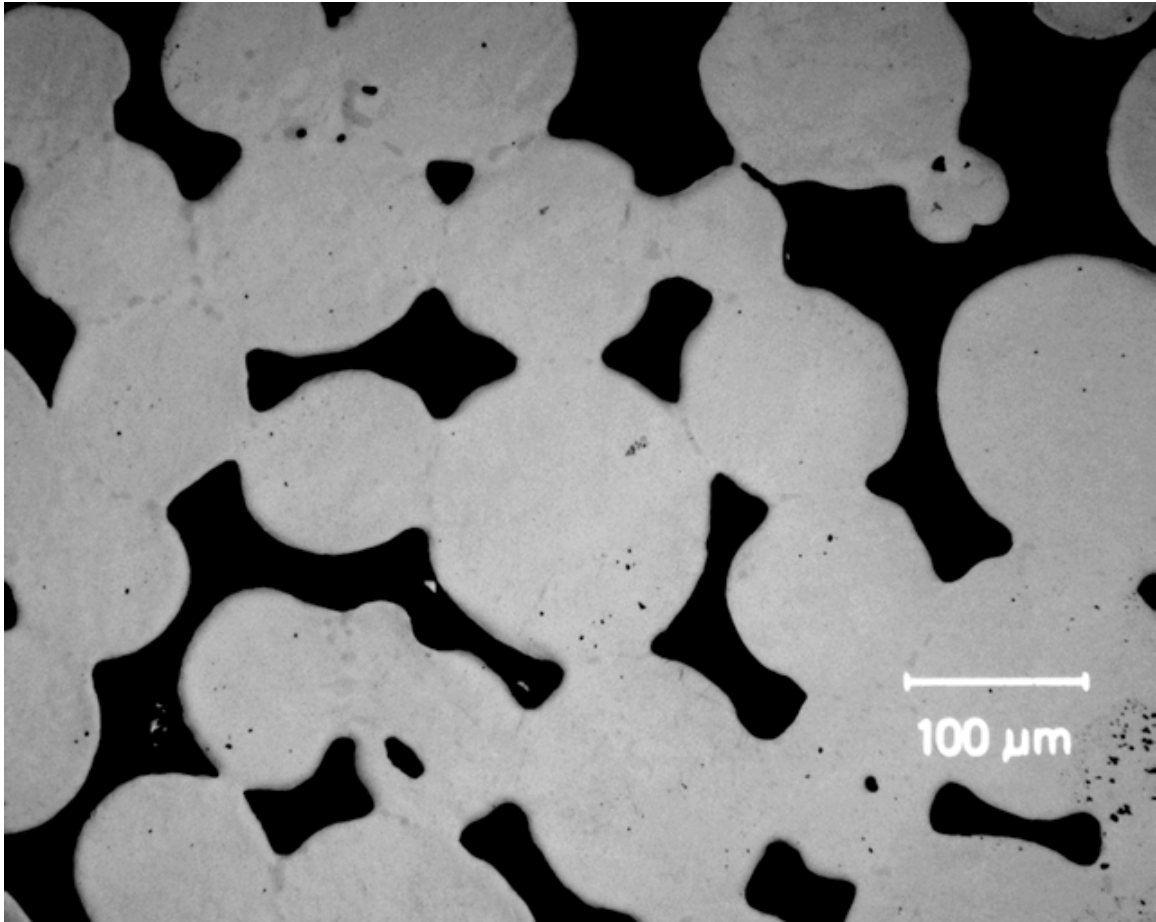
Fig. 12. Micrograph showing necked regions of pore expansion.

of up to 2000°C at 217Mpa. The QIH-3 is controlled by a programmable μMAC 5000 linked to an IBM 286/XT computer. Once a recipe is designed and stored, the computer downloads it to the onboard controller and acts as a monitor but also has the ability to modify the running program while the microMAC controls the times, temperatures, rates, and pressures required to execute the recipe. Although several furnace materials are available, a graphite furnace is currently in use and is monitored by three thermocouples which are installed at varying heights through the furnace. The available space inside the furnace for materials is about 3.3" in diameter and 5.7" in height. A picture of the HIP and the furnace enclosure can be seen in Fig. 13. Recipes used were adapted from the work of Mc-Neese [42] and Vandygriff [72]. Because their work centered around elemental powders, the temperature settings and times had to be adjusted for use with pre-alloyed powders. The final recipes were found through trial and error with the quality of the specimen as the main determining factor of effectiveness. The hold temperature used in this work is well above those used by Vandygriff and McNeese. This is expected as the combination of Ni and Ti is exothermic and therefore heats the compact above the temperature of the furnace. When HIPing pre-alloyed powders, no additional heat is generated by the diffusion, so the furnace must be maintained at a higher temperature. After several trial runs, the hold point was selected at 1100°C. At 1050°C very little consolidation took place, resulting in a "caked" appearance with small sections of loosely combined material. Raising the temperature slightly to 1150°C leads to regions of melted material where the powders had liquified and allowed the argon to escape completely. These melted sections were flattened, leaving a slightly asymmetric sample. Data from these trial runs is shown in Appendix A. A diagram of a later HIP recipe is shown in Fig. 14. The actual data from a cycle using a similar recipe is shown in Fig. 15, and is the final cycle used which consistently produced material with 40% porosity. Note that the data is slightly different from the diagram in the pressure during the hold step. This is intentional and did not affect the final product. The poros-

Fig. 13. QIH-3 Mini-hipper and detail of furnace.

ity obtained compares favorably to the lowest porosity achievable—without deforming the spheres—of 26% which occurs in a hexagonal close packed arrangement.

The first step in the HIP recipe, labelled number 1 on the diagram version, is to heat the chamber under low pressure. This step ensures that the seals required to contain high pressures are properly expanded. At this point, the powders are not greatly affected and remain largely separate with the same packing as when they were first loaded into the canister. During step 2, the pressure is raised dramatically while the temperature is raised only slightly. Raising the pressure in this step while keeping the temperature low fills the spaces between powders with high pressure argon before the powders have started to combine. Next is the consolidation step, number 3. The temperature is raised to the hold temperature, 1100°C, and held for 2.5 hours. The rate in this step is taken from the work of McNeese and is 35°C/min. High temperature and a maintained high pressure combine to force neighboring powders to combine seamlessly through diffusion. After the hold time has elapsed, the pressure is dropped to near atmospheric while the temperature is dropped only slightly, step 4. The step, as mentioned above, uses the stored energy in the argon to expand the pores. Argon was compressed into the pores in step 2 and now that the powders have combined the only way for the argon to escape is by pushing the powders apart. Verification of this hypothesis is made by examining micrographs of the finished product, shown in Figs. 12 and 16. The last step, number 5, is simply a return to atmospheric pressure and temperature. These three micrographs clearly show the good connectivity between powders and also the stretching caused by argon expansion in step 4. It should be noted that not all the powders begin spherical, and this is the cause of the oblong powders in these figures. This method of forming porous SMA creates a closed pores, meaning that the pores are not interconnected but exist as pockets within a matrix. This structure is not suitable for biomechanical applications, which require an open structure for bone in-growth, but is acceptable for use in structural applications.
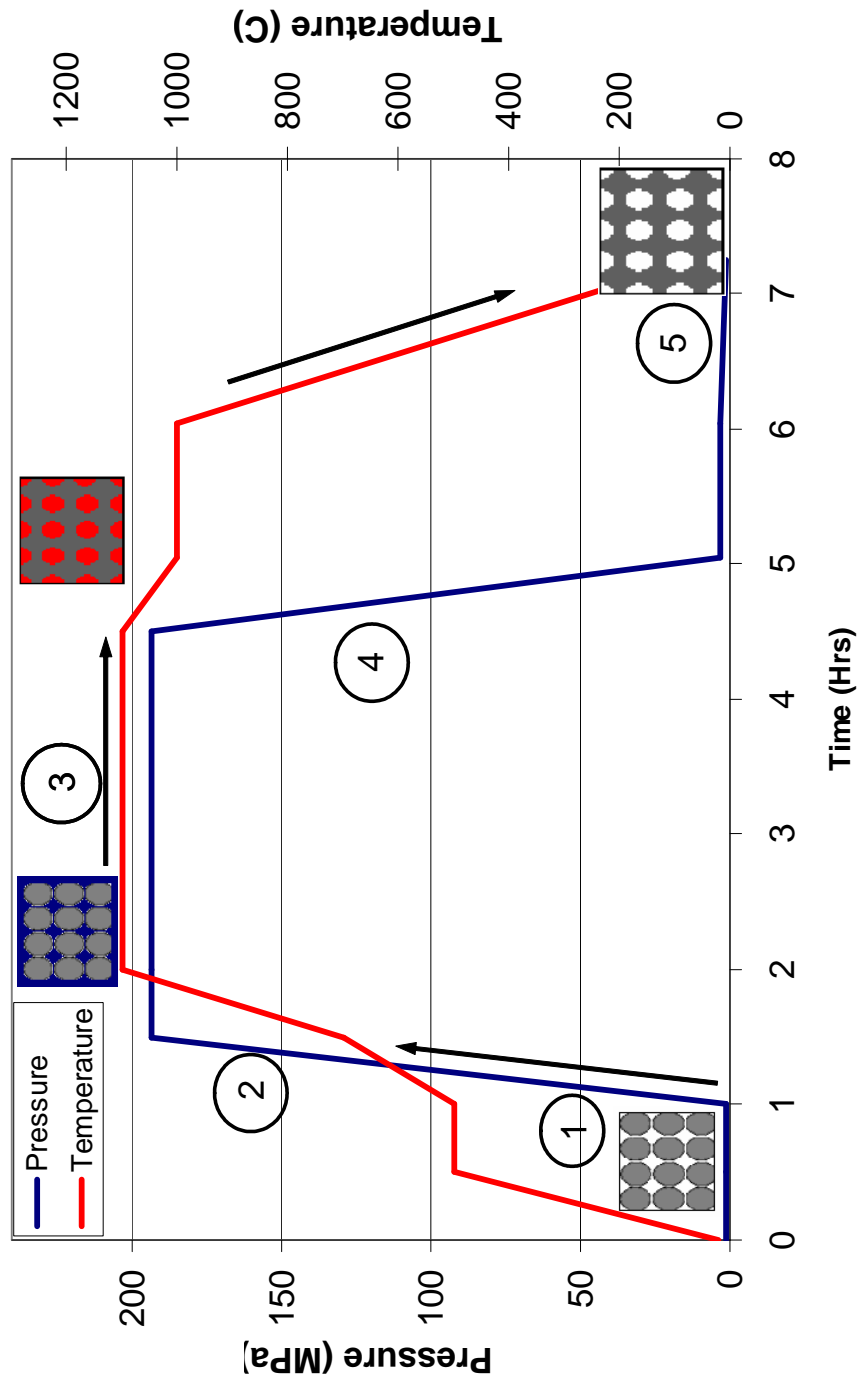
Fig. 14. Diagram of a typical HIP cycle showing schematics of the current material condition.
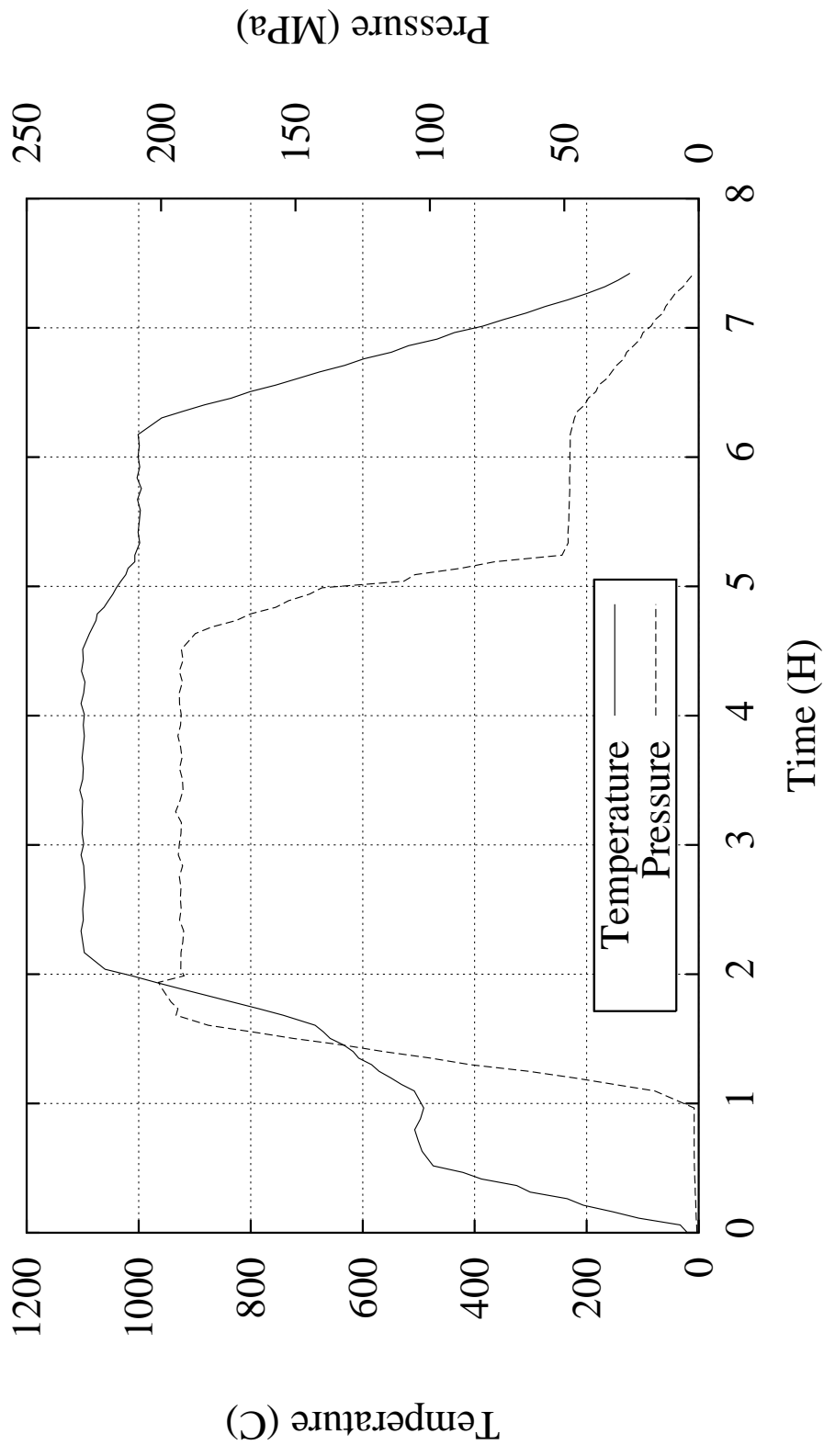
Fig. 15. Final HIP run with soak temperature of 1100°C and additional low pressure/high temperature step.
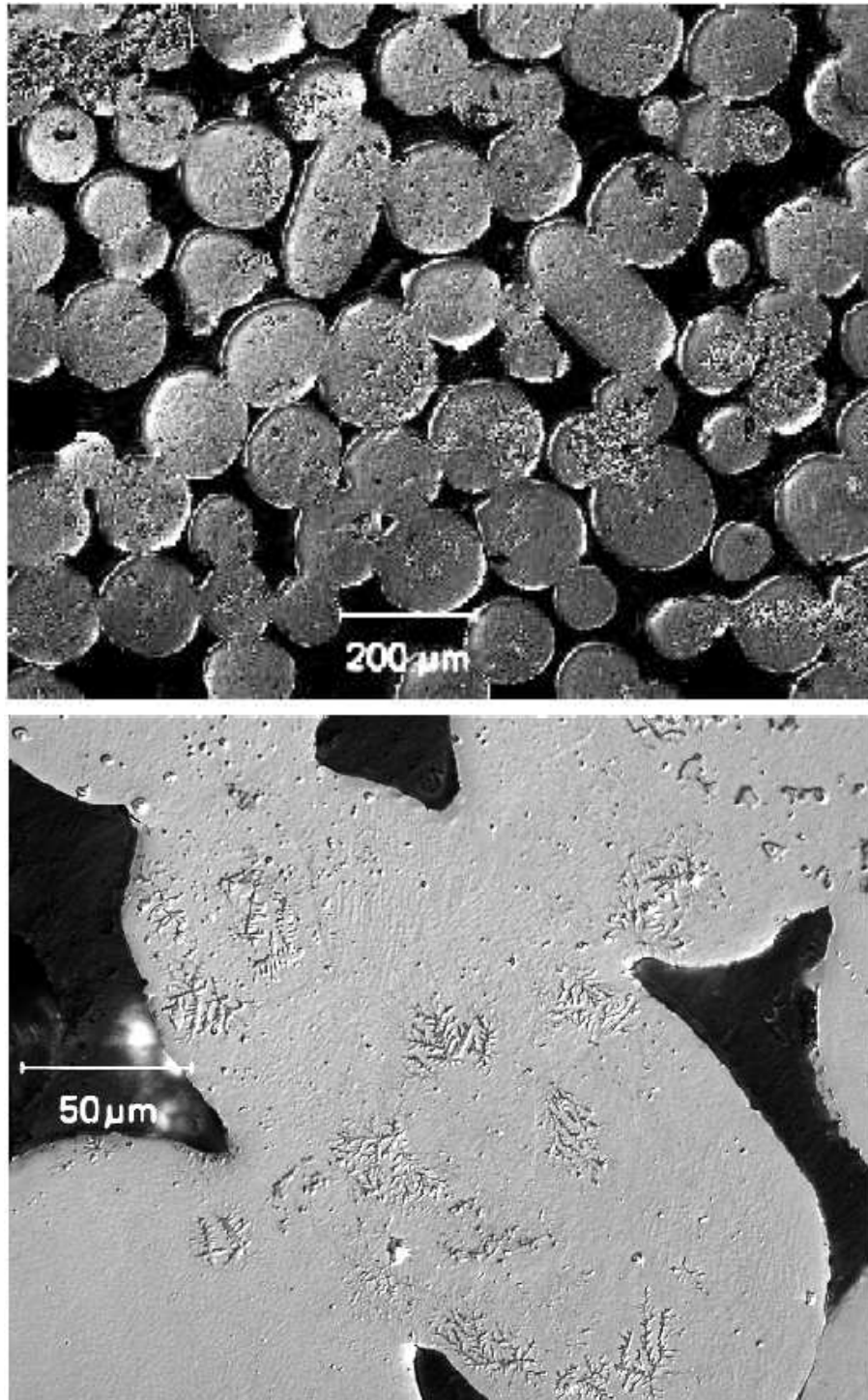
Fig. 16. Micrographs of consolidated samples.

C.   Post HIPing Procedures

Once the HIP has cooled completely from its run, the furnace is opened and the sample removed. Because of the high temperatures and long times used for the process, some diffusion occurs between the NiTi and the stainless steel container. This diffusion attaches the specimen tightly and the canister must be machined mostly away on a lathe, allowing the sample to be tapped out easily. After each sample is removed from its container, a constant set of post-HIP procedures are employed.

1.   Solution Heat Treatment

Each sample is fully cleaned with acetone in an ultrasonic cleaner to remove and machining oils and dirt. This cleaning is in preparation for a solution heat treatment (SHT), or solutionizing, of the material. Originally only a short treatment time was used as the widely used time is 1 hour at 900°C. Once a sample was solutionized by this standard method and taken to the microprobe, however, it became obvious that a longer time was needed to pull the $NiTi_2$ regions back into solution. Subsequent samples were treated at 1000°C for 10 hours with improved results. All samples are treated while encased in a vacuum-sealed glass ampule to prevent oxidation and water quenched. Quenching is needed to lock in the microstructure and prevent the growth of any precipitates or alternate phases which would form if the material was allowed to cool slowly. Fig. 17 shows the difference between samples treated at 1 hour and at 10 hours. The difference is most dramatic at junctions between powders as this is where the largest regions of $NiTi_2$ formed originally. Not only have the $NiTi_2$ regions dispersed into smaller regions, they seem to have dissolved back into the matrix. Again using image analysis, the first image contains 9% $NiTi_2$ and the second image only 3% $NiTi_2$. Although this is a welcome result and is the intended purpose of a solution heat treatment, it casts doubt on the previous conclusion made in section A of this chapter
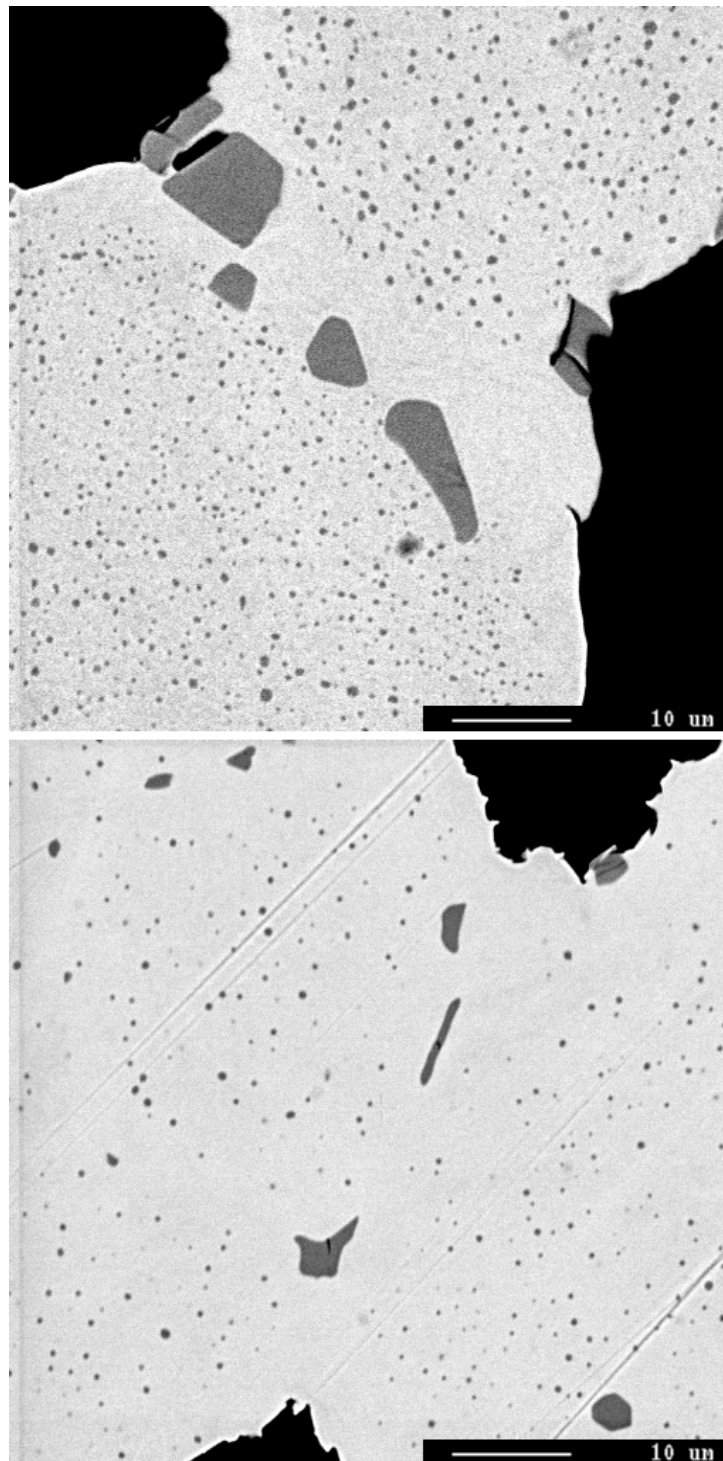
Fig. 17. BSE images of samples after short SHT (upper) and long SHT (lower).

about the electrode material being rich in titanium. By looking at the behavior of Ti-rich regions after solutionizing, it can be said that the material cannot be rich in Ti. At the SHT temperature NiTi is the stable phase. If the bulk material was completely composed of NiTi and the second phase was completely $NiTi_2$, there would be nowhere for the extra Ti to go as its current configuration is more stable than elemental Ti and there is no extra nickel to form more NiTi. The only conclusion is that there are regions of Ni_3Ti or even elemental Ni which are too small for the microprobe to detect. When the material is heated, the uncombined regions of excess Ni and excess Ti combine to form binary NiTi. When the original material was shipped, it was accompanied by a certification sheet which claimed a concentration of Ti-55.25wt.%Ni with some additional trace elements. This translates to Ti-50.2at.%Ni, a ratio which seemed to contradict information from earlier microprobe investigations, but now seems to be possible. It is thought that longer SHT times will result in a fully NiTi sample, but this time will increase exponentially as the second phase regions shrink. Further, when these regions reach the 0.5-1μm range, they will begin to favorably affect the performance of the material, rather than degrade it as they do now.

2.   Sample Preparation

After solutionizing, the material can be prepared for characterization. All cutting of NiTi is done on a low-speed gravity-fed saw equipped with a diamond embedded blade. Use of this saw ensures that the material is only minimally heated during cutting and the microstructure is preserved. Several small sections are cut from each sample for different investigations. First an interior sample between 10 and 20g is taken for thermal analysis in the Differential Scanning Calorimeter. Next a full slice is cut and mounted permanently with 2-part epoxy for polishing and viewing with a Leica MEF 4M metallograph. Once this epoxy is mixed and poured into a sizing container, the container, epoxy and sample are placed into a small vacuum chamber and evacuated for approximately 1.5 hours. Partially

curing under vacuum this way pulls air from all the pores and fills them with epoxy which allows for a better polish and a cleaner view under the metallograph. Preparation for the metallograph is done on a Struers Roto-Pol 31 with the Roto-Force 4 and Multidoser modules for specimen holding and polishing compound dosing, respectively. The samples are ground flat then polished with diamond suspensions down to 3μm. The final polish step is done with a 40/60 0.4μm colloidal silica/water suspension. Water reduces the acidity of the colloidal silica mixture to prevent etching during the final step. The remaining portion of the sample is prepared for compressive testing by turning the ends flat and parallel on a lathe. Normally such fast cutting is not desired because of the heat generated but in this case the ends are already near to flat from cutting on the diamond saw and the lathe is the cheapest and most reliable means of achieving the parallelism needed for testing.

CHAPTER III

CHARACTERIZATION OF POROUS SMA

In addition to the cursory inspection of a given HIP cycle's effectiveness in producing quality material, an extensive investigation was made into the thermal and mechanical properties of each sample produced, as well as rigorous determination of porosity, composition and heat treatment effectiveness. This chapter will present major trends in sample behavior across material produced by all HIP cycles used in the study.

A.   Thermal Investigation

Thermal scans were conducted on all samples to determine the four characteristic temperatures of each. The instrument used was a Perkin Elmer Pyris 1 Differential Scanning Calorimeter (DSC) which measures heat flow into and out of materials in the temperature range from -60°C to 600°C. The Pyris 1 DSC has a calorimetric accuracy and precision of $\pm 1\%$ and $\pm 0.1\%$ and a temperature accuracy and precision of ± 0.1°C and ± 0.01°C, respectively. For each sample, the heat flow is measured as a function of temperature across a range where transformation is expected. During the heating cycle the material will transform from martensite to austenite, a change observed as an increase in required heat for a given temperature change (endothermic). During cooling, the reverse transformation will occur and is seen as a decrease in the required outward heat flow to change the temperature by a given amount (exothermic). Results from a thermal scan on the pre-alloyed powders as received are shown in Fig. 18, which shows two curves. The upper curve shows normalized heat flow (W/g) into the sample during heating. The lower curve shows normalized heat flow out of the sample during cooling. From this it is clear that phase changes are occurring from the sudden change in slope of the heat flow curves. The software used to control the Pyris 1 and to analyze the data generated, Perkin Elmer Thermal Analysis 5.0, provides a
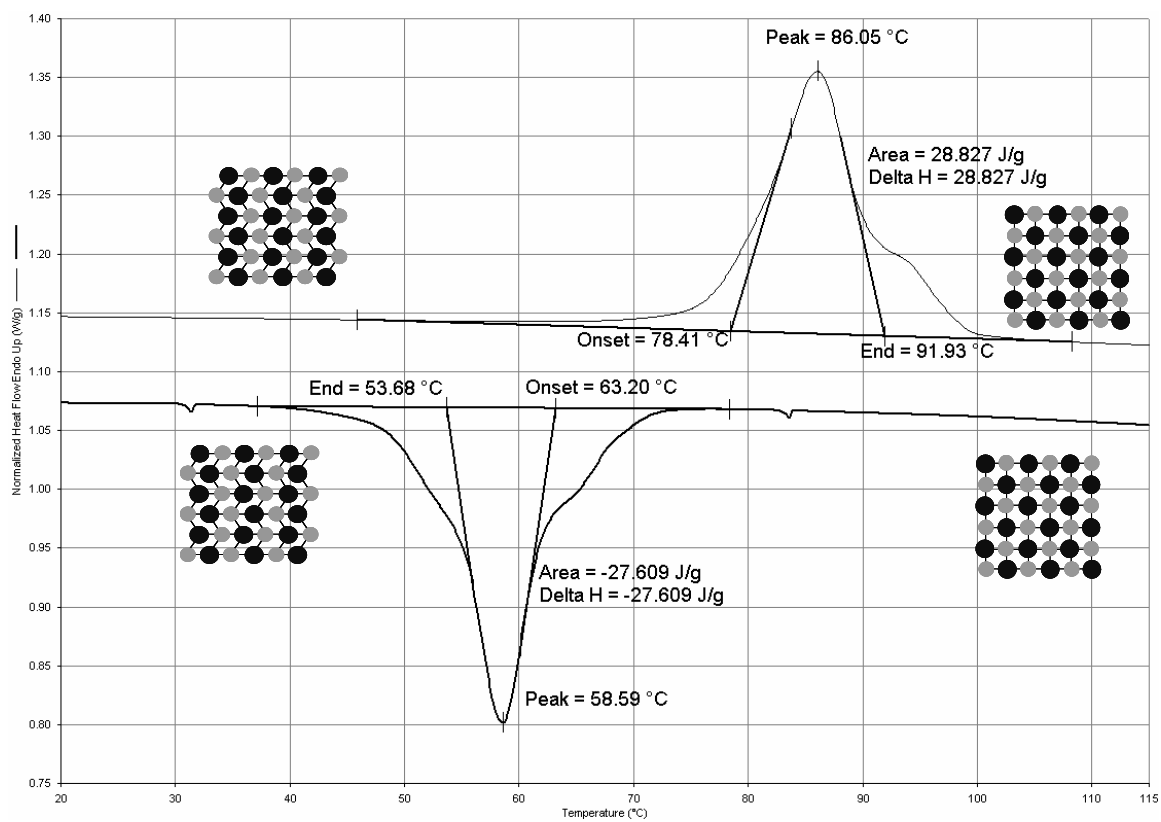
Fig. 18. DSC results for pre-alloyed powders.

powerful feature for determining the phase transformation temperatures. For each curve, the software can determine transformation onset and end by finding the intersection of extrapolated tangents from the baseline and the first inflection of the peak. The results of this function are shown in the graph as well. In order to clarify the meaning of the two curves shown in this graph, schematics of the material's current state are shown at either side of the transformation peak on both the heating and cooling curves. From this curve is can be seen that the transformation from martensite to austenite (upper curve) begins at 78°C and ends at 92°C. The reverse transformation begins at 63°C and ends at 54°C. Because the temperatures are found through tangent intersection, and subject to operator interaction, they are reported to the nearest degree only. These transformation temperatures are similar to what is expected from equiatomic material, which is to be expected given the composition discussed in previous chapters. Thermal scans were also conducted on HIPed material, representative results of which are shown in Fig. 19. This material has similar transformation temperatures to the powders as received, but with a small increase in all temperatures. The heating transformation, from martensite to austenite, begins at 90°C and finishes at 106°C. During the cooling step, a transformation from austenite to martensite is encountered first at 76°C and continues until 63°C. Observing the differences in composition between the powders as received and the material after HIPing shows the reason for a temperature shift of this kind. Large regions of $NiTi_2$ will create high stress concentrations due to a mismatch of stiffnesses between themselves and the surrounding material. Examining Fig. 4 shows that with this internal stress level raised above that of the powders the transformation temperatures will also raise. Including this result and results from other samples after HIPing (see Appendix B), the average A_f temperature was found to be 105°C with a standard deviation of 6.5°C.

After solutionizing, the material was again scanned for transformation temperatures. It was expected that all temperatures would decrease based on the decreased internal stresses
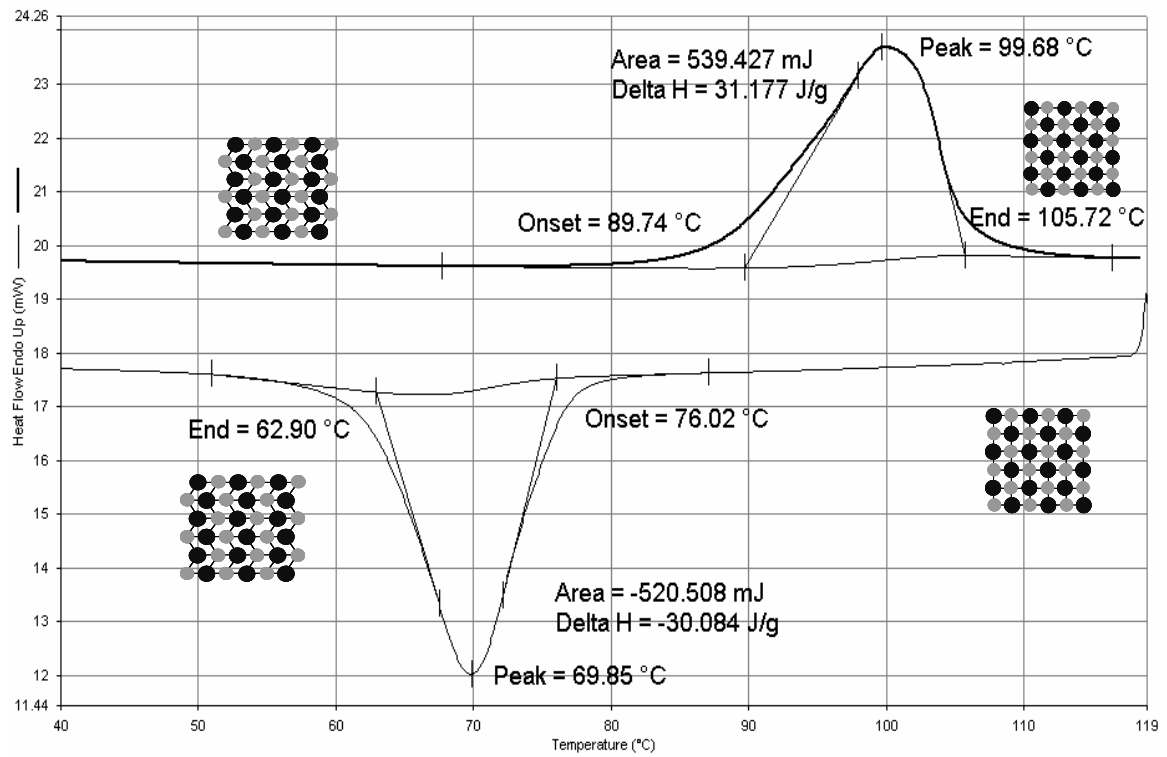
Fig. 19. DSC results for HIPed material.

resulting from a fully homogeneous composition. Ideally, the thermal behavior should match that of other Ti-50.2at.%Ni alloys, reported by such researchers as Liu and Galvin [25] and Strnadel et al. [73], which typically have an A_f of approximately 60°C. As stated in Chapter I, this temperature will decrease as the nickel content increases. Of course, this is for material with no special processing history and the addition of heat treating or mechanical working can significantly alter a material's thermal response. The thermal properties, in fact, did not noticeably change from the HIPed material. In one sample which is presented in the mechanical testing section, however, the temperatures were reduced by about 40°C. This sample was of a much smaller diameter than the other samples and it is believed that the oxidation effects were able to reach the interior of the sample, leeching out titanium and causing the material to be nickel rich. All the DSC results from solutionized material are shown in Appendix B. The average A_f temperature was 84°C with a standard deviation of 36.7°C. The low average and high deviation is cause by the single anomalous result.

B.   Composition Analysis

Some results of composition analysis were presented in an earlier chapter. Continuing with this investigation, HIPed material was analyzed to discover any changes to the composition which may have occurred during processing, the results of which are presented in Figs. 20–24. The first sample analyzed was in an as-HIPed condition, where no additional treatments had been performed after HIPing. The second sample had undergone a short solution heat treatment after HIPing, an image of which was shown previously in Fig. 17(upper). The third sample investigated had undergone a long solution heat treatment (10hrs) and was previously shown in the lower part of Fig. 17. For each sample, several images were taken using backscattered electrons (BSE). This technique produces greyscale images with shades from white to black depending on composition. BSE images

of these three materials are shown in Figs. 20, 22 and 24. In each of these images, two phases are clearly present. Other capabilities of the microprobe can be used to determine the composition of each phase.

The Energy-Dispersive X-ray Spectrometer (EDS) was employed with these samples to obtain a qualitative picture of the composition, the results of which are shown in Figs. 21 and 23. The upper image in both figures shows the result of analyzing the lighter of the two phases and the lower image is from the darker of the two phases. Although no elements other than the nickel, titanium and carbon (from the mounting medium) are observed, it is clear that the two phases are of differing ratios of nickel and titanium.

The as-HIPed material (Fig. 20) shows a coalescence of the second phase which was present in dendrites in the powders before HIPing. To determine the composition of both phases, Wave-Dispersive X-ray Spectrometer (WDS) analysis was performed on this material just as was done on the electrode material. Table II shows the results of WDS analysis on several light regions and several dark regions. Values reported are the averages of all analysis. Also shown are the standard deviations for each element in each analysis which show that the deviation is well within the error of the instrument. The lighter phase is, as expected, an equiatomic region of Ni and Ti and the darker region is NiTi$_2$. The BSE image of the as-HIPed sample shows a major part of the second phase, which has no shape memory properties, converged near the junctions between powders. When a force is applied to this material globally, it will be transferred almost exclusively to the narrow junctions. For this reason, it becomes extremely important to minimize the second phase formation at the junctions. A first attempt at this was a short solution heat treatment (SHT) of 1 hour at 900°C. As is apparent in Fig. 22 this treatment had little effect on the composition of the material. Imaging and EDS analysis show that the quantity of each phase and compositions of each are unchanged. After this, a much longer SHT was employed, with greater success. The temperature for this treatment was raised to
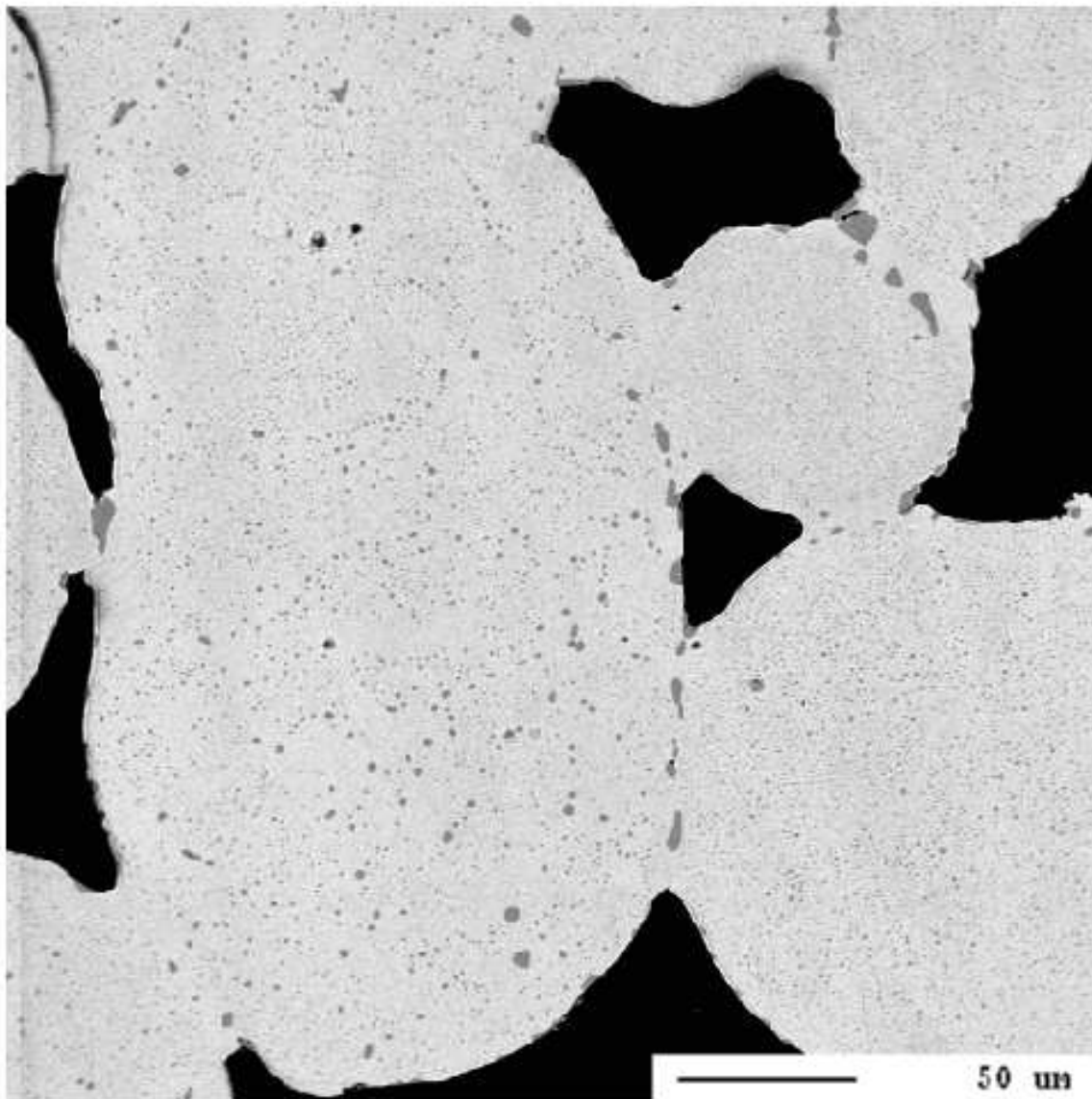
Fig. 20. BSE image of as-HIPed material showing large amounts of NiTi$_2$.
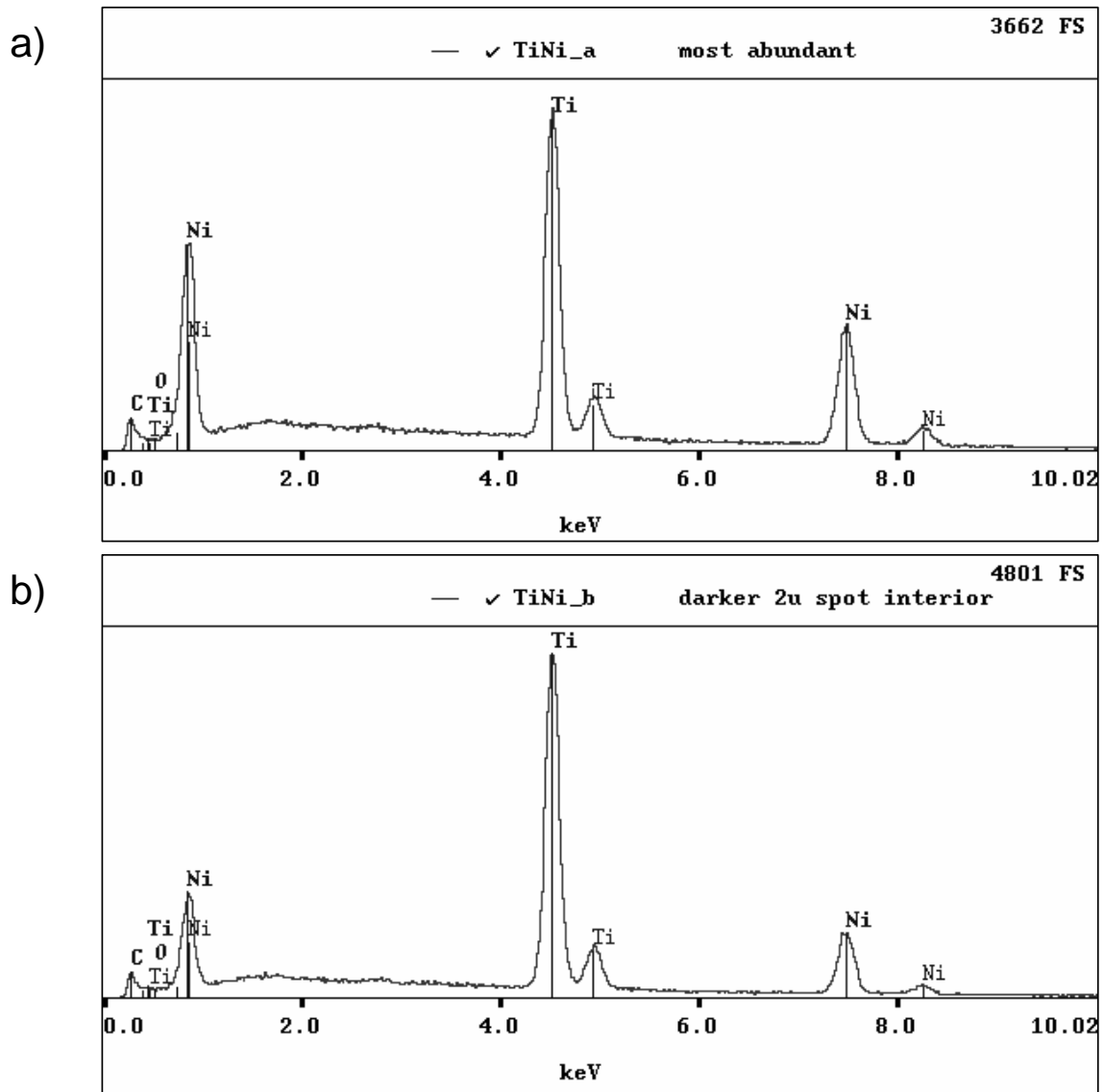
Fig. 21. EDS analysis of as-HIPed material in a) light regions and b) dark regions.
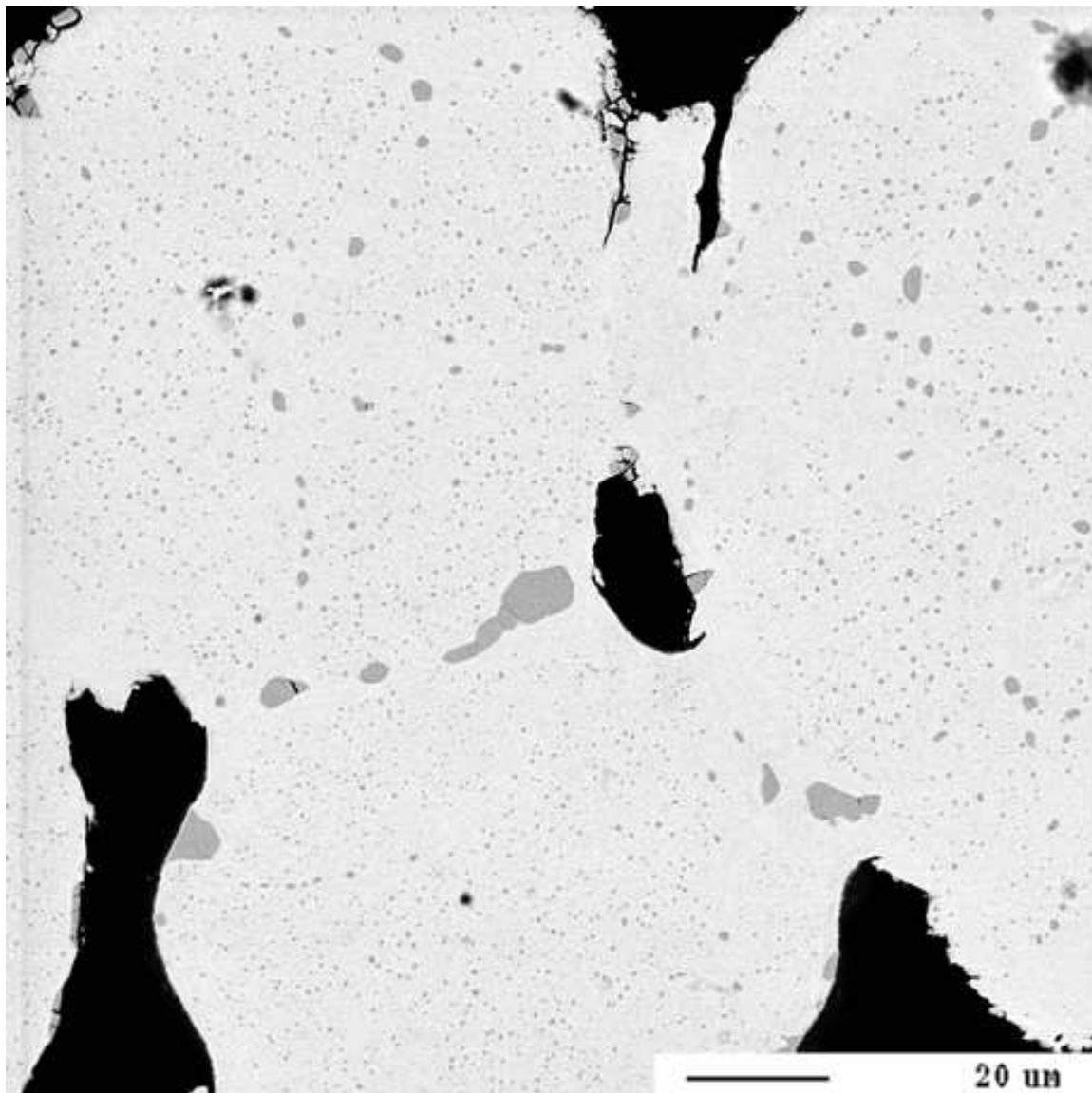
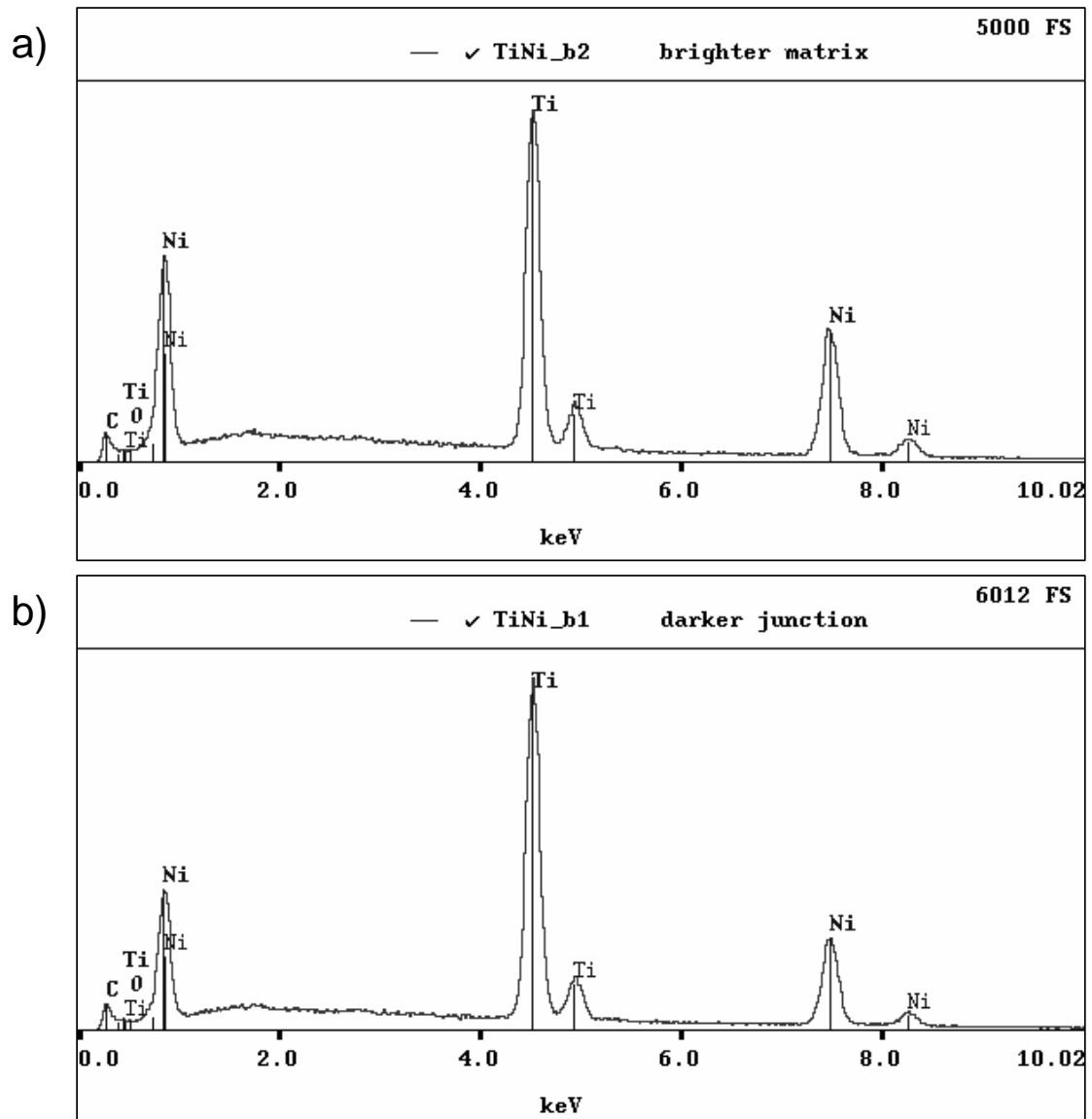Fig. 22. BSE image of HIPed material after a short SHT showing large amounts of NiTi$_2$.

Fig. 23. EDS analysis of HIPed material after a short SHT in a) light regions and b) darker regions.
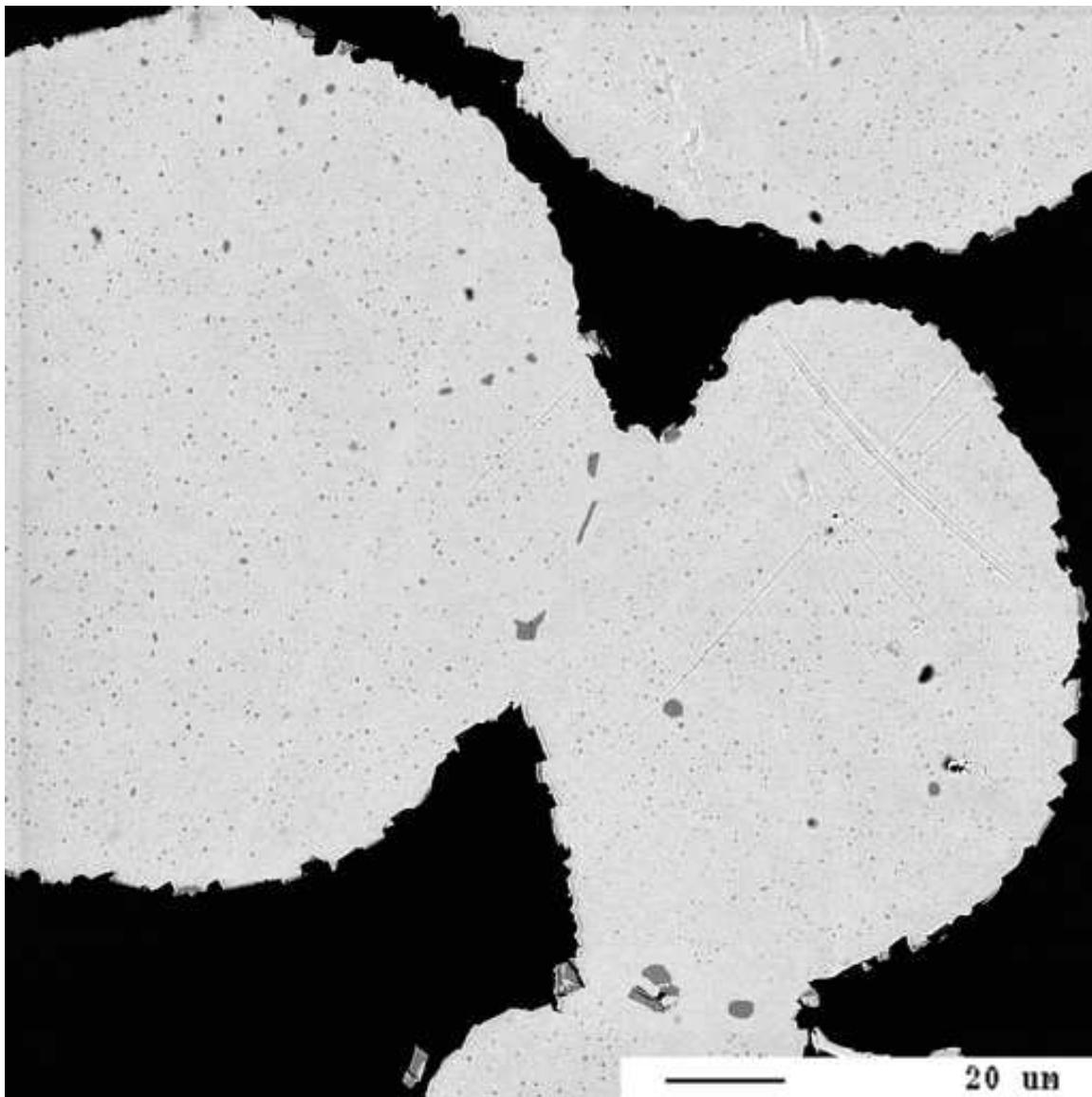
Fig. 24. BSE image of HIPed material after long SHT showing reduced amounts of second phase.

Table II. Averages and standard deviations of elemental analysis of two phases within as-HIPed material using WDS analysis (error: $\pm1\%$).

	Ni (at%)	Ti (at%)	O (at%)
Light Regions	49.7	49.2	1.1
St. Dev.	0.162	0.396	0.558
Dark Regions	31.6	61.7	6.7
St. Dev.	1.102	0.810	0.300

1000°C and the time lengthened to 10 hours. The results were encouraging as a marked difference in second-phase content was observed (Fig. 24). By employing basic image analysis, qualitative information about second-phase content was obtained.

Image analysis software used was the freely-available Scion Image, a PC clone of NIH Image produced by the Scion Corporation. First the region of interest was isolated from the surrounding areas (i.e. epoxy) and the second phase highlighted by selecting an appropriate color range. Once this was done, the software can calculate area percentages for the highlighted and non-highlighted areas. A screen capture of this process is shown in Fig. 25. The red areas are second-phase pockets which are highlighted for measurement. The black region is the mounting epoxy which is excluded from measurement. This analysis was performed on the three samples shown above to determine how effective each heat treatment was in eliminating the second phase. Several images were taken of each sample and each image contained different regions and sometimes different magnifications. Table III shows the result of area percentage analysis for every image and the average values across all images. This table shows that the amount of second-phase regions decreased
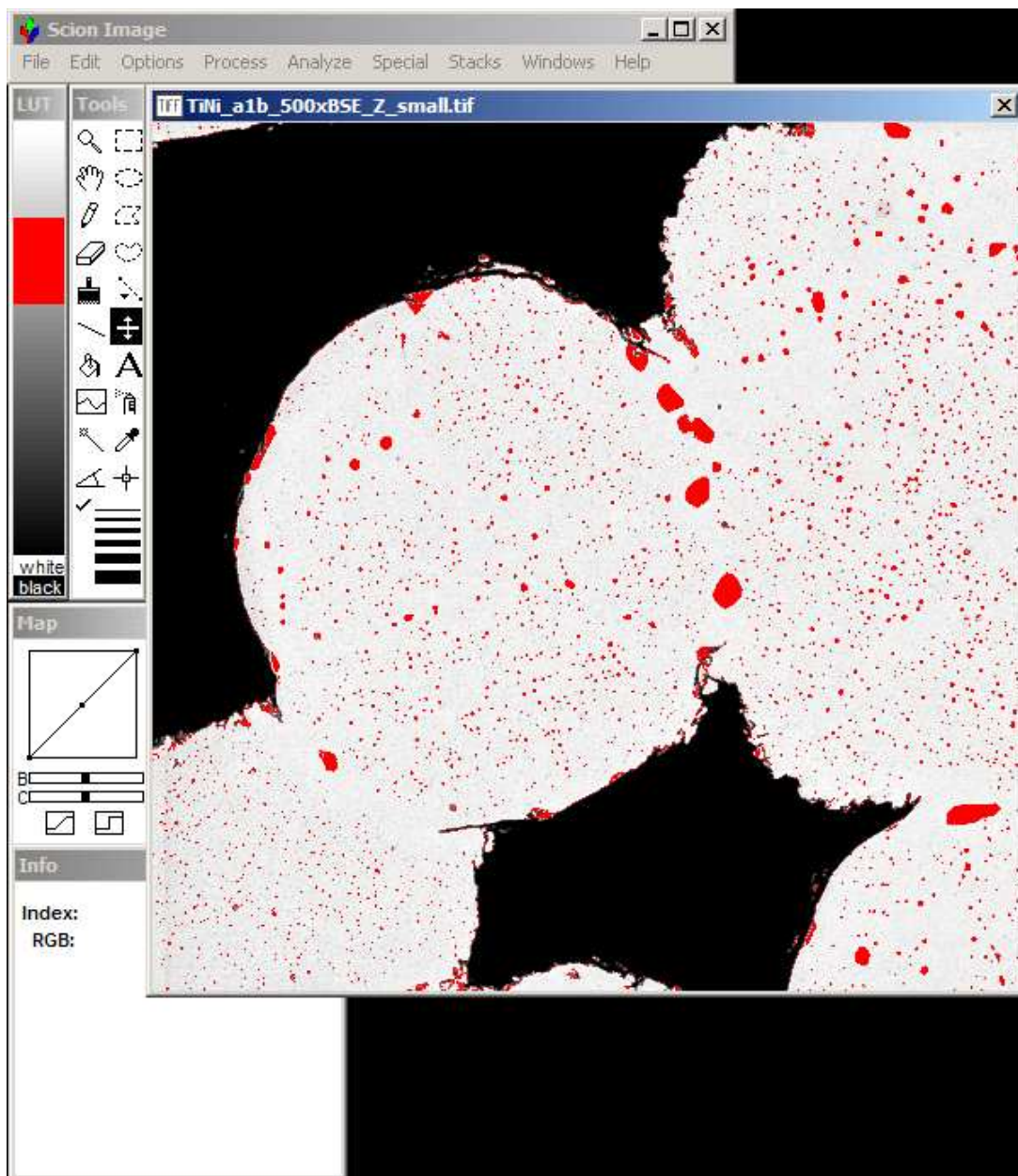
Fig. 25. Screen capture during area percentage calculation.

Table III. Area percentages of second-phase regions in materials with differing heat treatments.

Image Number	Light Region (%)	Dark Region (%)
As-HIPed		
1	95	5
2	95	5
3	95	5
4	89	11
5	95	5
Avg. %:	93.8	6.2
Short SHT		
1	93	7
2	95	5
3	97	3
4	92	8
Avg. %:	94.25	5.75
Long SHT		
1	97	3
2	97	3
3	98	2
4	95	5
5	96	4
Avg. %:	96.6	3.4

with each treatment with a sharp decrease when the SHT time was increased tenfold over the initial SHT time. Unfortunately this data also shows that the decrease in $NiTi_2$ content is not a linear function of SHT time. With a .45% difference between no treatment and a 1 hour treatment, a linear relationship would give only 1.7% $NiTi_2$ content after a 10 hour treatment (starting from 6.2% initial area), which is not the observed result. As the BSE images show, much of the area taken up by $NiTi_2$ in the last sample is within the powder and not in the junction region. This important observation shows that heat treating was able to disperse the second phase from the area which has the most impact on material performance.

C.   Quasi-static Testing

Mechanical performance is the most revealing and important measure of this material's quality. The goals for the material produced in this study were 4% recoverable strain utilizing the shape memory effect and 3% strain recovery utilizing the pseudoelastic effect. These goals were based on past experience with porous SMA and meeting them would make this study's result competitive with the other material. Compressive quasi-static testing was performed on HIPed samples to test for both SME and PE. Testing was performed using an MTS 810 hydraulically driven mechanical testing system outfitted with a 55 Kip load cell. Engineering strain measurements were taken directly using a $1''$ strain gage manufactured by Epsilon Technology Corporation, which in most tests was adapted to a $1/2''$ gage length. Elevated temperatures tests were performed using a Research Industries Quad Elliptical E4-10 quartz lamp furnace controlled to $\pm 1°C$ by an Omron E5AX-A

temperature controller. Low temperatures down to -5°C were achieved with CO2 pumped into a partially sealed chamber. In order to maintain temperature, the gas release was controlled by an electromagnetic valve actuated by the temperature controlled mentioned earlier. Feedback for this controller was provided by a K-type thermocouple attached directly to the test article. Fig. 26 shows the MTS system with temperature controller (bottom left) and furnace (center). The lower picture shows a close-up of the furnace with the sample installed. Applied load was compressive for all the quasi-static tests so to simplify presentation, compressive stress and strain will be reported as positive values. Also, the stress is a simple macroscopic value based on the applied force and the measured diameter of the sample and the strain is a macroscopic value read directly from the extensometer which measures elongation in one dimension. It should be noted that local strains will be much higher than the reported macroscopic strain due to the structure of the particle junctions. The as-HIPed sample discussed in this section had an aspect ratio (L/D) of ∼2, the remaining samples had an aspect ratio of ∼1. This change was due to a conservation of material and also to examine higher strain levels without buckling.

Fig. 26. MTS test system showing furnace and testing fixture.

1. Shape Memory Effect

To test for the shape memory effect, the sample is cooled below M_f and then loaded at a temperature at least below A_s to de-twin the martensite. After unloading, the sample is heated to recover austenite and the original shape. The stated goal for this type of test is a 4% recovery, which means that 4% of the imparted strain will be recovered during the post-test heating step. This goal was exceeded by all the material produced in this study and the samples with a long solution heat treatment performed exceptionally well.

First, as-HIPed material was tested for the shape memory effect, Fig. 27 shows the stress-strain response of this test. Test temperature was 25°C, well below the A_s temperature of 89°C. A columnar sample was loaded incrementally to a maximum strain of 7% at 170.96 MPa. During unloading, 0.85% of the imparted strain was recovered beyond elastic unloading. This small amount of strain is not attributed to any shape memory properties as there is no transformation possible during this test segment. Because this is a porous material and not all of the powders are attached to their neighboring powder, some sliding occurs when the piece is compressed. On unloading, these powders return to their original position, but with a delay caused by friction. This delay shows as a nonlinear unloading path. When this sample was soaked at 200°C for 30 minutes to recover the austenitic shape, 2.9% strain, or 41% of the imparted strain, was recovered. While this nearly meets the goals set for this study, the performance is not ideal and could likely be improved with thermomechanical treatments.

In order to improve the stress-strain response seen above, samples were treated with the short solution heat treatment mentioned earlier. Testing on this material was performed again at 25°C, below the A_s temperature of 93°C. Force was incrementally applied to a load level of 227.3 MPa where strain was 7%. This loading path can be seen in Fig. 28. The same sliding effects are seen here, and are not counted in the recovery total. Dur-
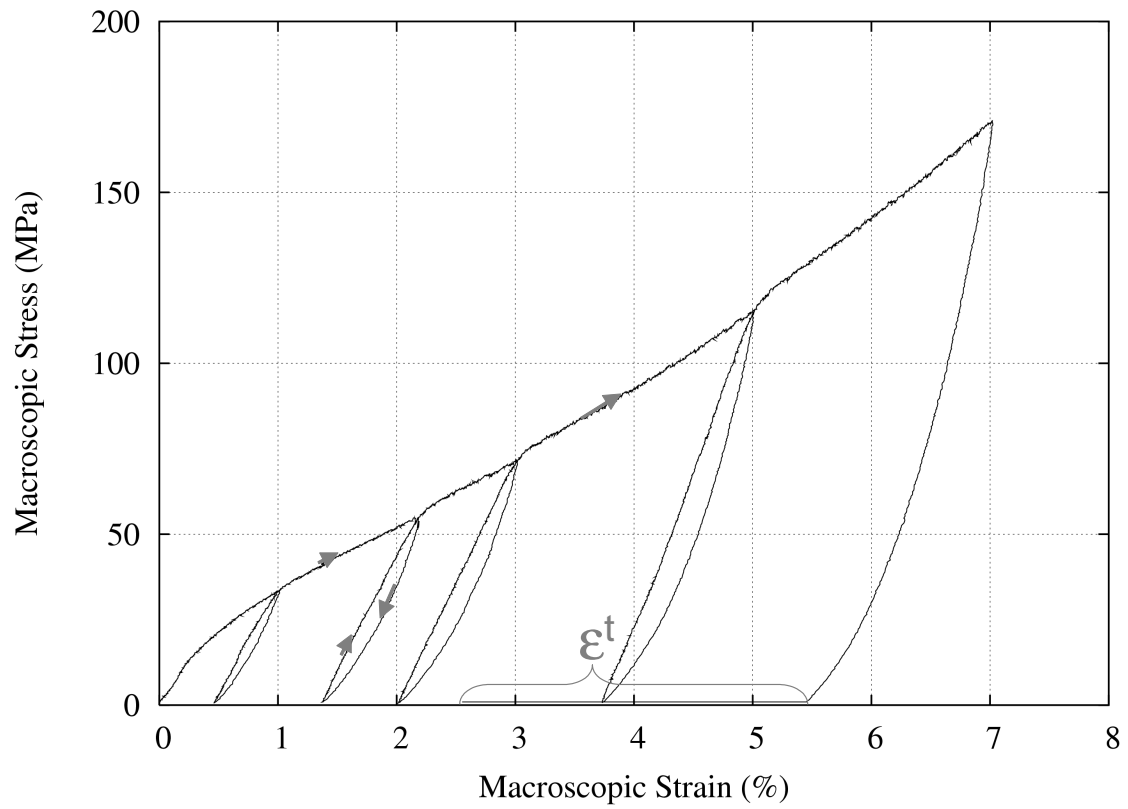
Fig. 27. Results of testing for SME on as-HIPed sample. Test temperature was 25°C, A_s temperature was 89°C.

ing heating 4.25% strain was recovered, surpassing the stated goal of 4%. By examining this material in the microprobe after having undergone a short SHT, it was believed that further improvement to the composition microstructure, and thus a performance improvement, could be made by increasing the time and temperature of the treatment. As such, additional material was treated with the long SHT mentioned in Chapter II and tested. The stress-strain response is shown in Fig. 29. Testing for the shape memory effect had to be done below room temperature as the heat treatment caused the transformation temperatures to shift lower by about 60°C. By performing the test at 0°C, the material was held below its A_s temperature of 18°C. After loading incrementally up to 6.81% strain at 154.33 MPa, the material was unloaded and the recovery behavior was observed. During the short heating after testing, 4.4% strain was recovered. This is promising as it shows an increase above the materials with less solutionizing and may lead to increased pseudoelastic performance as well.

Table IV. Summary of key features of testing for the shape memory effect.

	Max Strain (%)	Max Stress (MPa)	Recovery During Heating
As-HIPed	7.02	170.96	2.90
Short SHT	7.00	227.34	4.25
Long SHT	6.81	154.33	4.41

Although the partially and fully solutionized materials both met the required 4% recovery goal as stated before testing began, a significant improvement could be seen through
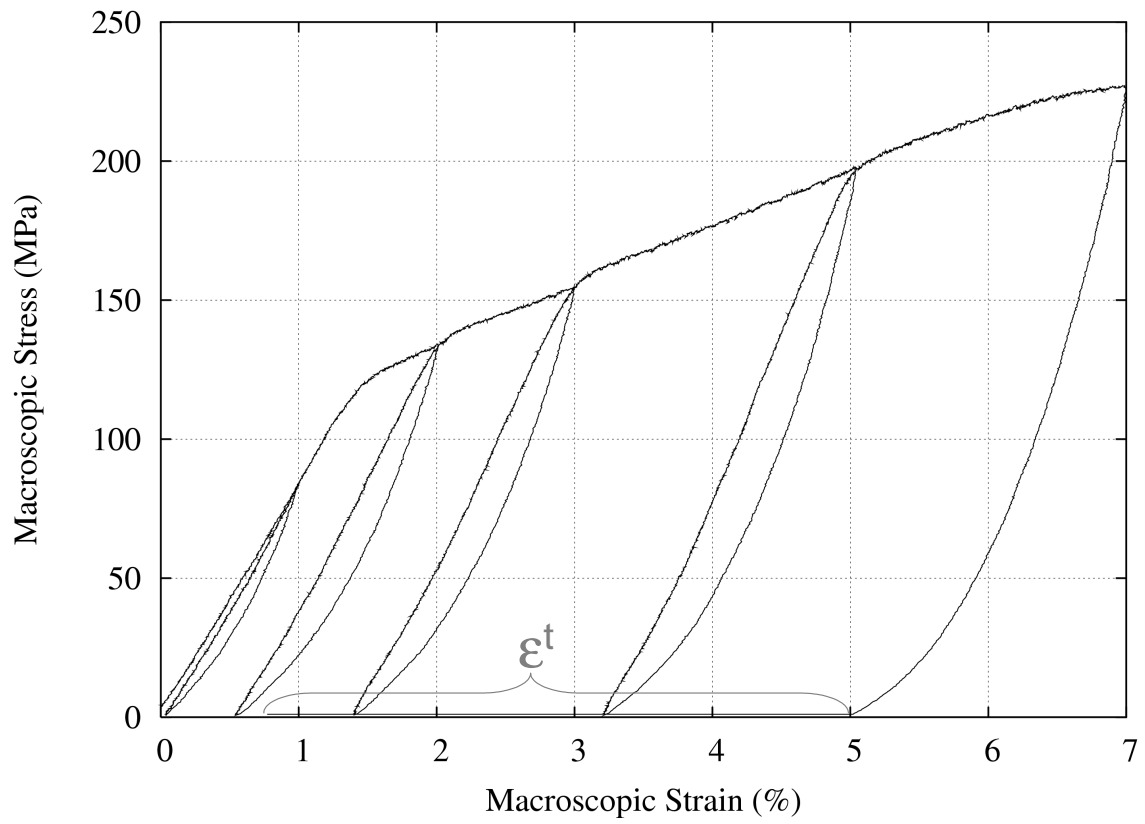
Fig. 28. Results of testing for SME on sample after a short SHT. Test temperature was 25°C, A_s temperature was 93°C.
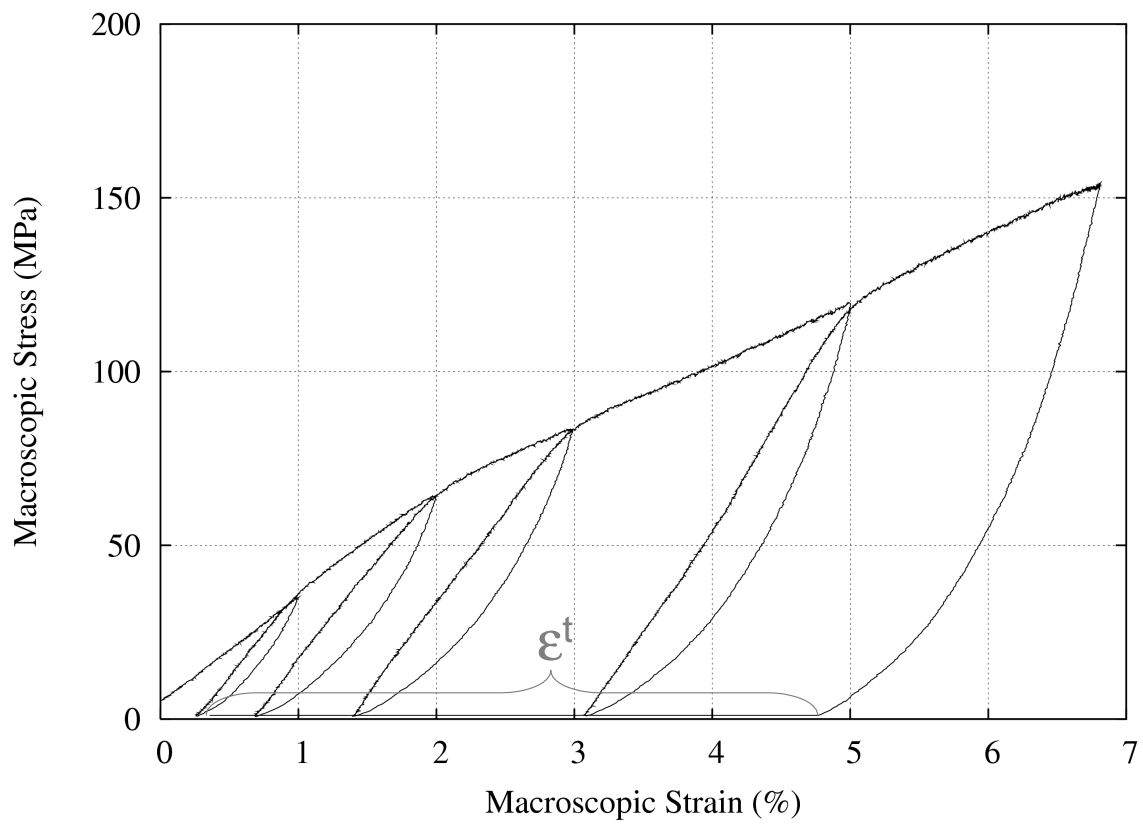
Fig. 29. Results of testing for SME on sample after a long SHT. Test temperature was 0°C, A_s temperature was 18°C.

modification of the heat treatment schedule. In order to easily understand the differences between all these tests, a table is presented which summarizes the key features of each test (Table IV).

2. Pseudoelastic Testing

Many applications of shape memory alloys, both dense and porous, require excellent pseudoelastic performance. This material is no exception and testing for pseudoelastic behavior was carried out in much the same manner as the shape memory effect testing described in the previous section.

The as-HIPed material was tested at 111°C, a few degrees above the A_f temperature of 105°C. Stress-strain response was measured and is presented in Fig. 30. This figure shows the incremental increase in load up to a maximum macroscopic stress of 169.61 MPa where the strain was measured to be 8%. Because of the direct austenite–martensite–austenite transformation which is characteristic of pseudoelasticity, it is expected that most of the strain will be recovered during unloading. When this material was unloaded, however, less than 1% was recovered. During the subsequent heating an additional 4.7% was recovered. This was not the desired behavior and it was thought again that the existence of NiTi$_2$ regions inhibited the reverse transformation. To test this theory, materials having undergone a solution heat treatment were tested for pseudoelastic behavior. Fig. 31 shows the stress-strain response of a sample after undergoing a short solution heat treatment. This sample was loaded to a maximum stress of 214.9 MPa where the strain was measured to be 7%. On unloading the material recovered 1.5% of that strain and an additional 2.7% during heating. This result shows that the behavior in pseudoelasticity is also improved with solution heat treatments, which is expected after the improvement to the SME performance.

Fig. 32 shows the stress-strain response of material tested after having undergone the long heat treatment. Accordingly with the DSC, the test temperature was adjusted to 50°C,
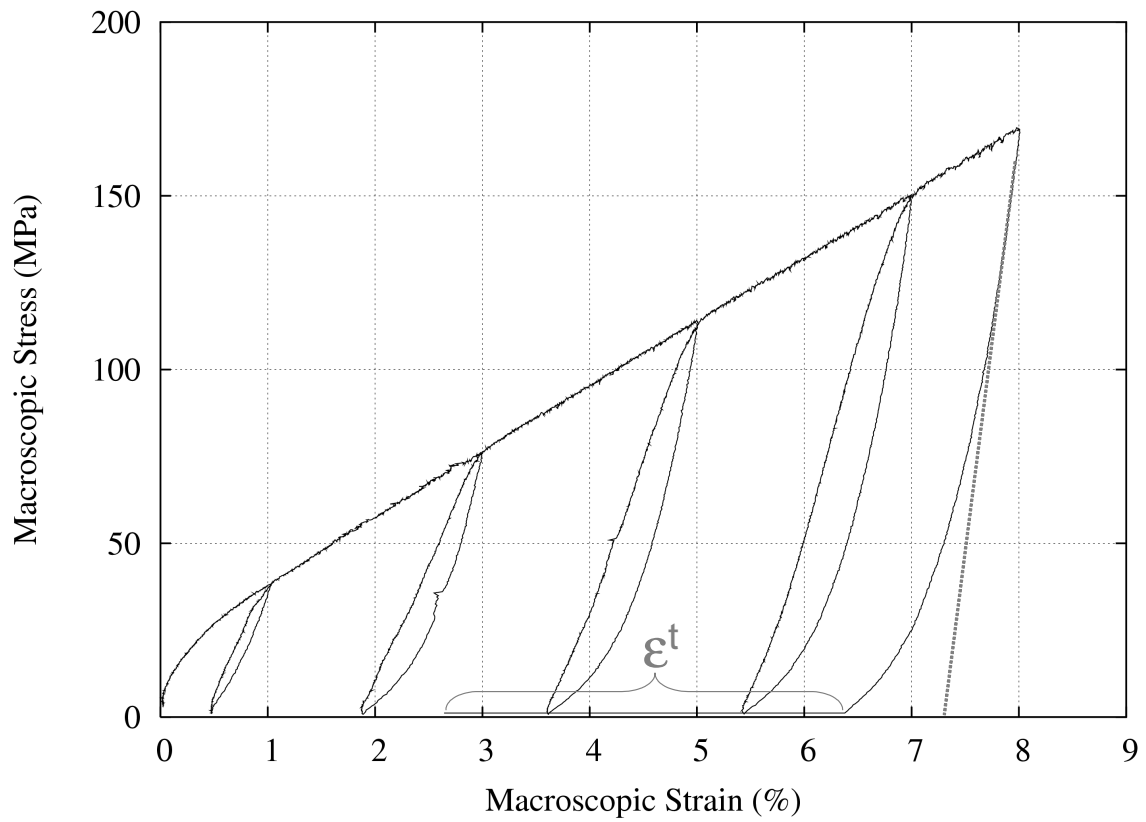
Fig. 30. Results of testing for PE on as-HIPed sample. Test temperature was 111°C, A_f temperature was 105°C.
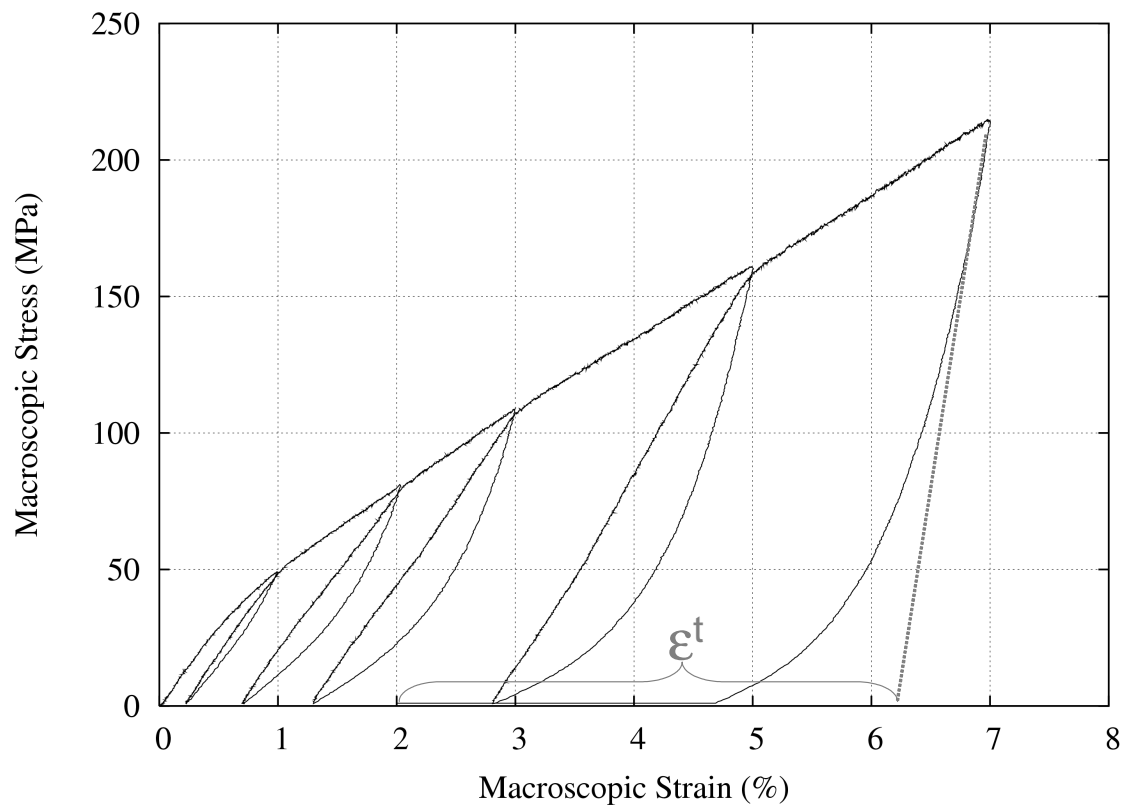
Fig. 31. Results of testing for PE on sample after a short SHT. Test temperature was 120°C, A_f temperature was 105°C.

just above the A_f temperature of 42°C. The maximum stress reached was 181.66 MPa where the strain was measured to be 7.3%. On unloading the sample recovered 1.7% of that strain and an additional 4.6% during heating. The strange region near zero load on each unloading was caused by a small misalignment in the testing fixture. Although a seemingly small improvement over the material with only a short heat treatment, a side-by-side comparison as shown in Table V, reveals a steady improvement with the increase of heat treatment time. It should be noted here that some portion of the strain recovered during unloading is due to the effects of powders sliding past one another during compression. As it is impossible to separate the two sources of nonlinearity, the recovered strain will be reported as any strain are presented in Appendix C.

Table V. Summary of key features of testing for pseudoelasticity.

	Max Values		% Strain Recovered		
	Strain	Stress	Unload	Heating	Total
As-HIPed	8.01	169.61	0.97	3.73	4.71
Short SHT	7.00	214.88	1.49	2.69	4.18
Long SHT	7.30	181.66	1.70	4.60	6.30

Although the materials tested here showed the ability to recover large amounts of strain, this could only be done through post-test heating. To examine the temperature dependance of strain recovery, similar samples were tested at varying temperatures above A_f up to 175°C. The high temperature testing was intended to cause transformation in any material with a stress-raised A_f. Fig. 33 shows the results of this testing (the curves have
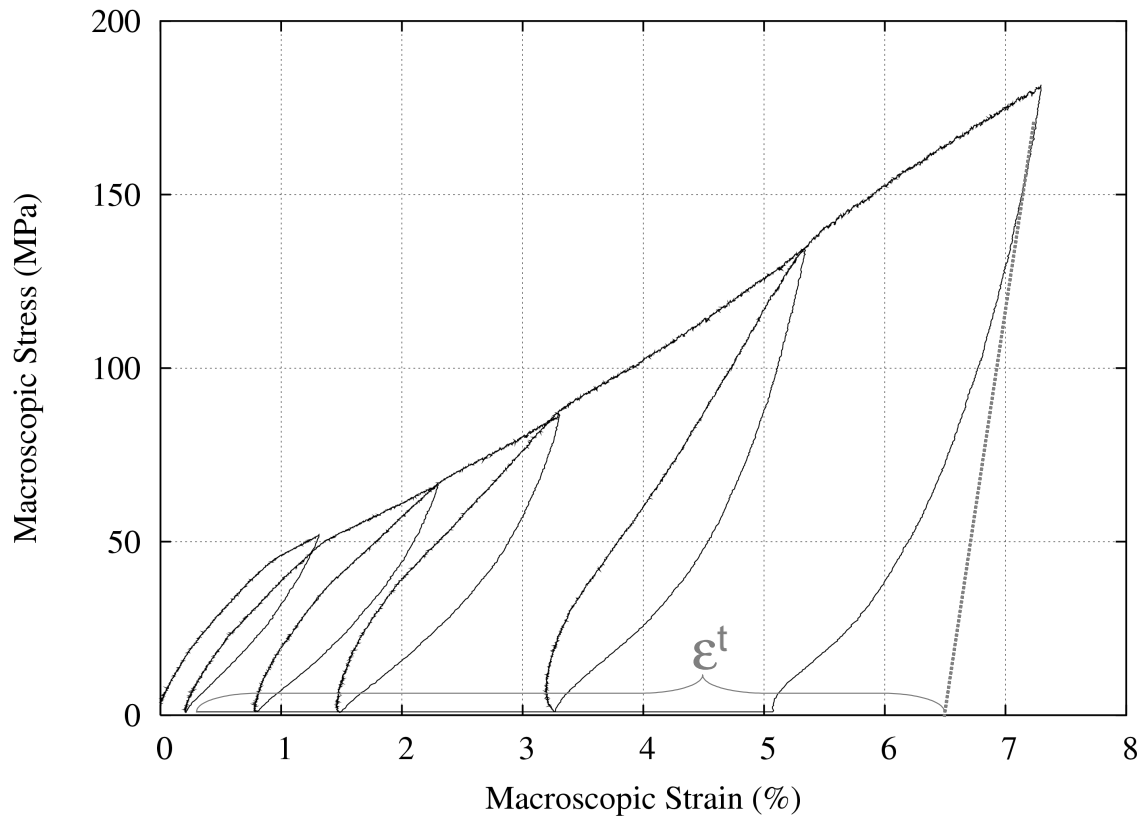
Fig. 32. Results of testing for PE on sample after a long SHT. Test temperature was 50°C, A$_f$ temperature was 42°C.

been artificially smoothed for clarity). Although the stiffness increases in each case due to the delayed start of the martensite transformation, the recovery paths are very similar. In fact, in each case the max strain is identical and the final strain is extremely close. As the three samples were subjected to similar, but not identical, processing steps, the correlation means that there is no advantage to testing at any of these three temperatures.

3.   Thermomechanical Treatments

It has been shown by several researchers that a narrow range of conditions must exist for pseudoelasticity to occur [25], [73]. This set of conditions can be created by various types of thermomechanical treatments, mentioned in Chapter I, which were employed with material in this study to enhance its performance beyond the levels achieved by solution heat treatments alone. Specifically, the correct interaction between temperature, applied load and internal stresses will result in a material which exhibits good performance in both SME and PE. The fist method for creating the proper balance between these factors is a purely mechanical treatment. By cooling the material below M_f and deforming it beyond its elastic region, a dislocation field will be created that is beneficial to the reverse transformation so crucial to pseudoelastic performance. The level of deformation required varies, but has been reported as 2-5% more than is required to finish detwinning completely. Unfortunately for this study, porous SMAs do not respond with the same stress-strain profiles as dense SMAs. This is due to the constantly changing stress field caused by pore collapse and powder compression, both of which change the current cross-sectional area. While this feature of porous SMAs is the main reason for their ability to demonstrate large strains without failure, it also prevents the appearance of a clear beginning and end of transformation as different parts of the material transform at different load levels. Without a clear transformation and the appearance of a detwinning plateau as a marker, a different guideline had to be determined.
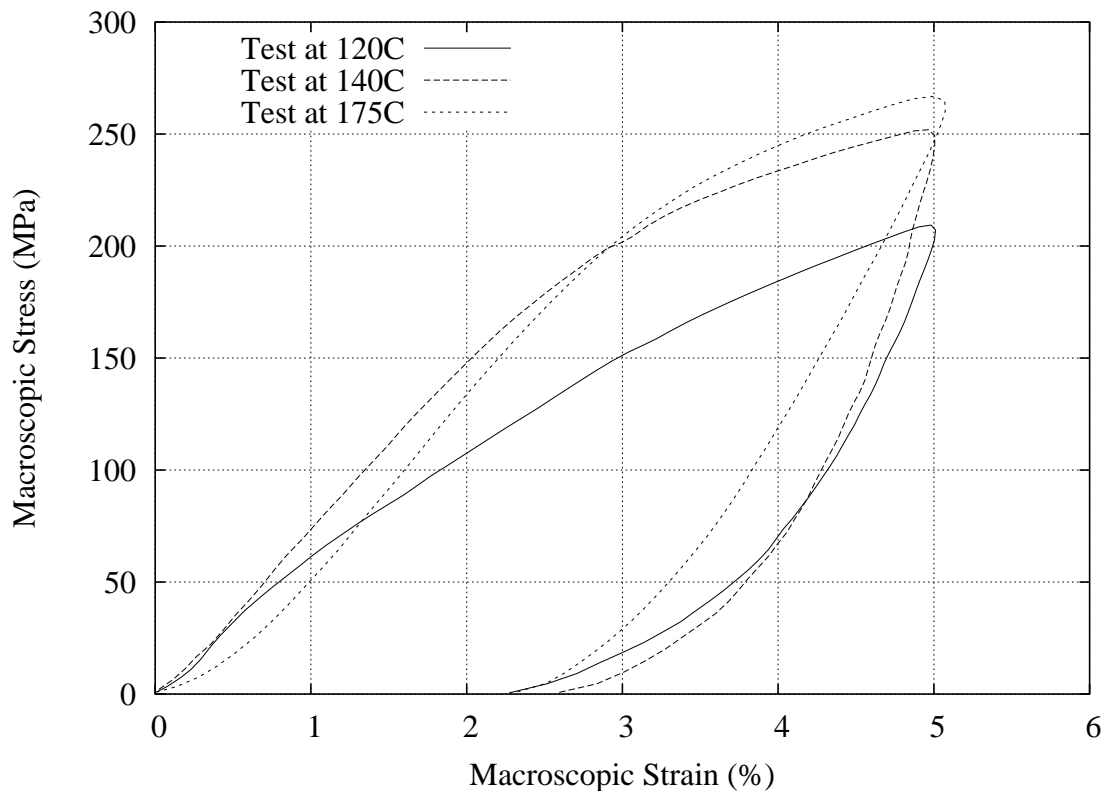
Fig. 33. Stress-strain response of similar materials tested at three temperatures.

When creating SMA actuators, a training procedure is utilized which involves continually cycling the material thermally or mechanically until the subsequent displacement or loading paths are identical[74]. Training in this way ensures that future behavior will follow the same path as no more significant plastic strain is expected to occur. Following a similar idea with material in this study, a sample was strained to 5% in martensite then heated to 200°C for half an hour to recover the transformation strain. Each cycle induced less plastic strain than the previous one, and after several cycles the sample did not show any significant additional plastic strain. During the first few cycles, in addition to gaining permanent strain, the effective stiffness of the material increased (see Fig. 34). This is due to the collapse of connective regions between powders, areas with the smallest area and highest stress. After the initial permanent set associated with the collapse, additional plastic strain is associated with dislocations within the powders which are beneficial to the reverse transformation crucial to good pseudoelastic performance. Fig. 35 shows the stress-strain response of the same sample at the same temperature before and after this training procedure. The increase in stiffness is apparent as well as the ability of the trained material to recover more strain than the untrained material. Close examination of this figure shows that the unloading slopes are almost identical, almost as if the trained sample is shifted slightly upwards. This shows that there is no fundamental change happening during the training process, but only that the weaker regions have collapsed, allowing the powders to bear the stress and transform within the same strain range. In addition, this means that regions on the stress-strain curve of untrained material which looked like detwinning or austenite to martensite transformation were actually a combination of both transformation and collapse. Further obscuring this fact was partial recovery of the pore collapse during the post-compression heating stage. With the weaker connections fully collapsed, the portion of recovery due to their recovery was taken out of the recovered strain during heating.
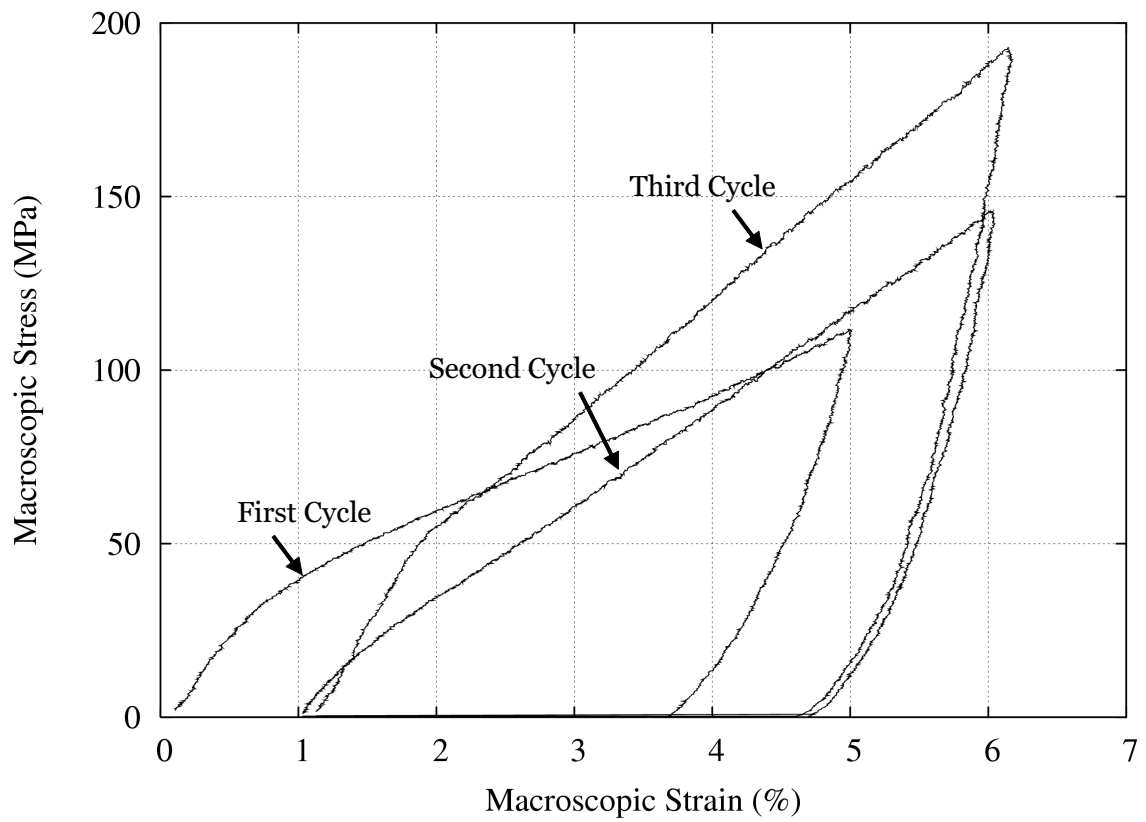
Fig. 34. Stress-strain plot during training showing stiffness increase during first three cycles. Test was performed at 25°C, M_f was 61°C.
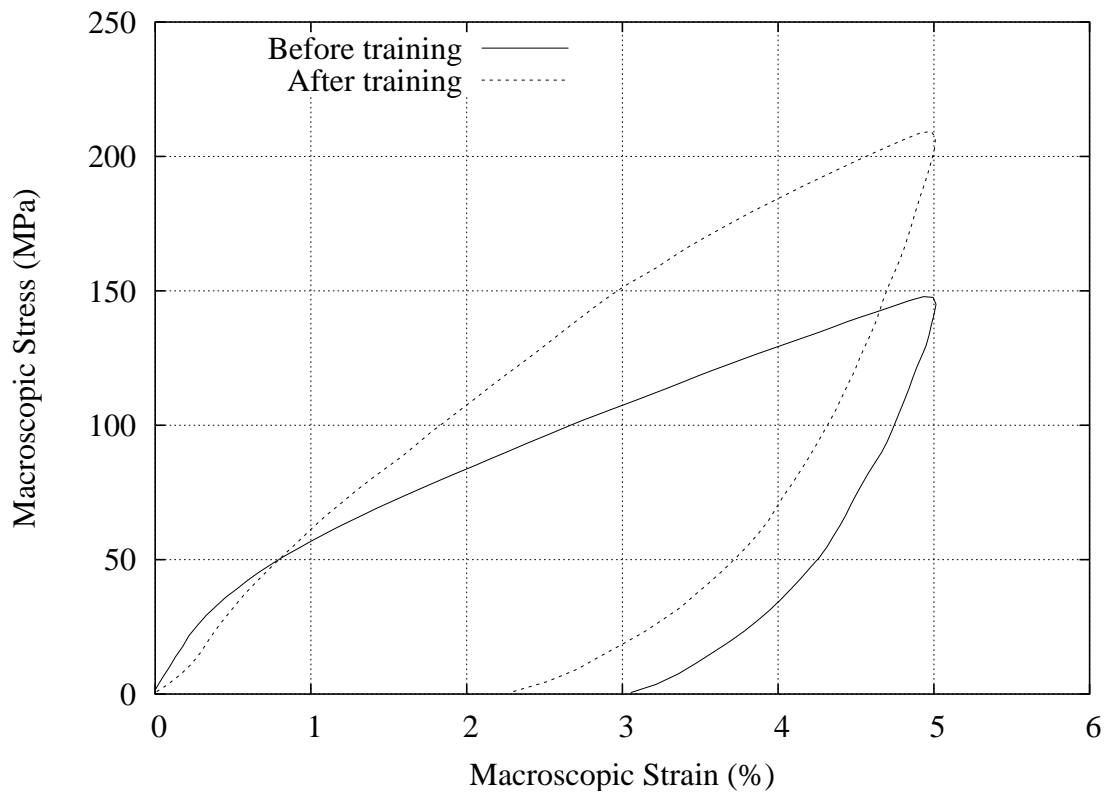
Fig. 35. Comparison of pseudoelastic behavior before and after mechanical treatment.

In addition to the increased performance of trained material, it has the benefit of reaching a steady condition after only a couple cycles. Fig. 36 shows a test in which the sample was cycled up to a constant stress value. The first cycle loads the material up to the defined stress level, in this case 195 MPa, by plastic strain and transformation. After some recovery, the next cycle loads to the same stress level and unloads along much the same path as the initial unloading. There is some additional plastic strain accumulated during this second cycle, but it is a small amount and the accumulation is minimal in the following cycles.

Further examination of strain recovery behavior was done to confirm the results from testing at varying temperatures. The stated goal of this test was to discover if the testing was causing a long term shift in the transformation temperatures, but it also exposed the cause for similarity observed in Fig. 33. To conduct this test, a fully trained sample was compressed to 5% macroscopic strain and the cooled to room temperature then placed in a furnace. The furnace was then heated from just above room temperature to 175°C, the highest temperature at which the strain sensor will function, as strain data was recorded. Fig. 37 shows the strain history as the sample was heated. The initial strain reading was adjusted to zero and recovery—expansion—shows as positive strain. As the furnace and the extensometer began to heat, there was a drift in the strain reading which showed as an initial downward slope. This has been subtracted based on baseline data in order to isolate the response of the sample from these other effects. The features of importance on this graph are the two sharp changes in slope, corresponding to the beginning and end of transformation from martensite to austenite. For the sample used in this test, the DSC reported A_s and A_f to be 86°C and 105°C respectively. The data from this strain temperature test show A_s at approximately 90°C and A_f to be near 120°C. Although the temperatures seem to have
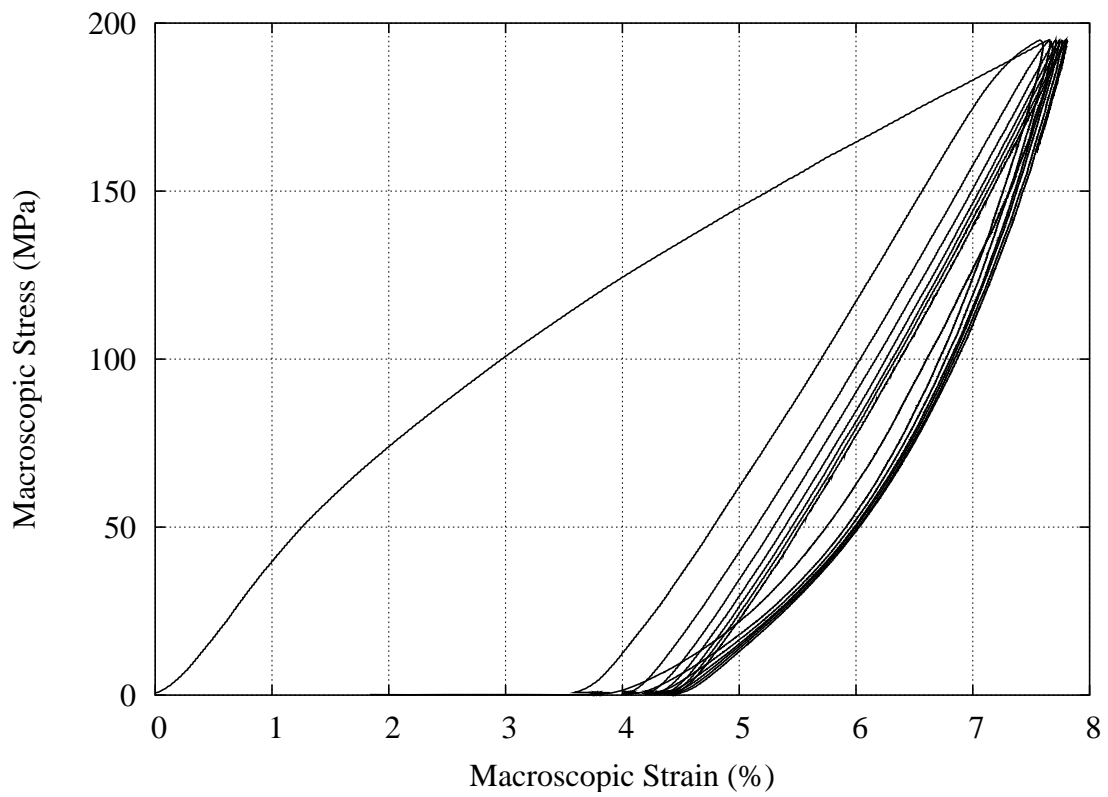
Fig. 36. Pseudoelastic stress-strain response of trained material showing stabilization after one cycle.

shifted slightly, the difference can be accounted for by considering that the heating rate of the furnace was too high to allow stabilization at each temperature. This would cause the outer sections of the cylinder to reach temperature before the inner sections, meaning that the majority of the material was cooler than the indicated temperature. This may have caused the strain readings to lag slightly behind the temperature readings. The conclusion from this test is that compression testing does not significantly permanently impact the transformation temperatures. Another important conclusion obtained through this test is related to the strain recovered upon heating. In Fig. 37, this strain is $\approx 2.2\%$, just above the level recovered on unloading during pseudoelastic testing of fully solutionized material. This means that the material, as it is currently produced, can only recover about 2.2% strain in pseudoelasticity. Any additional strain is from pore connections reopening or from edge effects. A test for this would be to develop a sample with a strong area reduction in the gage section and to fix the extensometer to that region. After testing the sample could be heated to just above A_f and the strain measured. Following this would be another heating step to $200^\circ C$ and another strain measurement. This may provide some insight into the strain behavior beyond edge effects.
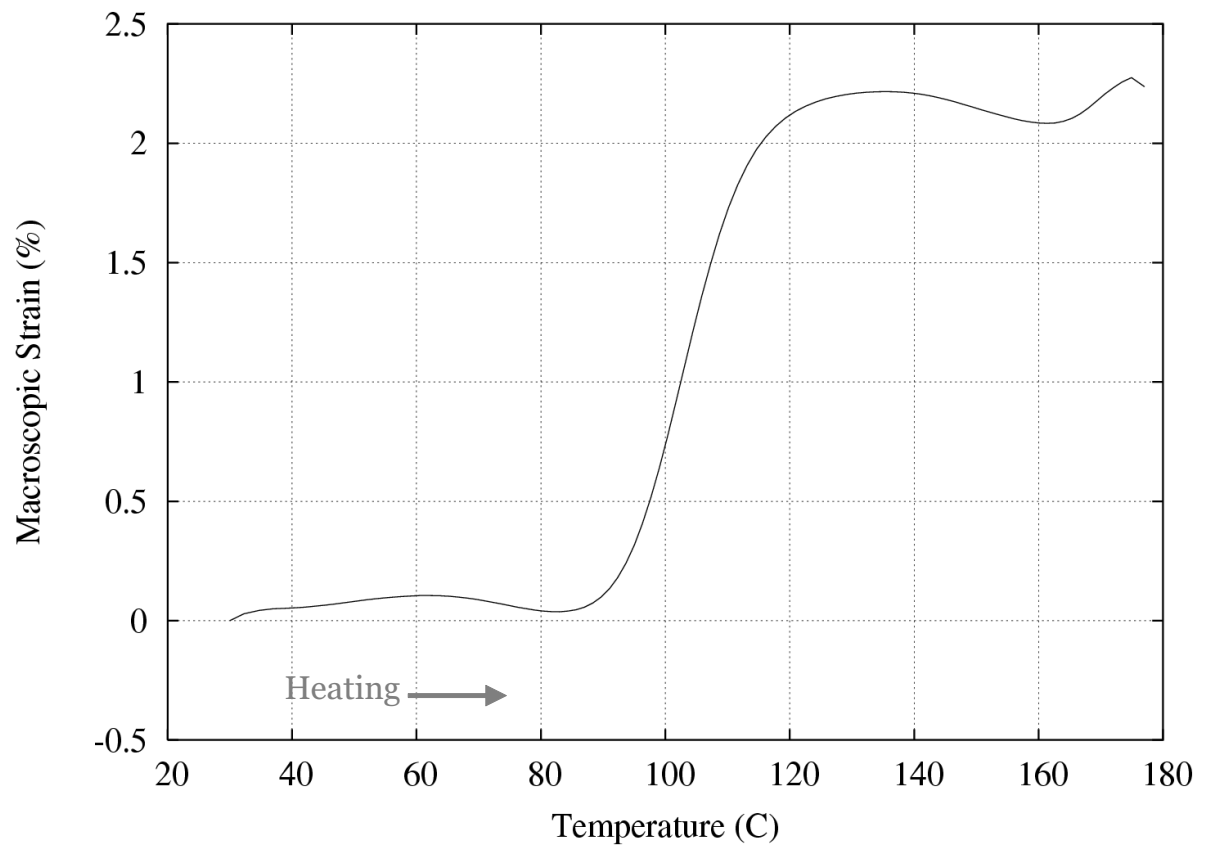
Fig. 37. Strain-temperature recorded during heating of a deformed sample.

4.   High Strain Behavior

In order for a porous SMA to be used in applications for impact and vibration absorption, they must be able to undergo large amounts of strain without catastrophic failure. To test the high strain behavior of this material, a sample was loaded in small increments up to nearly 16% strain where it began to fail. At this point the sample was unloaded and the recovery behavior was investigated. The stress-strain response from this test is shown in Fig. 38. This figure shows that the material's failure is not sudden and complete. Instead a gradual failure occurs, indicative of pore collapse and not pore-wall fracture. An examination of the pore collapse was made by cutting the sample parallel to the loading direction and examining the exposed face in the microprobe. Fig. 39 shows one view of this investigation. By comparison to microprobe images taken before testing, it can be seen that the once spherical powders have become oblong and the pores have collapsed in certain regions. This is the cause for gradual failure as shown above. It then can be concluded that this failure mode is mainly plastic deformation of the powders and the connections between powders.
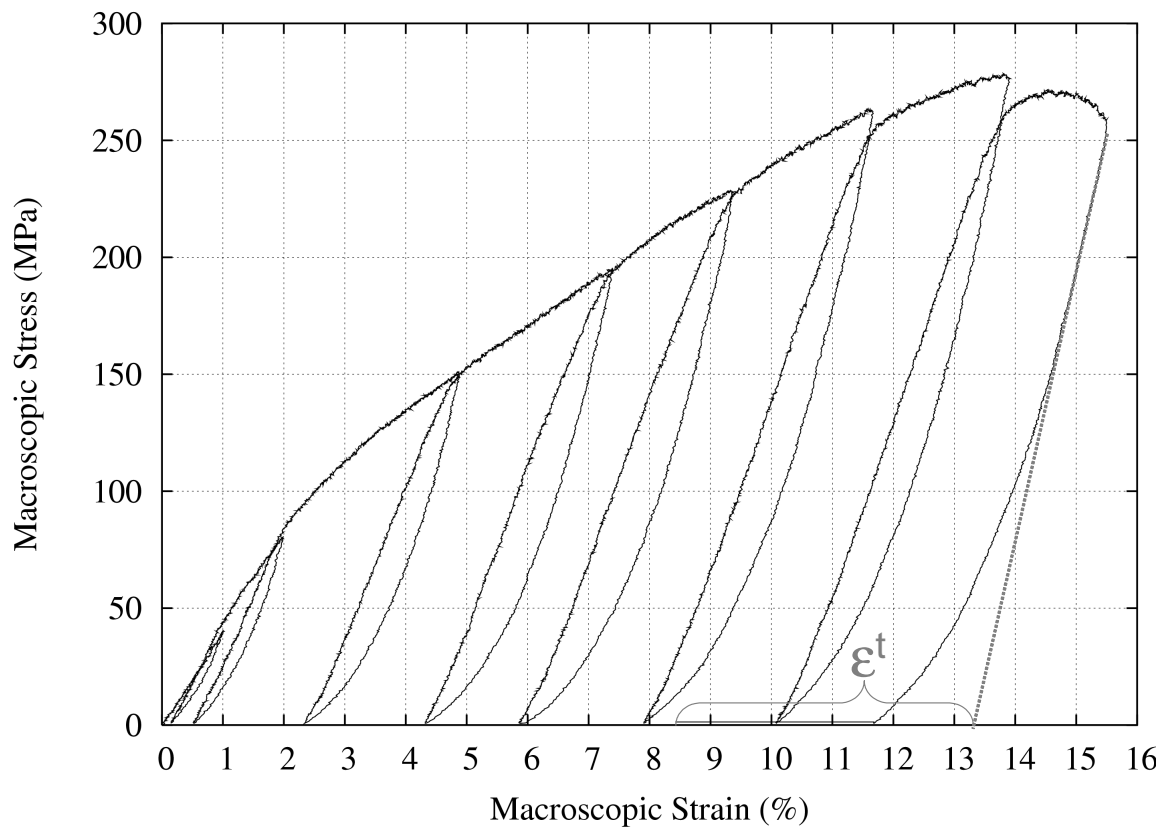
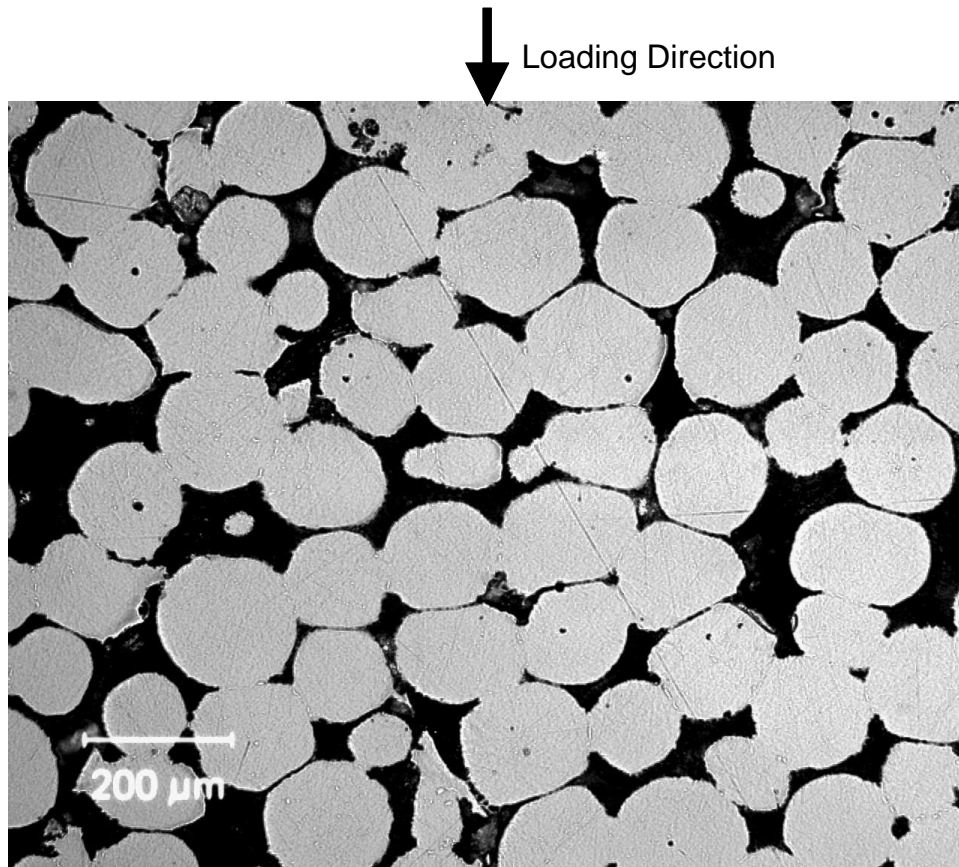Fig. 38. Stress-strain response of porous SMA loaded to high strain.

Fig. 39. Micrograph of sample after high strain testing.

5. Similar Materials Comparison

In this section, a comparison between material produced in this study and material produced through two other methods will be presented. The stress-strain curves for two similar materials will be presented and a comparison will then be made relative to the strain-recovery behavior and stiffness (corrected for porosity variations).

The first example of similar materials is a commercially made porous SMA with 60% porosity and an open pore structure identified as "Material 1" in Table VI. The austenitic finish temperature is 99°C and the martensitic finish temperature is 47°C. Combustion synthesis was used to make this material and the composition is theoretically equiatomic. Fig. 40 shows the stress-strain plot of a quasi-static loading performed at 25°C, well below A_s. Following the same procedure as for the tests described in the previous chapter, this sample was loaded incrementally to a maximum strain of 6%, which occurred at a load of approximately 57 MPa. Upon unloading from this level, 1.6% of that strain was recovered in addition to the elastic recovery. After heating at 200°C, the shape memory effect caused another 1.42% to be recovered. The total amount of strain recovered was just over 3%. Testing the same material for its pseudoelastic behavior only requires raising the temperature to a suitable level, which in this case was 107°C, several degrees above the austenitic finish temperature. In this test (Fig. 41) the larger portion of recovered strain is expected during unloading, just as in previous test of the same type. The sample was loaded incrementally to a maximum macroscopic stress of 65.83 MPa, where the macroscopic strain was measured to be 7%. On the removal of load, the sample recovered 1.7% beyond the elastic recovery. After heating, the material had recovered an additional 0.75% strain, for a total recovery of 2.43%.

Material with a similar open pore structure was fabricated from elemental powders via HIPing and is identified as "Material 2" in Table VI. Results shown here are for testing
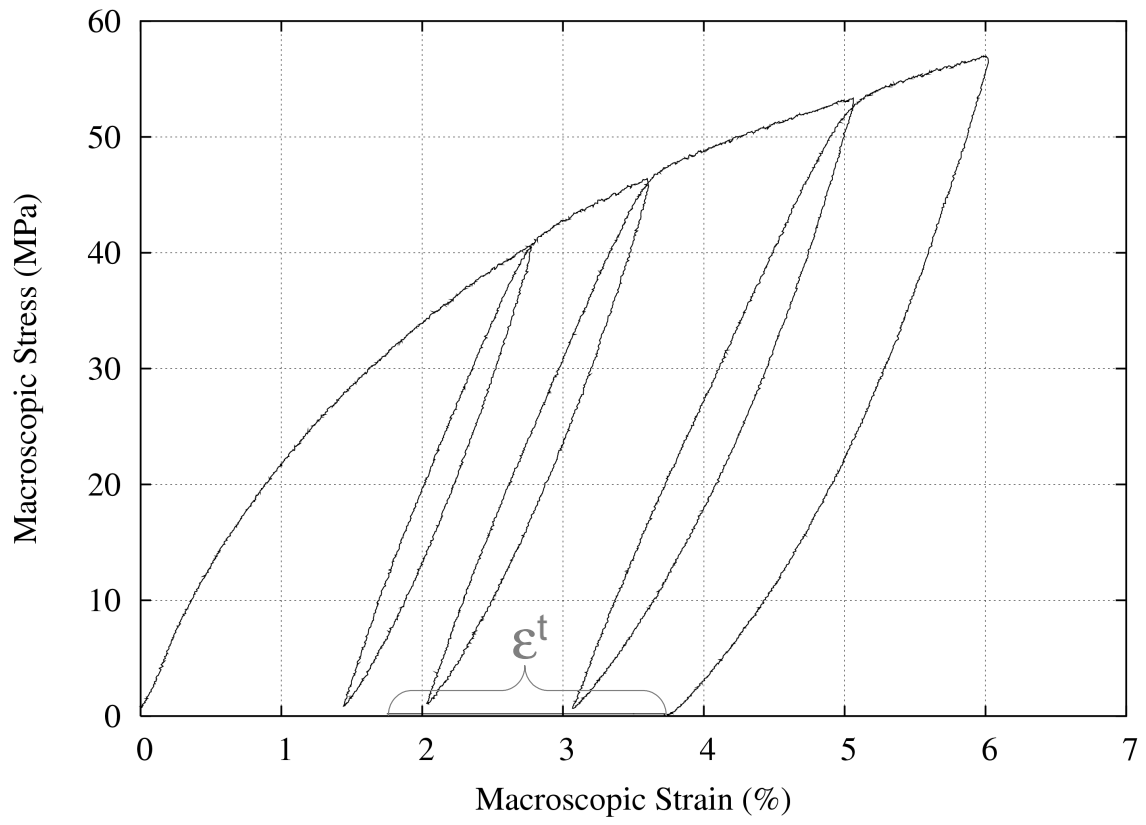
Fig. 40. Stress-strain response of SHS sample tested for SME.
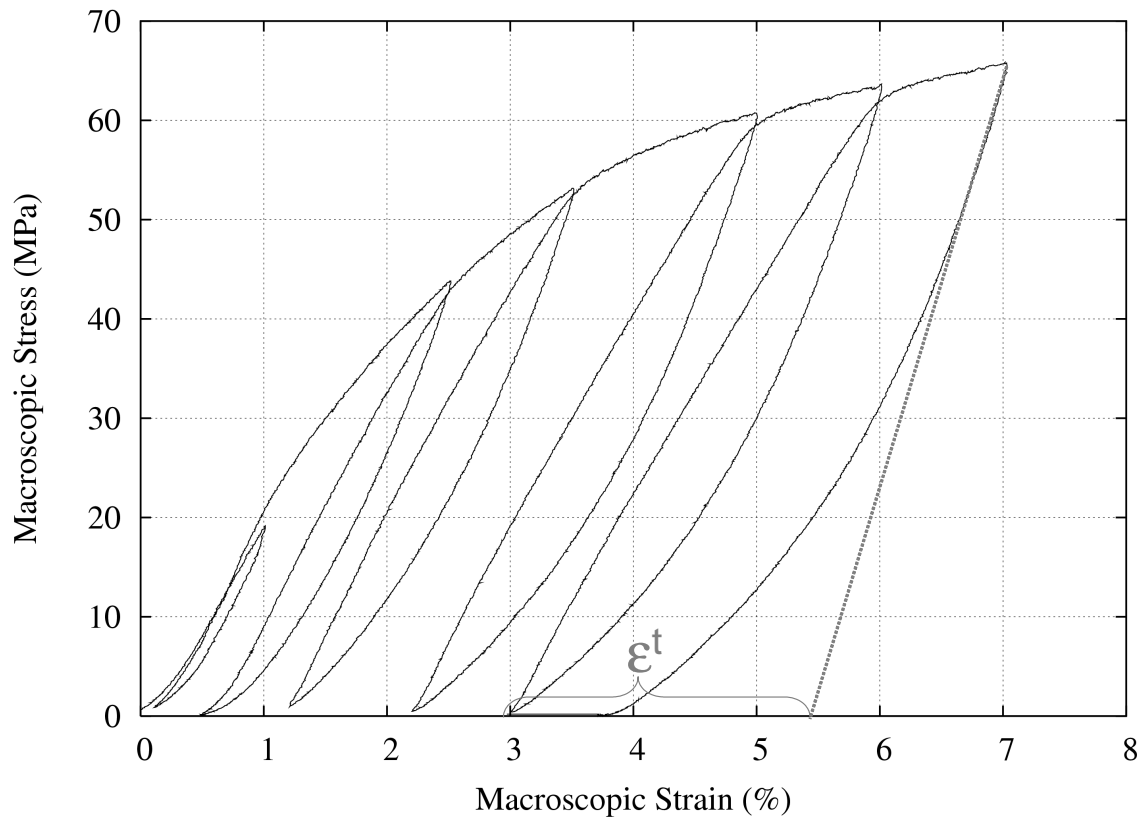
Fig. 41. Stress-strain response of SHS sample tested for pseudoelasticity.

in shape memory and pseudoelasticity for a sample having 50% porosity and M_f and A_f temperatures of -24°C and 47°C, respectively. The stress-strain response generated from testing for the shape memory effect is shown in Fig. 42. This test shows that the initial stiffness was 8 GPa and the total recovery was 3.4%. Results of testing for pseudoelasticity are presented in Fig. 43. This test showed an initial stiffness of 7 GPa and 1.5% strain recovered on unloading from 4.2% strain at 108 MPa.

Table VI is presented in order to give a clear comparison between the two materials shown above and the material from this study. In this table the strain recovery is shown as a percentage of applied strain. In addition, the stiffness of each sample has been adjusted for the porosity of that sample using the rule of mixtures. Porosity in each case was determined by density measurements. From the table it is easy to see that the shape memory performance of material produced in this study is superior to the other two materials. Pseudoelastic performance, however, is lacking. The porosity adjusted Austenitic stiffness of material from this study is higher than the other two, but still far below the "standard" stiffness of commercially available dense NiTi of 70GPa. Martensitic stiffness of all three materials is below the 30GPa of commercially available NiTi. One item of interest is the relative stiffness of the two phases. In the case of the SHS material and this study's material the Austenitic stiffness is higher than the Martensitic stiffness, as should be the case. With the small differences between these three materials, however, it is clear that the material produced here is comparable in performance to material produced by two other means.
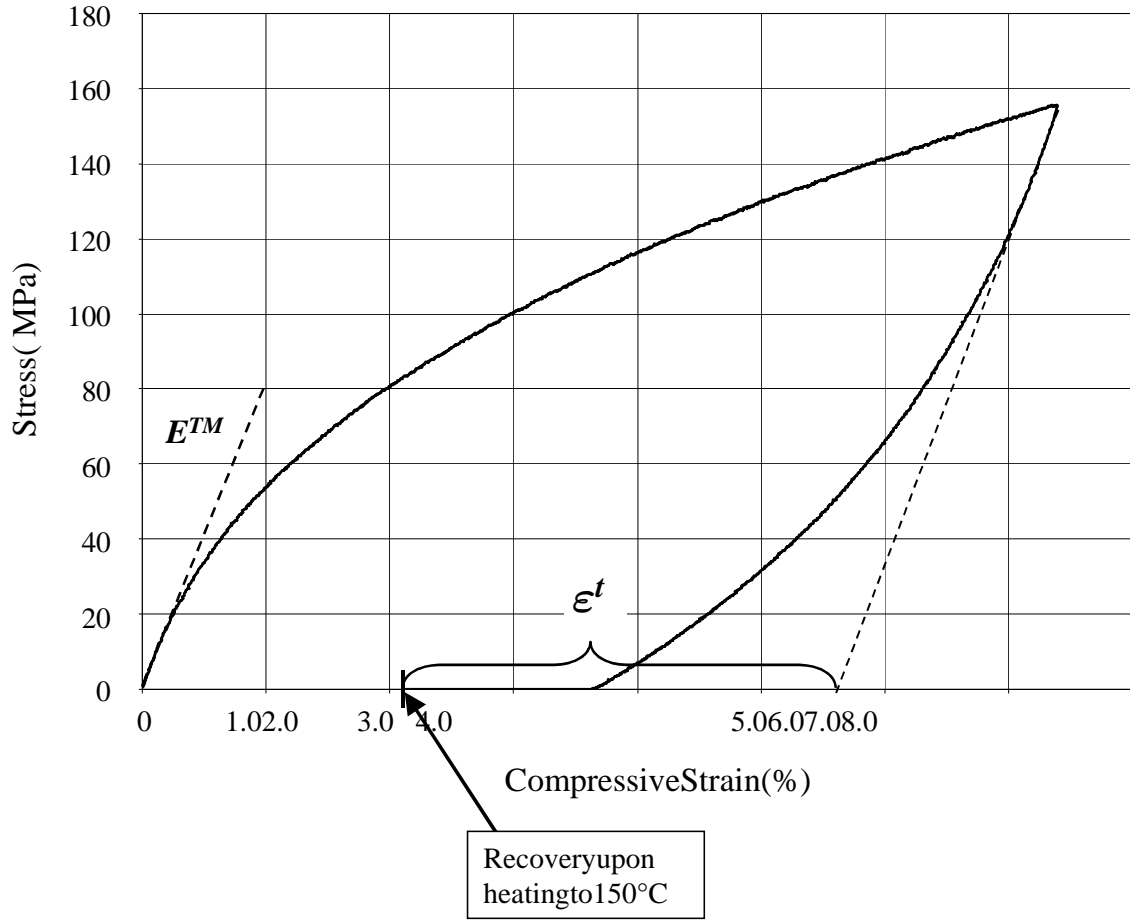
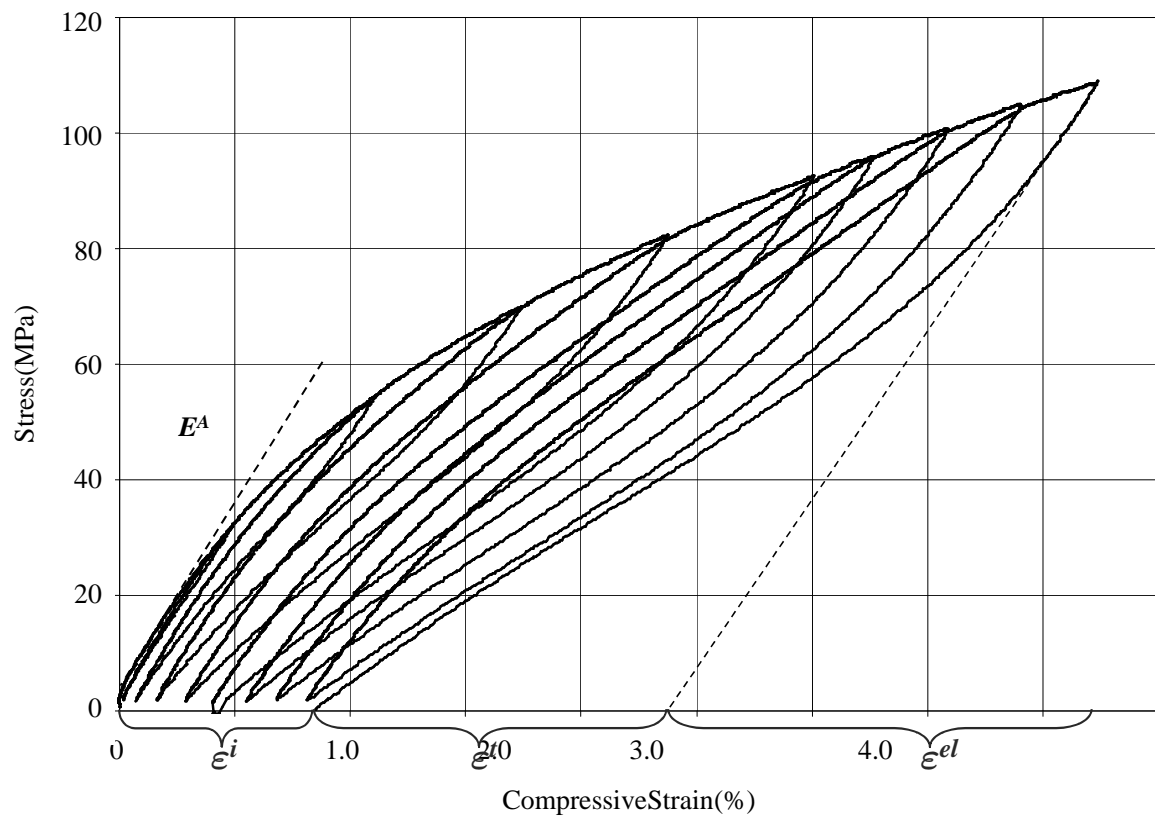Fig. 42. Stress-strain response of a 50% porous sample fabricated from elemental powders tested below A_s.

Fig. 43. Stress-strain response of a 50% porous sample fabricated from elemental powders tested above A_f.

Table VI. Comparison of similar materials.

Material (porosity)	Stiffness (GPa)		Strain Recovered/Max Strain	
	Aus.	Mar.	Shape Memory	Pseudoelasticity
Material 1 (60%)	3.3	4.5	42.8	29.2
Material 2 (50%)	14.0	16.0	45.9	35.7
Present (40%)	16.3	7.8	81.4	23.3

CHAPTER IV

CONCLUSIONS AND FUTURE WORK

A.   Summary

A method for producing porous shape memory alloys from pre-alloyed powders has been presented. This method has been shown to successfully produce porous shape memory alloy material with porosity varying from 30%–40%. A full characterization of the powders was presented including a discussion of the electrode material and its impact. The powder was analyzed in a microprobe which revealed an exaggeration of the dendritic structure common to Ti powders produced through the rotating electrode processes. Thermal analysis showed higher transformation temperatures than are expected from alloys slightly rich in nickel. After HIPing these temperatures raised slightly to 106°C, an indication of raised internal stresses caused by the mismatch between the NiTi matrix and the numerous $NiTi_2$ regions. Microprobe analysis was again used to confirm that a solution heat treatment of sufficient time would disperse the Ti-rich areas and lead to a nearly homogenous chemical composition. Transformation temperatures from solution heat treated material were observed to be similar to the as-HIPed material in most cases, but with a single sample having an A_f of 42°C.

Mechanical testing was performed to determine the performance characteristics of the porous SMA produced in this study. Material which had not been heat treated exhibited fair performance both in SME and PE, but all performance was improved by solution heat treatment. Testing for shape memory effect, for example, showed the untreated material able to recover only 53% of the originally imparted 0.0702 in/in strain. The fully solutionized material, on the other hand, recovered 81% of its 0.0608 in/in strain. Training the materials in SME improved the predicability of pseudoelastic response, but did not greatly impact the

strain recovery on unloading. Even after training to saturation below A_s, specimens tested for pseudoelastic response recovered a large portion of strain only during heating under no load. It was found that the transformation temperatures did not shift significantly during testing and that the strain recovery on unloading of trained material was the most possible from the current material.

It was found that all material can obtain large amounts of macroscopic strain before failing. When failure was reached, the collapse was gradual and characterized by pore collapse. When pore connections were broken, however, the breakage seemed to be localized rather than rapidly propagating through the sample. This is a positive aspect when considering vibration and impact isolation applications.

B.   Future Work

Based on the results of this study, future research is warranted. The obvious focus should be on the improvement of pseudoelastic performance, but investigations into other performance and fabrication aspects should be made as well.

1.   Pseudoelastic Performance

Improvement of mechanical performance is a prerequisite to any applications research. Additional thermomechanical treatments could be applied including rolling deformation or alternating heating cycles with deformation cycles. To reach increased levels of deformation needed for the purpose of marforming, the samples could be compressed within a constraining mold. This would allow the material to uniformly obtain the high levels of strain needed for the first step of the marforming process without barrelling or buckling. Beyond this, an investigation into the variants present at different stages of loadings may give insight into the reasons for incomplete transformation from martensite to austenite

during unloading. If the test specimen can be cut and examined after unloading and before heating and then again after heating, an understanding may be gained into the source of the recovered strain. Edge effects should also be considered and removed through testing of a sample with a reduced-area gage section. In situ observation as well as a measurement of M_d temperature may also provide insight into material behavior.

2.   Processing Variations

The ability of variations in the HIP recipe combined with variations in powder size to affect porosity and other characteristics should be studied. Through a study of this type, a superior combination may be discovered which yields higher porosity or better mechanical performance or both. For example, a longer hold time at temperature in the HIP may increase the strength of the connection between neighboring powders, thereby improving high stress performance.

3.   Dynamic Performance

An original area of investigation for this study, dynamic performance in both impact absorption and vibration isolation are important applications of porous SMA. Material produced in this study is especially suited for these applications as, in addition to its good mechanical performance, it is machinable and can be tapped and threaded. This was a problem with previous material as not being able to hold threads created the need for a heavy and expensive enclosure that nearly negated the benefits of using porous SMA.

REFERENCES

[1] A. Srinivasan, "Smart biological systems as models for engineered structures," *Materials Science and Engineering: C*, vol. 4, no. 1, pp. 19–26, March 1996. 1

[2] C. M. Wayman, "Phase transformations, nondiffusive," in *Physical Metallurgy*, R. W. Cahn and P. Haasen, Eds. New York: North-Holland Physics Publishing, 1983, pp. 1031–1075. 1, 2

[3] H. Funakubo, *Shape Memory Alloys*. New York: Gordon and Bleach, 1987. 1, 2

[4] C. M. Jackson, H. J. Wagner, and R. J. Wasilewski, "55-Nitinol—The alloy with a memory: Its physical metallurgy, properties and applications," NASA, Tech. Rep. NASA-SP-5110, 1972, (Personal Collection: L. E. Penrod). 1

[5] T. W. Duerig, K. N. Melton, D. Stöckel, and C. M. Wayman, Eds., *Engineering Aspects of Shape Memory Alloys*. London: Butterworth-Heinemann, 1990. 1

[6] J. V. Humbeeck, "Non-medical applications of shape memory alloys," *Materials Science and Engineering: A*, vol. 273-275, pp. 134–148, 1999. 2

[7] T. Duerig, A. Pelton, and D. Stockel, "An overview of Nitinol medical applications," *Materials Science and Engineering: A*, vol. 273–275, pp. 149–160, 1999. 2

[8] J. Haasters, G. Bensmann, and A. Pon, "Applications of the memory alloy NiTi as an implant material," *Mater. Sci. Implant Orthop. Surg*, vol. 116, pp. 117–124, 1986. 2

[9] M. Thier, "Shape-memory alloys for implants, instruments, and external applications in medicine; uses and chances in the future," *Metall. (Berlin)*, vol. 44, no. 1, pp. 29–33, 1990. 2

[10] S. Miyazaki, "Medical and dental applications of shape memory alloys," in *Shape Memory Alloys*, K. Otsuka and C. M. Wayman, Eds. Cambridge: Cambridge University Press, 1999, ch. 12, pp. 267–281. 2

[11] L. J. Garner, L. N. Wilson, and D. C. Lagoudas, "Development of a shape memory alloy actuated biomimetic vehicle," *Smart Structures and Materials*, vol. 9, no. 5, pp. 673–683, October 2000. 2

[12] O. K. Rediniotis, D. C. Lagoudas, L. Garner, and N. Wilson, "Experiments and analysis of an active hydrofoil with sma actuators," in *Proc. 36th AIAA Aerospace Sciences Meeting*, Reno, NV, 1998. 2

[13] A. P. Jardine, J. M. Kudva, C. Martin, and K. Appa, "Shape memory alloy Ti-Ni actuators for twist control of smart wing designs," in *Proc. SPIE Mathematics and Controls in Smart Structures*, vol. 2717, 1996, pp. 160–165. 2

[14] A. Baz, K. Iman, and J. McCoy, "Active vibration control of flexible beams using shape memory actuators," *J. Sound Vib.*, vol. 140, pp. 437–456, 1990. 2

[15] Y. C. Yiu and M. E. Regelbrugge, "Shape-memory alloy isolators for vibration suppression in space applications," in *Proc. 36th AIAA/ASME/ASCE/AHS/ASC Structures, Structural Dynamics, and Materials Conference*, New Orleans, LA, April 1995, pp. 3390–3398. 2

[16] R. Fosdick and Y. Ketema, "Shape memory alloys for passive vibration damping," *Journal of Intelligent Material Systems and Structures*, vol. 9, pp. 854–870, 1998. 2, 13

[17] A. Andersen, D. Pedersen, A. Sivertsen, and S. Sangesland, "Detailed study of shape memory alloys in oil well applications," SINTEF Petroleum Research, Trondheim,

Norway, Tech. Rep. 32.0924.00/01/99, July 1999. 2

[18] T. W. Duerig and A. R. Pelton, "Ti-Ni shape memory alloys," in *Materials Properties Handbook: Titanium Alloys*, G. W. R. Boyer and E. W. Collings, Eds. Materials Park, OH: American Society for Metals, 1994, pp. 1035–1048. 2, 9

[19] C. Wayman and T. Duerig, *Engineering Aspects of Shape Memory Alloys*. London: Butterworth-Heinemann Ltd., 1990, ch. Introduction to Martensite and Shape Memory, pp. 3–17. 2, 9

[20] L. C. Chang and T. A. Read, "Plastic deformation and diffusionless phase changes in metals – the gold–cadmium beta phase," *Trans. AIME*, vol. 191, pp. 47–52, 1951. 5

[21] W. J. Buehler, J. V. Gilfrich, and R. C. Wiley, "Effects of low-temperature phase changes on the mechanical properties of alloys near composition TiNi," *J. Appl. Phys.*, vol. 34, pp. 1475–1477, 1963. 5

[22] R. Batist, "Mechanical energy dissipation related with martensitic transformation processes," in *Proc. ASTM STP, Mechanics and Mechanisms of Material Damping*, V. K. Kinra and A. Wolfenden, Eds., no. 1169. Philadelphia, PA: American Society for Testing and Materials, 1992, pp. 45–59. 5

[23] K. Madangopal, "The self accomodating martensitic microstructure of Ni-Ti shape memory alloys," *Acta Metall.*, vol. 45, no. 12, pp. 5347–5365, 1997. 7

[24] D. E. Hodgson and J. W. Brown, *Using Nitinol Alloys*. San Jose, CA: Shape Memory Applications, Inc., 2000. 7, 9, 11

[25] Y. Liu and S. P. Galvin, "Criteria for pseudoelasticity in near-equiatomic NiTi shape memory alloys," *Acta Mater.*, vol. 45, no. 11, pp. 4431–4439, 1997. 9, 42, 65

[26] H. Sehitoglu, I. Karaman, R. Anderson, X. Zhang, K. Gall, H. Maier, and Y. Chumlyakov, "Compressive response of NiTi single crystals," *Acta Mater.*, vol. 48, pp. 3311–3326, 2000. 9

[27] K. Gall, H. Sehitoglu, R. Anderson, I. Karaman, Y. Chumlyakov, and V. Kireeva, "On the mechanical behavior of single crystal NiTi shape memory alloys and related polycrystalline phenomenon," *Materials Science and Engineering: A*, vol. 317, pp. 85–92, 2001. 9

[28] W. Chen, Q. Wu, J. Kang, and N. Winfree, "Compressive superelastic behavior of a NiTi shape memory alloy as strain rates of $0.001 - 750s^{-1}$," *International Journal of Solids and Structures*, vol. 38, pp. 8989–8998, 2001. 9

[29] K. N. Melton, "Ni-Ti based shape memory alloys," in *Engineering Aspects of Shape Memory Alloys*, T. W. Duerig, K. N. Melton, D. Stökel, and C. M. Wayman, Eds. London: Butterworth-Heinemann, 1990, pp. 21–35. 11

[30] E. Hornbogen, "Hundred years of precipitation hardening," *Journal of Light Metals*, vol. 1, no. 2, pp. 127–132, 2001. 11

[31] C. Somsen, H. Zähres, J. Kästner, E. F. Wassermann, T. Kakeshita, and T. Saburi, "Influence of thermal annealing on the martensitic transitions in Ni-Ti shape memory alloys," *Materials Science and Engineering: A*, vol. 273–275, pp. 310–314, 1999. 11

[32] H. F. Lopez and A. Salinas Rodriquez, "Aging effects on transformation temperatures of cold-worked Ni-52at.%Ti shape memory alloy," *Materials Science and Technology*, vol. 18, pp. 268–272, March 2002. 12

[33] Y. Liu, "Mechanical stabilisation of martensite due to cold deformation," *Materials Science and Engineering: A*, vol. 273–275, pp. 668–672, 1999. 12

[34] Y. Liu and D. Favier, "Stabilisation of martensite due to shear deformation via variant reorientation in polycrystalline NiTi," *Acta Mater.*, vol. 48, pp. 3489–3499, 2000. 12

[35] Y. Liu and G. S. Tan, "Effect of deformation by stress-induced martensitic transformation on the transformation behaviour of NiTi," *Intermetallics*, vol. 8, pp. 67–75, 2000. 12

[36] J. Speilfeld, "Marforming and martempering of a Cu-Zn-Al shape memory alloy," *Materials Science and Engineering: A*, vol. 273-275, pp. 639–643, 1999. 12

[37] D. Wurzel, "Marforming and tempering of binary Ni–Ti alloys including precipitation effects," *Material Science and Engineering: A*, no. 273–275, pp. 634–638, 1999. 12

[38] Y. Liu, Y. Liu, and J. Van Humbeeck, "Two-way shape memory effect developed by martensite deformation in Ni-Ti," *Acta Mater.*, vol. 47, no. 1, pp. 199–209, 1999. 12

[39] D. Treppmann, E. Hornbogen, and D. Wurzel, "Thermomechanical treatment of shape memory alloys by ausforming and marforming," *Z. Metallkd.*, vol. 89, no. 2, pp. 126–134, 1982. 12

[40] I. Martynova, V. Skorohod, S. Solonin, and S. Goncharuk, "Shape memory and superelasticity behaviour of porous Ti-Ni material," *Journal de Physique*, vol. 1, no. C4, pp. 421–426, 1991. 12

[41] B. Y. Li, L. J. Rong, and Y. Y. Li, "Porous NiTi alloy prepared from elemental powder sintering," *J. Mater. Res.*, vol. 13, pp. 2847–2851, 1998. 12, 14

[42] M. D. McNeese, D. C. Lagoudas, and T. C. Pollock, "Processing of TiNi from elemental powders by hot isostatic pressing," *Material Science and Engineering: A*, vol. 280, pp. 334–348, 2000. 12, 15, 28

[43] Y. Li, L. Rong, and Y. Li, "Pore characteristics of porous NiTi alloy fabricated by combustion synthesis," *Journal of Alloys and Compounds*, vol. 325, pp. 259–262, 2001. 12, 13

[44] A. Kapanen, J. Ryhanen, A. Davilov, and J. Tuukkanen, "Effect of nickel–titanium shape memory metal alloy on bone formation," *Biomaterials*, vol. 22, pp. 2475–2480, 2001. 12

[45] R. A. Ayers, S. J. Simske, T. A. Bateman, A. Petkus, R. L. C. Sachdeva, and V. E. Gyunter, "Effects of Nitinol implant porosity on cranial bone ingrowth and apposition after 6 weeks," *J. Biomed. Mater. Res.*, vol. 45, no. 1, pp. 42–47, 1999. 13

[46] S. Simske, R. A. Ayers, and T. A. Bateman, "Porous materials for bone engineering," in *Porous Materials for Tissue Engineering*, ser. Materials Science Forum, D. Liu and V. Dixit, Eds.   Enfield, NH: Transtech, 1997, vol. 250, pp. 151–182. 13

[47] P. Thomson, G. J. Balas, and P. H. Leo, "The use of shape memory alloys for passive structural damping," *Smart Materials and Structures*, vol. 4, no. 1, pp. 36–41, March 1995. 13

[48] R. DesRoches and M. Delemont, "Seismic retrofit of simply supported bridges using shape memory alloys," *Engr. Struct.*, vol. 24, pp. 325–332, 2002. 13

[49] K. Wilde, P. Gardoni, and Y. Fujino, "Base isolation system with shape memory alloy device for elevated highway bridges," *Engr. Struct.*, vol. 22, pp. 222–229, 2000. 13

[50] C. M. Friend and C. R. D. Mattey, "Active strain-energy tuning of low actuator-fraction shape-memory alloy (SMA) hybrid composites," *Material Science and Engineering: A*, vol. 273–275, pp. 799–803, 1999. 13

[51] T. L. Turner, "Dynamic response tuning of composite beams by embedded shape memory alloy actuators," in *Proc. SPIE Smart Structures and Materials 2000: Industrial and Commercial Applications of Smart Structures Technologies*, J. H. Jacobs, Ed., vol. 3991, Newport Beach, CA, 2000, pp. 377–388. 13

[52] D. Lagoudas, M. Khan, J. Mayes, and B. Henderson, "Parametric study and experimental correlation of an SMA based damping and passive vibration device," in *Proc. IMECE '02*, New Orleans, LA, 2002. 13

[53] N. G. Davies and S. Zhen, "Review metallic foams: Their production, properties and applications," *Journal of Material Science*, vol. 18, pp. 1899–1911, 1983. 13

[54] M. Bram, A. Ahmad-Khanlou, A. Heckmann, B. Fuchs, H. P. Buchkremer, and D. Stover, "Powder metallurgical fabrication precessed for NiTi shape memory alloy parts," *Material Science and Engineering: A*, vol. 00, pp. 1–10, 2002, in press. 13

[55] L. Ye, Z. Liu, K. Raviprasad, M. Quan, M. Umemoto, and Z. Hu, "Consolidation of MA amorphous NiTi powders by spark plasma sintering," *Material Science and Engineering: A*, vol. 241, pp. 290–293, 1998. 13

[56] H. C. Yi and J. J. Moore, "The combustion synthesis of Ni-Ti shape memory alloys," *Journal of Metals*, vol. 42, pp. 31–35, 1990. 13

[57] Y. Li, L. Rong, and Y. Li, "Compressive property of porous NiTi alloy synthesized by combustion synthesis," *Journal of Alloys and Compounds*, vol. 345, pp. 271–274, 2002. 13

[58] B. Li, L. Rong, Y. Li, and V. Gjunter, "A recent development in producing porous Ni–Ti shape memory alloys," *Intermetallics*, vol. 8, pp. 881–884, 2000. 14

[59] M. Zhu, T. C. Li, J. T. Liu, and D. Z. Yang, "Microstructure characteristics of NiTi shape memory alloy obtained by explosive compact of elemental nickel and titanium powders," *Acta Metall. Mater.*, vol. 39, no. 7, pp. 1481–1487, 1991. 14

[60] Y. L. Zhu, T. C. Li, J. T. Liu, X. D. Han, and D. Z. Yang, "Shock synthesis of NiTi intermetallic compounds from a mixture of titanium and nickel elemental powders," *Scripta Metallurgica et Materialia*, vol. 30, no. 6, pp. 775–780, 1994. 14

[61] J. C. Hey and A. P. Jardine, "Shape memory TiNi synthesis from elemental powders," *Material Science and Engineering: A*, vol. 188, no. 1-2, pp. 291–300, 1994. 14

[62] T. C. Li, Y. B. Qui, and J. T. Liu, "Explosive consolidation of titanium-nickel shape-memory alloy from pure titanium powder and pure nickel powder," *J. of Materials Science Letters*, vol. 11, pp. 845–847, 1992. 14

[63] K. Tangaraj, Y.-C. Chen, and K. Salama, "Fabrication of porous NiTi shape memory alloy by elemental powder sintering," in *Proc. ASME International Mechanical Engineering Congress & Exposition*, J. Redmont and J. Main, Eds., Orlando, FL, 2000, pp. 59–63. 14

[64] B. Li, L. Rong, and Y. Li, "The influence of addition of TiH_2 in elemental powder sintering porous Ni–Ti alloys," *Materials Science and Engineering: A*, vol. 281, pp. 169–175, 2000. 14

[65] M. W. Kearns, P. A. Blenkinsop, and A. C. Barber, "Manufacture of a novel porous metal," *Int. J. of Powder Metallurgy*, vol. 24, no. 1, pp. 59–64, 1988. 15

[66] D. S. Schwartz, D. S. Shih, R. J. Lederich, R. L. Martin, and D. A. Deuser, "Development and scale-up of the low density core process for Ti-64," in *Proc. Materials Research Society Symposium*, vol. 521, San Francisco, CA, 1998, pp. 225–230. 15

[67] N. G. Davis, J. Teisen, C. Schuh, and D. C. Dunand, "Solid-state foaming of titanium by superplastic expansion of argon-filled pores," *Journal of Materials Research*, vol. 16, no. 5, pp. 1508–1519, May 2001. 15

[68] H. Kato, T. Koyari, M. Tokizane, and S. Miura, "Stress-strain behavior and shape memory effect in powder metallurgy TiNi alloys," *Acta Metall. Mater.*, vol. 42, no. 4, pp. 1351–1358, 1993. 17, 18

[69] C. Klein and M. Costa, "DNA methylation, heterochromatin and epigenetic carcinogens," *Mutation Research/Reviews in Mutation Research*, vol. 386, no. 2, pp. 163–180, April 1997. 17

[70] M. Tokizane, T. Fukami, and T. Inaba, "Structure and mechanical properties of the hot pressed compact of Ti-rich TiAl powder produced by the plasma rotating electrode process," *ISIJ International*, vol. 31, no. 10, pp. 1088–1092, 1991. 20

[71] L. Apgar and D. Eylon, "Microstructure control of titanium aluminae powder compacts by thermomechanical processing," *ISIJ International*, vol. 31, no. 8, pp. 915–921, 1991. 20

[72] E. C. Vandygriff, D. C. Lagoudas, K. Thangaraj, and Y. C. Chen, "Porous shape memory alloys, Part I: Fabrication and characterization," in *Proc. ASC 15th Annual Technical Conference*, College Station, TX, 2000, pp. 239–247. 25, 28

[73] B. Strnadel, S. Ohashi, H. Ohtsuka, S. Miyazaki, and T. Ishihara, "Effect of mechanical cycling on the pseudoelasticity characteristics of Ti-Ni and Ti-Ni-Cu alloys," *Material Science and Engineering: A*, vol. 203, pp. 187–196, 1995. 42, 65

[74] D. A. Hebda and S. R. White, "Effect of training conditions and extended thermal cycling on nitinol two-way shape memory behavior," *Smart Materials and Structures*,

vol. 4, no. 4, pp. 298–304, 1995. 67

APPENDIX A

DATA FROM HIP RUNS

This appendix contains data from four HIP runs, presented chronologically. All the actual data matches the programmed data very closely, but in some cases the initial pressure drop on unloading is much quicker than desired. This is due to the method of pressure release. In this machine, the pressure is released through a manually adjustable vent which is opened and closed by the controller. Rapid pressure drops occur when this vent is open too far when the venting step is reached.

The first cycle (Fig. A-1), had fewer steps than the final cycle presented in chapter II and was run as a initial trial in a group to determine the best temperature for consolidation of pre-alloyed powder. The hold at 700°C for a half hour was used to ensure all seals had expanded before the pressure was raised and the hold temperature of $900^{\circ}C$ was chosen based on previous work with elemental powders. Powders processed with this method were barely combined and could be broken free with little pressure. After this, the temperature was raised slightly to 950°C while all other parameters were kept the same as the previous run (see Fig. A-2. Some consolidation was seen, but it was still very weak. Again raising the temperature slightly, this time to 1000°C, improved the result. Fig. A-3 shows the data from this run. The sample produced from this method was very strongly combined compared to previous samples, but still very brittle. The cycle shown in Fig. A-4 was the first to produce good samples which were in a single piece and were not brittle. The porosity of these samples was ~35%. The final cycle, presented in Chapter II, is presented again here for continuity (Fig. A-5).
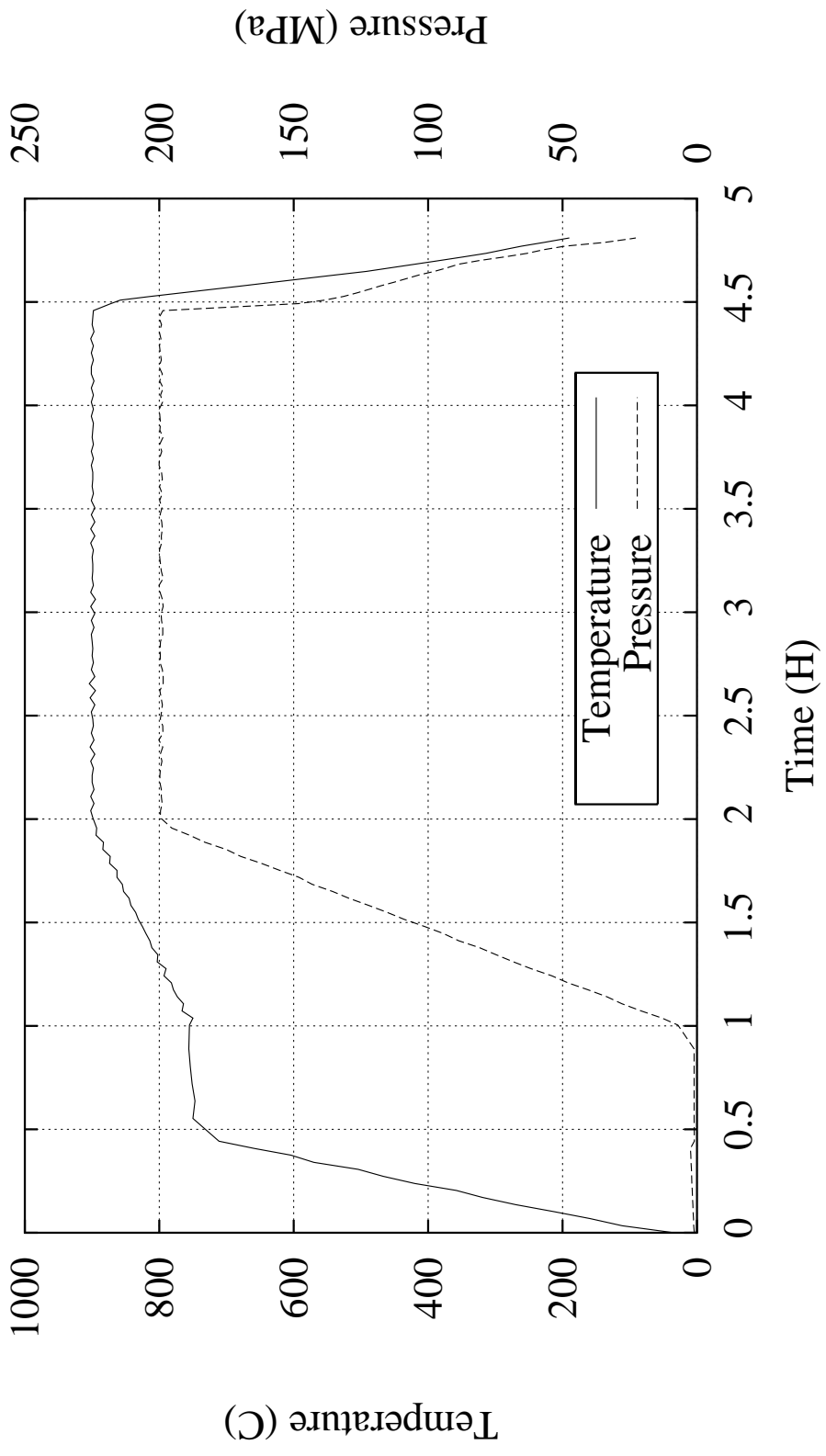
Fig. A-1. HIP run with soak temperature of 900°C.
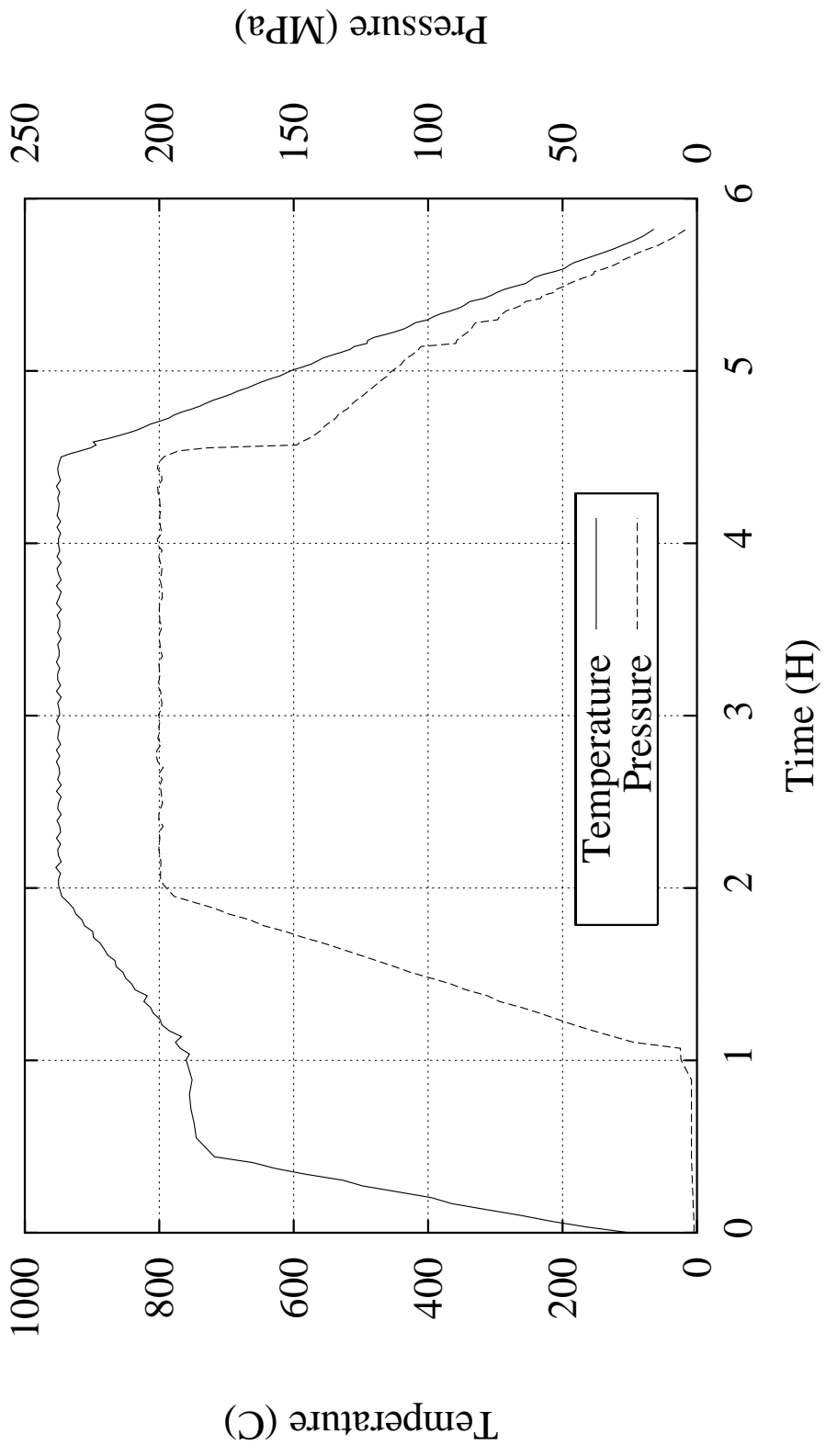
Fig. A-2. HIP run with soak temperature of 950°C.
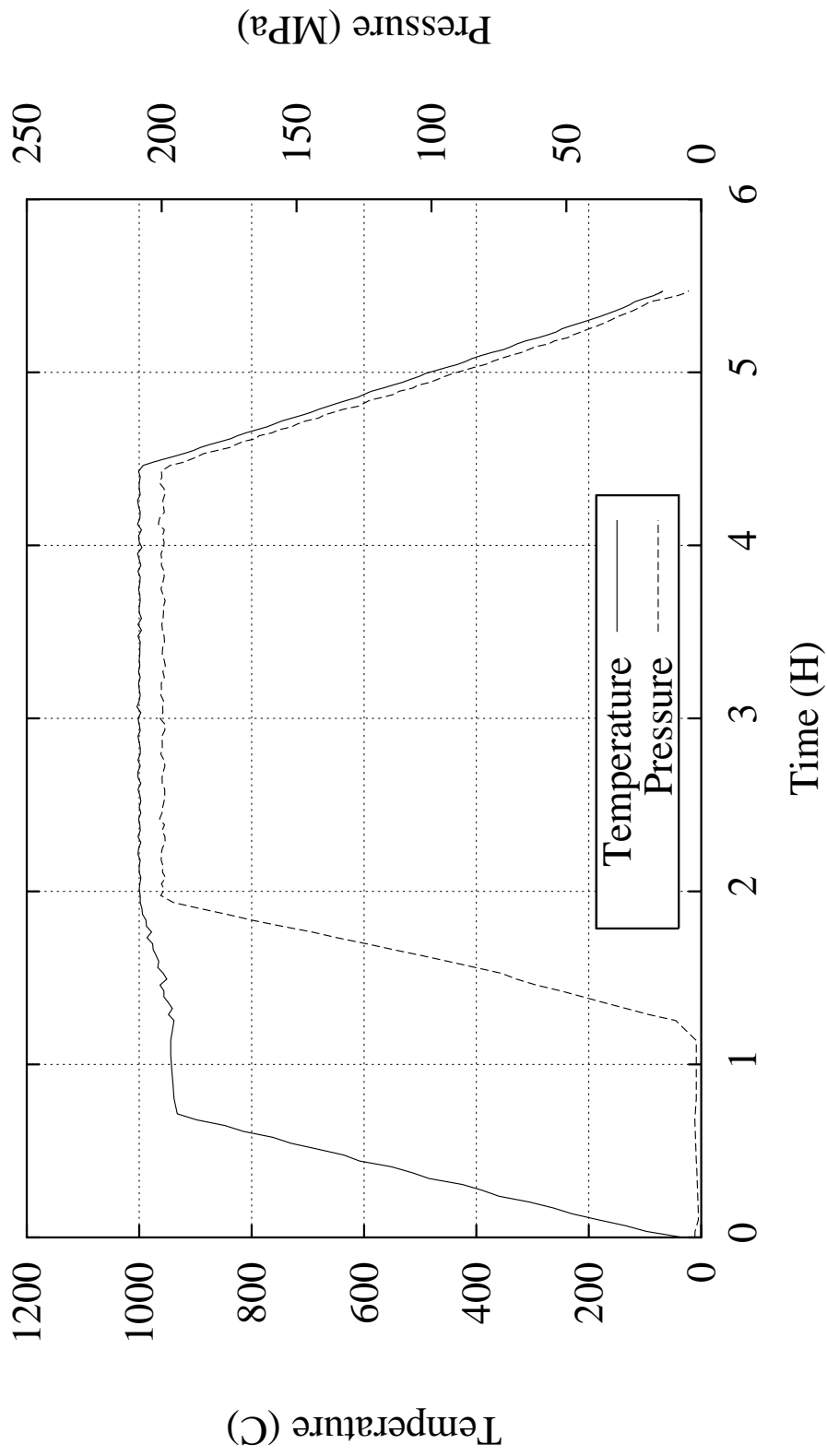
Fig. A-3. HIP run with soak temperature of 1000°C.
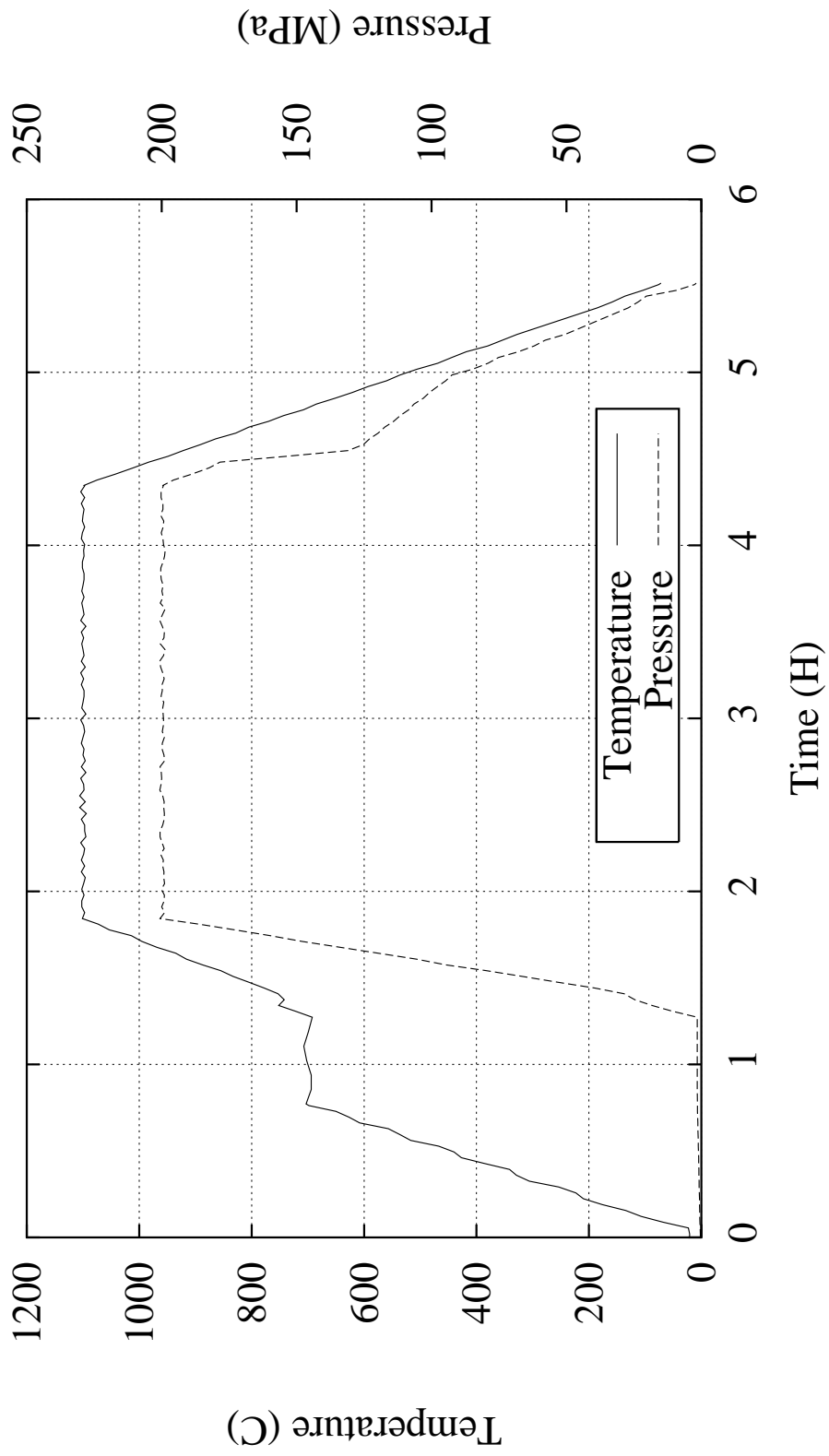
Fig. A-4. HIP run with soak temperature of 1100°C.
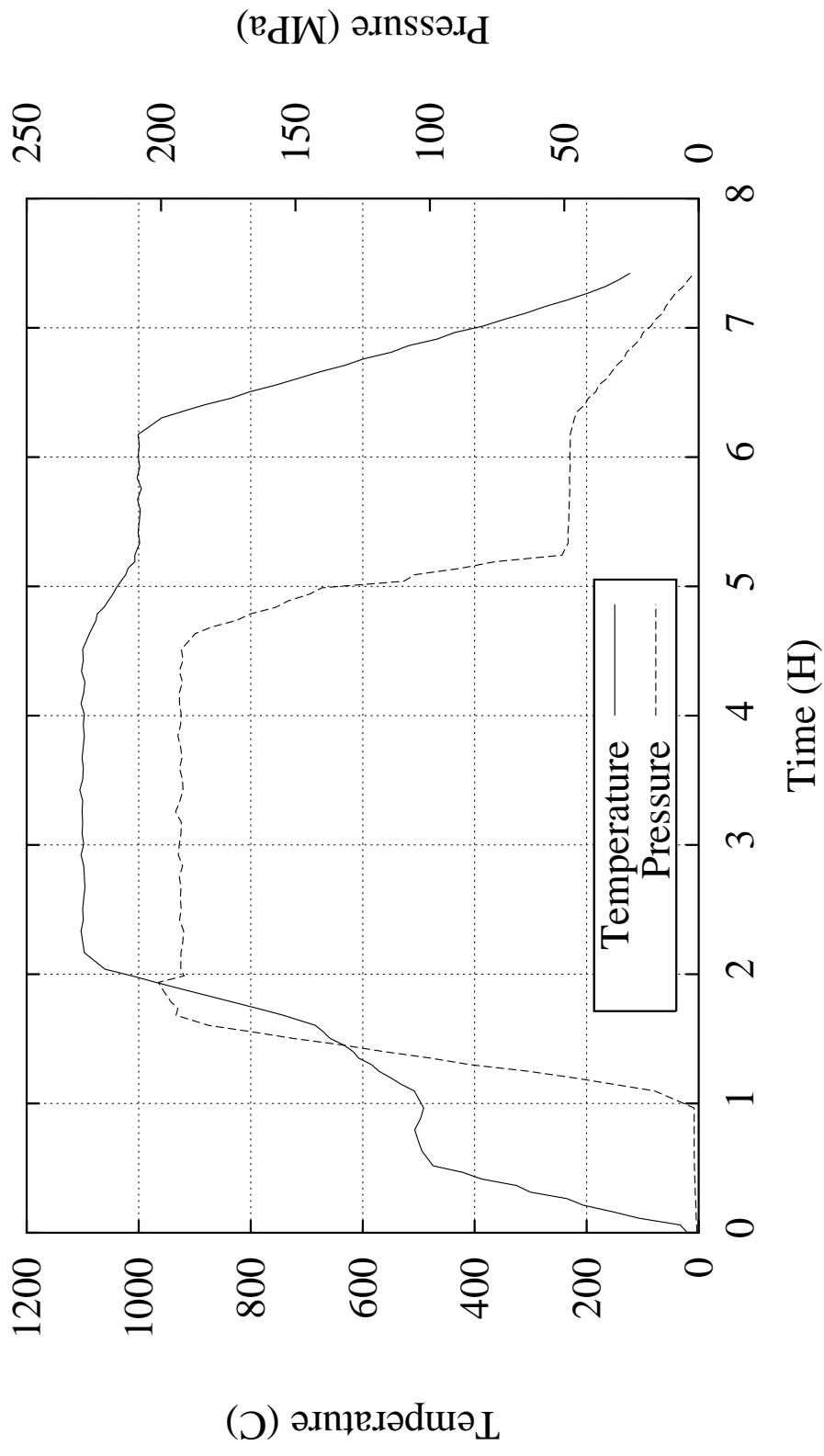
Fig. A-5. Final HIP run with soak temperature of 1100°C and additional low pressure/high temperature step.

APPENDIX B

ADDITIONAL DSC DATA

This appendix presents DSC data from samples which were not presented in the main chapters. The first three figures are from as-HIPed sample(Figs. B-1–B-3). The following three figures are from samples after a long solution heat treatment (Figs. B-4–B-6). The last figure in this group is the anomalous result mentioned in Chapter III.
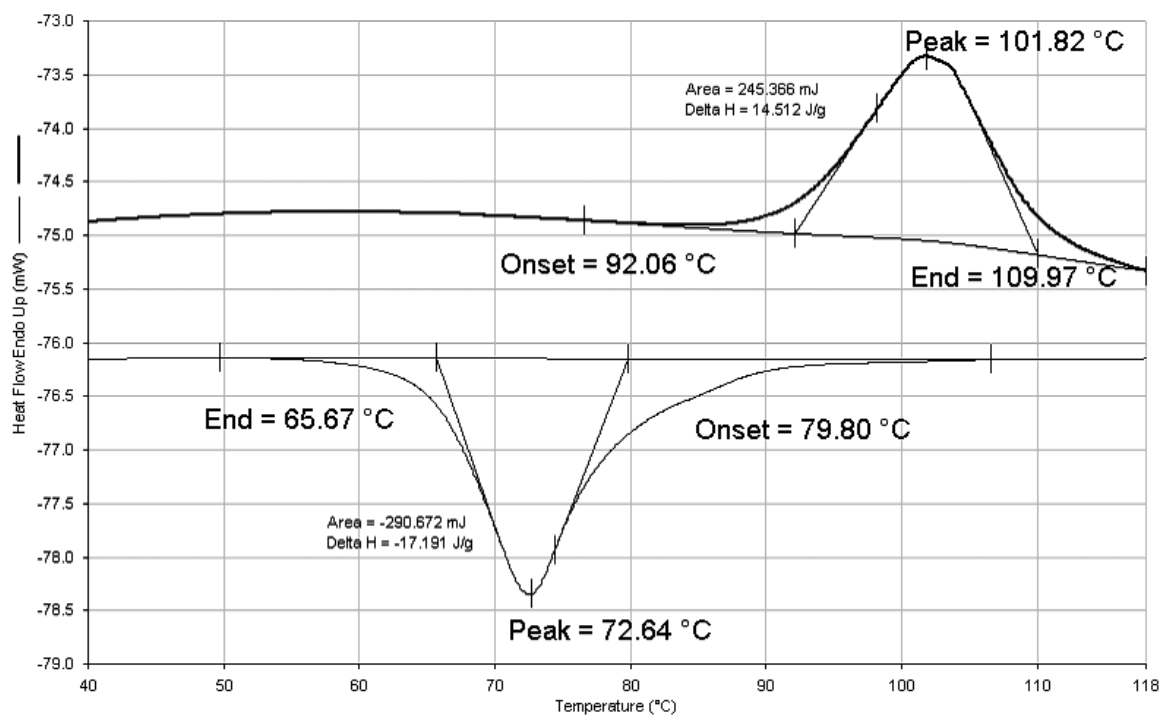
Fig. B-1. DSC results from as-HIPed sample.
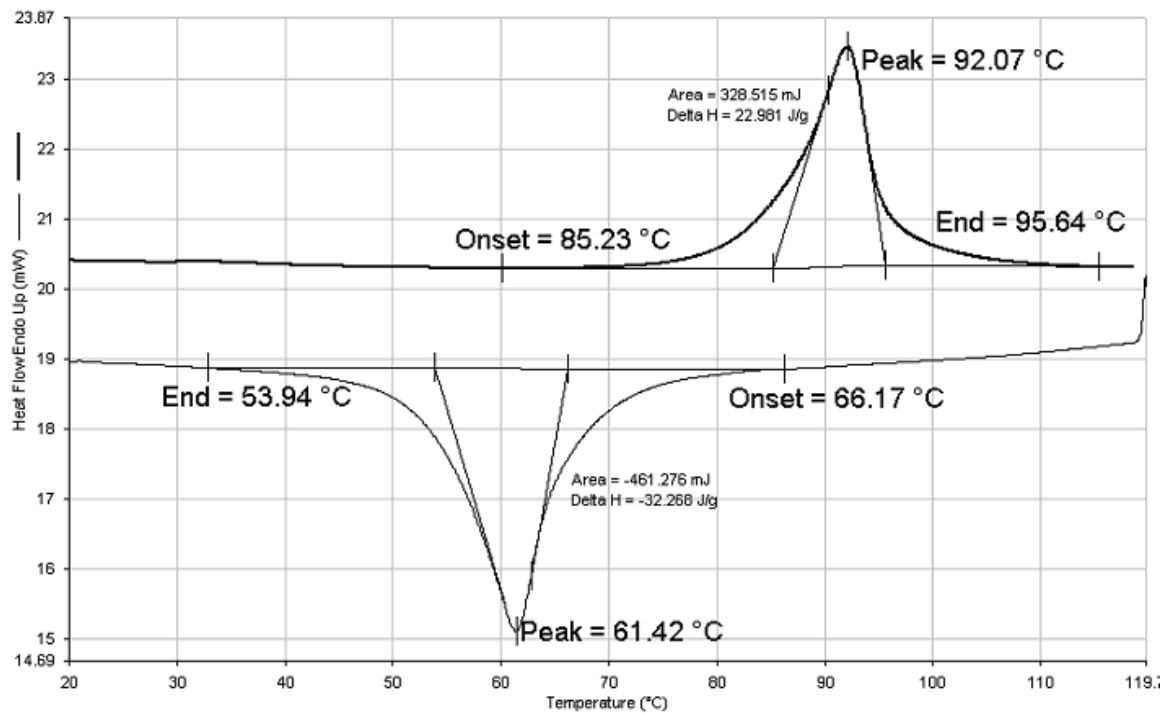
Fig. B-2. DSC results from as-HIPed sample(2).
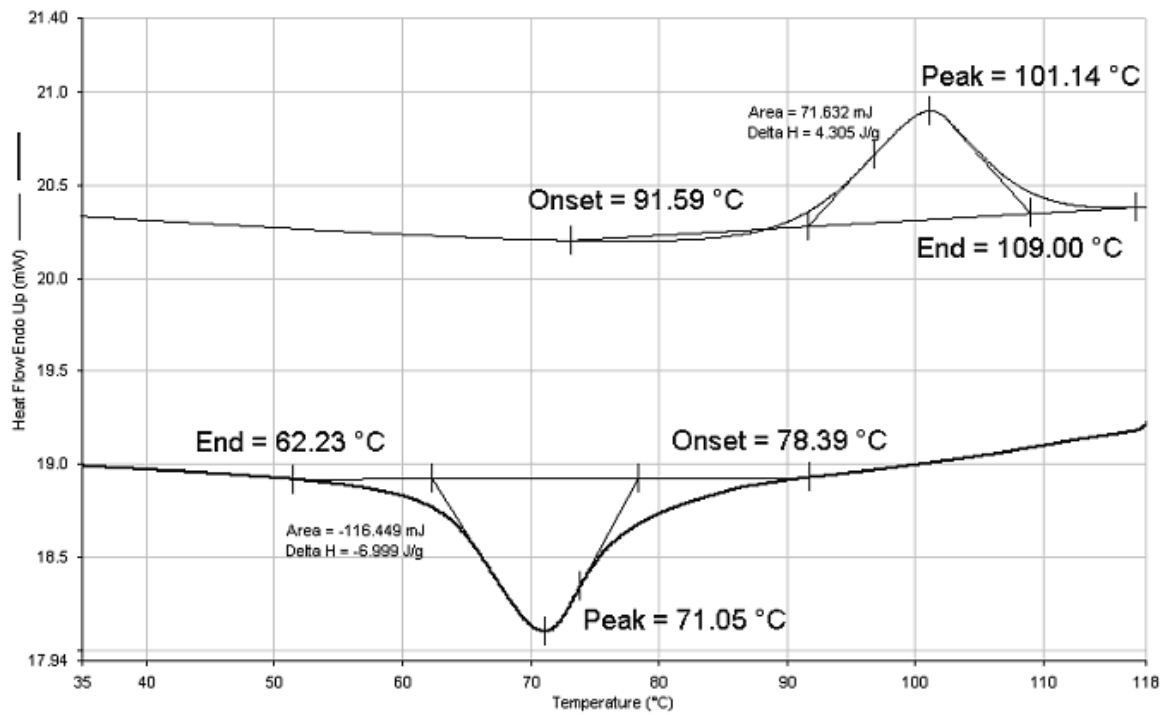
Fig. B-3. DSC results from as-HIPed sample(3).
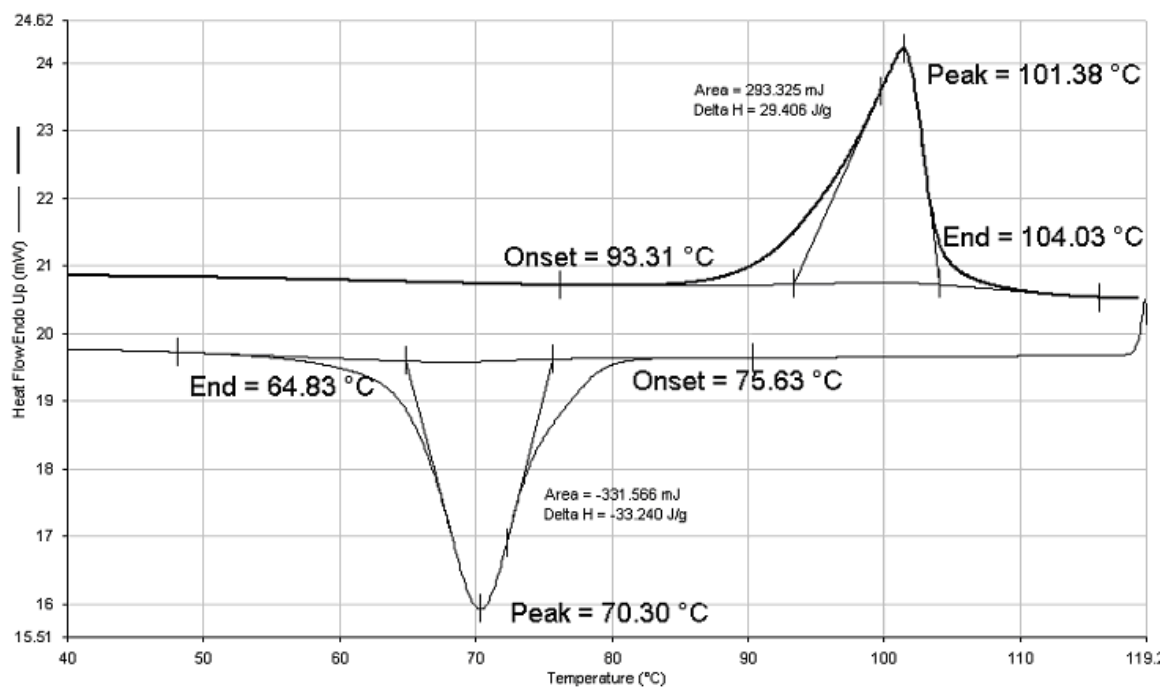
Fig. B-4. DSC results from sample after long solution heat treatment.
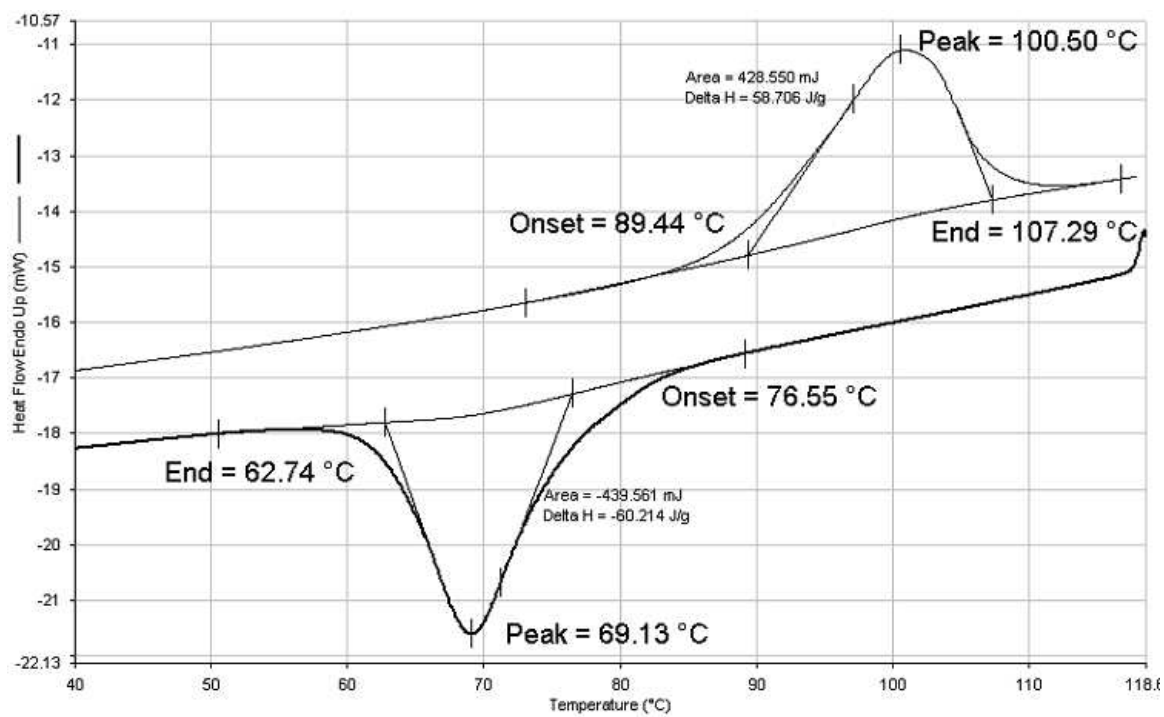
Fig. B-5. DSC results from sample after long solution heat treatment(2).
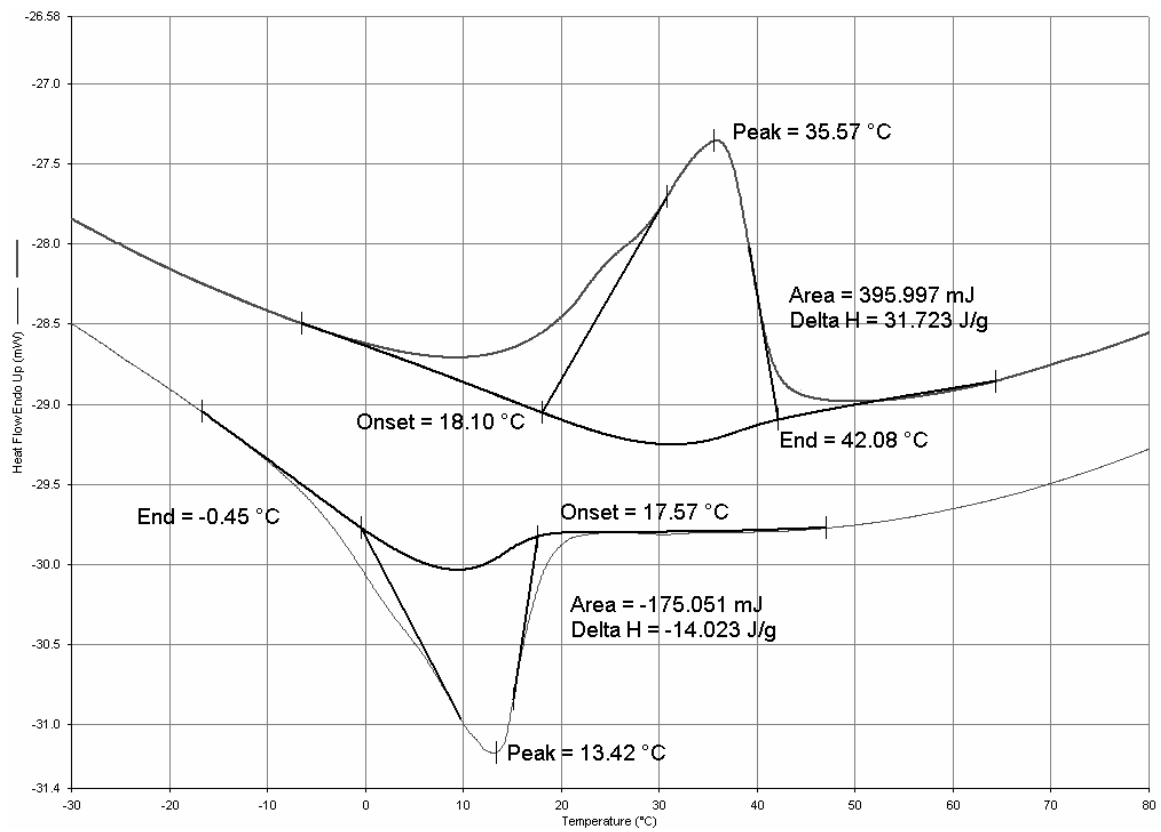
Fig. B-6. Anomalous DSC results from sample after a long SHT.

APPENDIX C

ADDITIONAL MECHANICAL TESTING RESULTS

This appendix contains additional mechanical testing results. As pseudoelastic performance was the limiting factor in this work, many tests were run at high temperature. As such, few SME tests were performed and all reportable SME testing results were presented in the main body of this work.

The sample tested in Figs. C-1 and C-2 had an aspect ratio of 2.5 and porosity of 40%. There was no treatment between the first test and the second test. The obvious break in data in Fig. C-1 was caused by a load cell failure after which the test was continued with a load cell of different capacity. Figs. C-3, C-4, C-4 and C-5 were performed on a solutionized, fully trained sample with an aspect ratio of 1. The change in aspect ratio from the previous sample is due to material availability. Between the second and third test on this sample a thermal treatment was performed and a reduction in strain recovery was observed. Figs. C-7, C-8, C-9, and C-8 were performed on a solutionized sample with an aspect ratio of 1. Training was performed between tests and is noted in the captions.
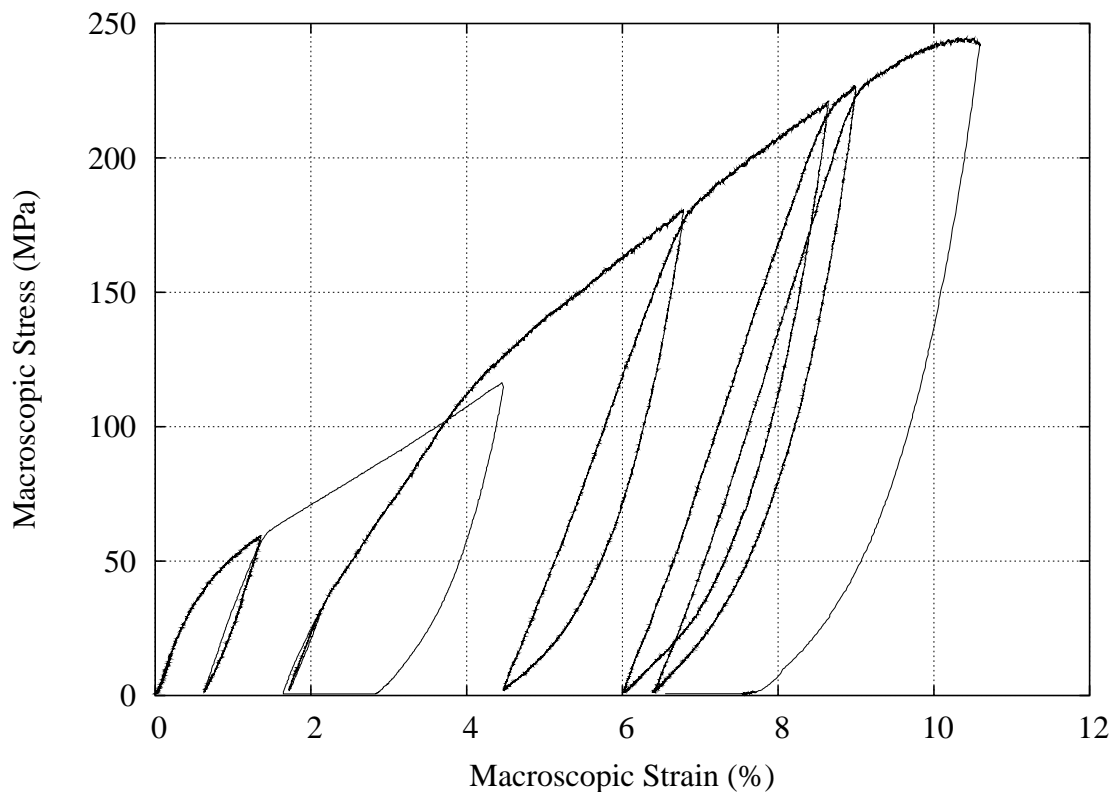
Fig. C-1. Stress-strain plot from pseudoelastic testing of a sample after short heat treatment. Test temperature was 112°C, A_f was 110°C.
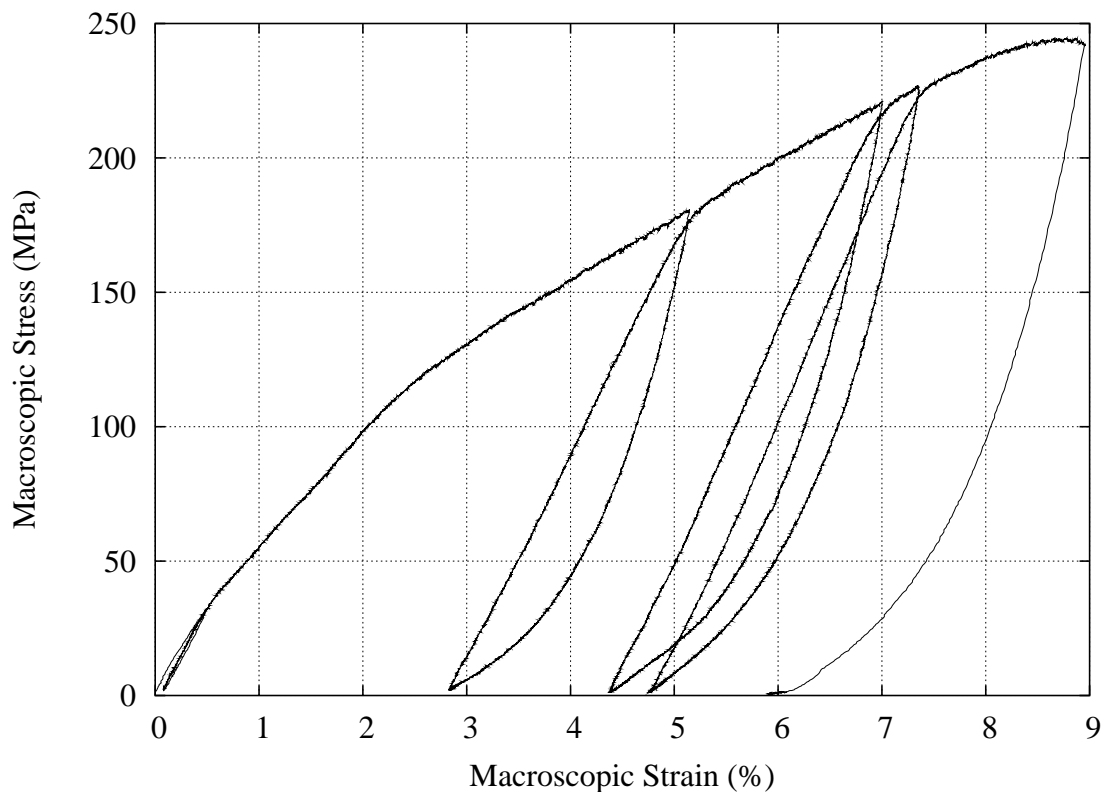
Fig. C-2. Stress-strain plot from second pseudoelastic testing of a sample after short heat treatment. Test temperature was 112°C, A_f was 110°C.
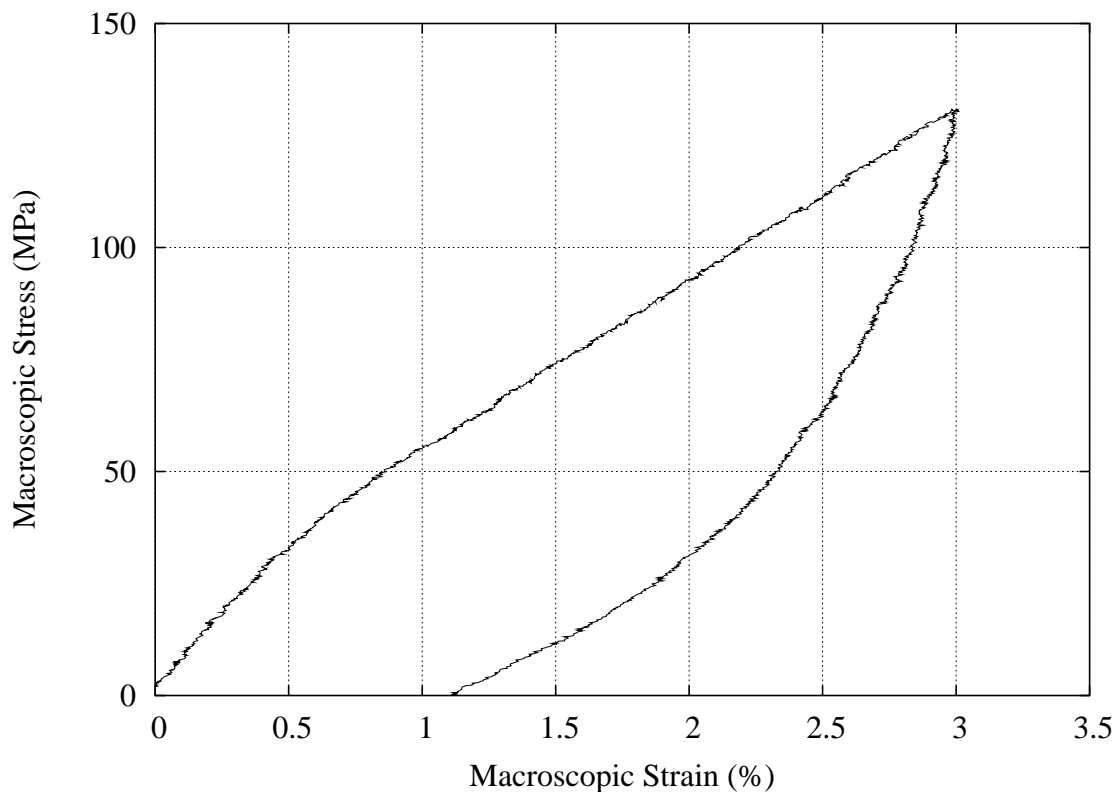
Fig. C-3. Stress-strain plot from pseudoelastic testing of a sample with long heat treatment after training. Test temperature was 112°C, A$_f$ was 105°C.
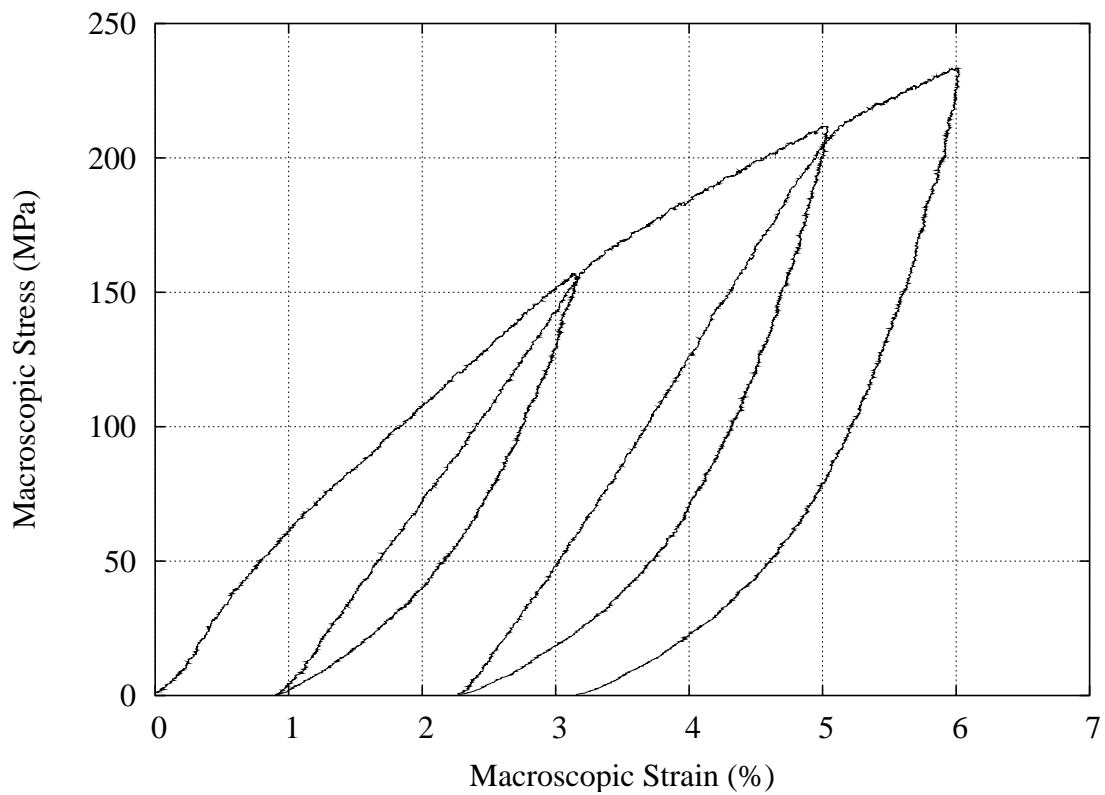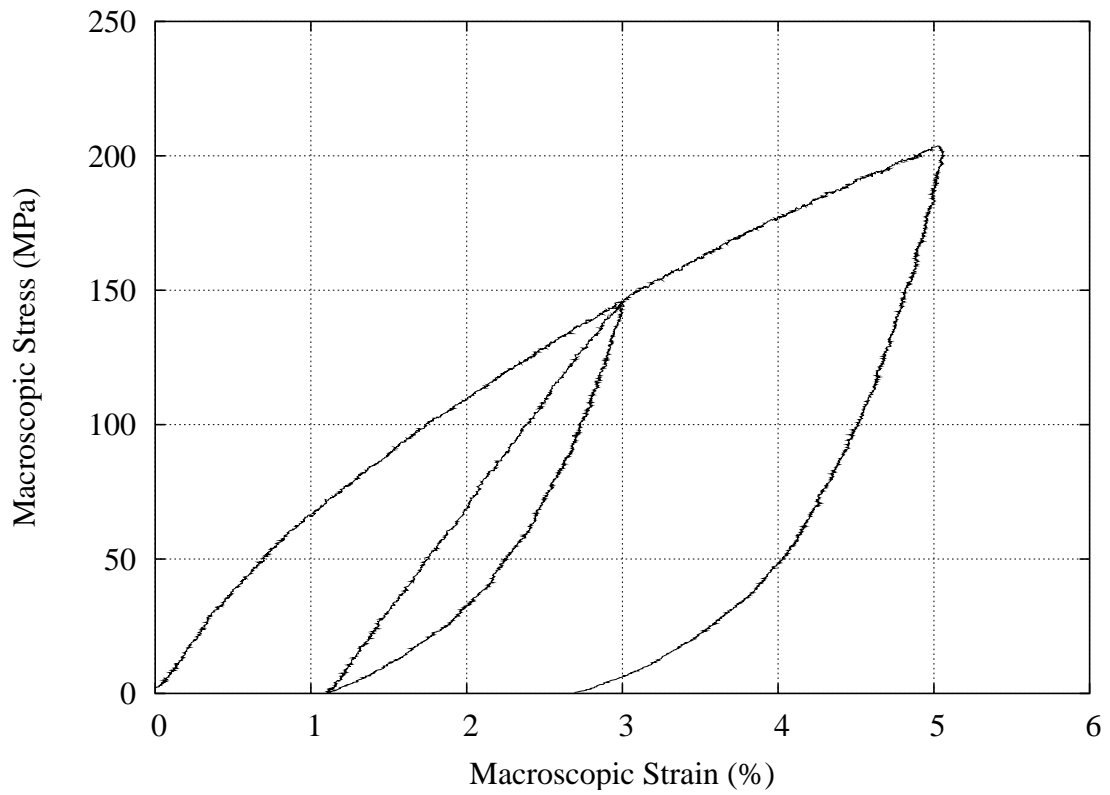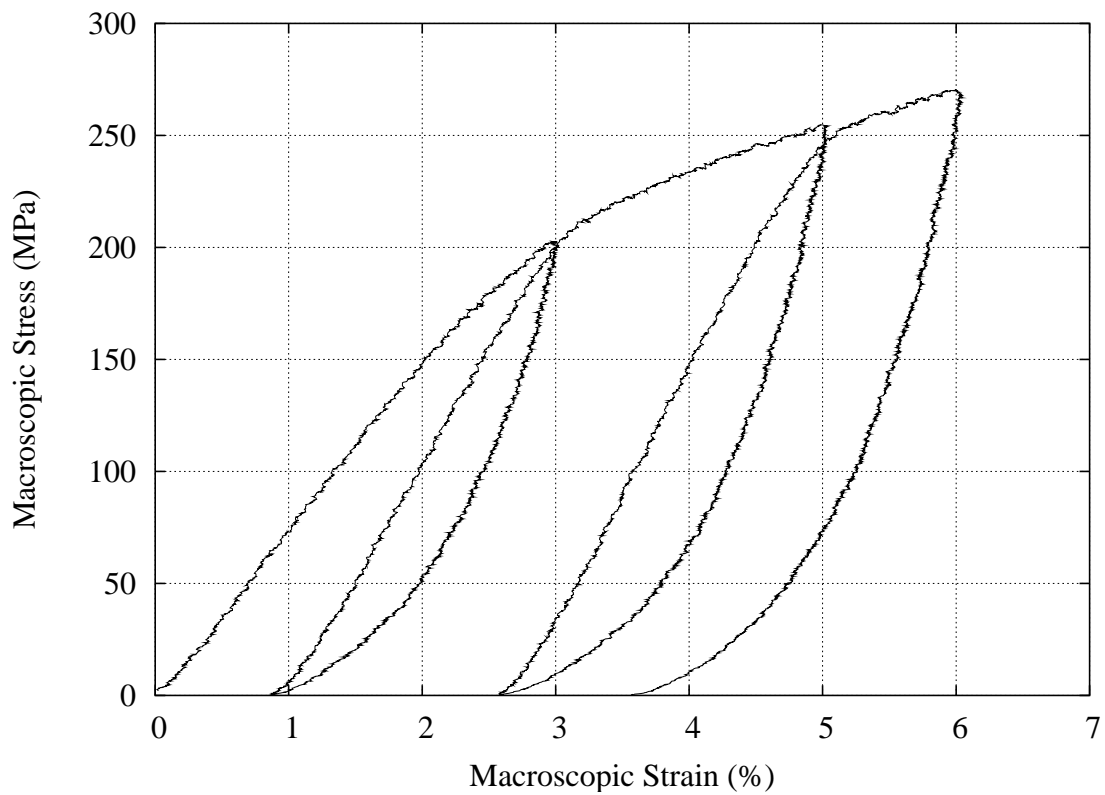
Fig. C-4. Stress-strain plot from second pseudoelastic testing of a sample with long heat treatment after training. Test temperature was 120°C, A_f was 105°C.

Fig. C-5. Stress-strain plot from third pseudoelastic testing of a sample with long heat treatment after training and thermal treatment. Test temperature was 120°C, A_f was 105°C.

Fig. C-6. Stress-strain plot from fourth pseudoelastic testing of a sample with long heat treatment after training and thermal treatment. Test temperature was 140°C, A_f was 105°C.

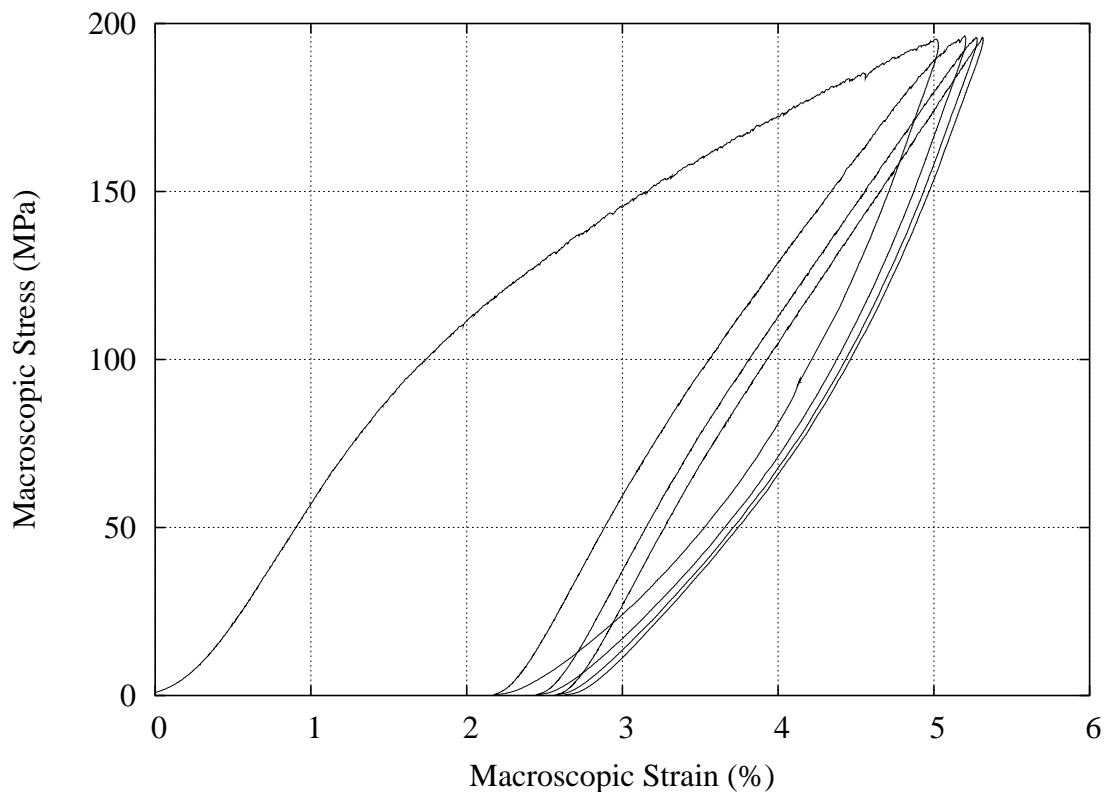Fig. C-7. Stress-strain plot from first pseudoelastic testing of a sample with long heat treatment. Test temperature was 120°C, A$_f$ was 105°C.
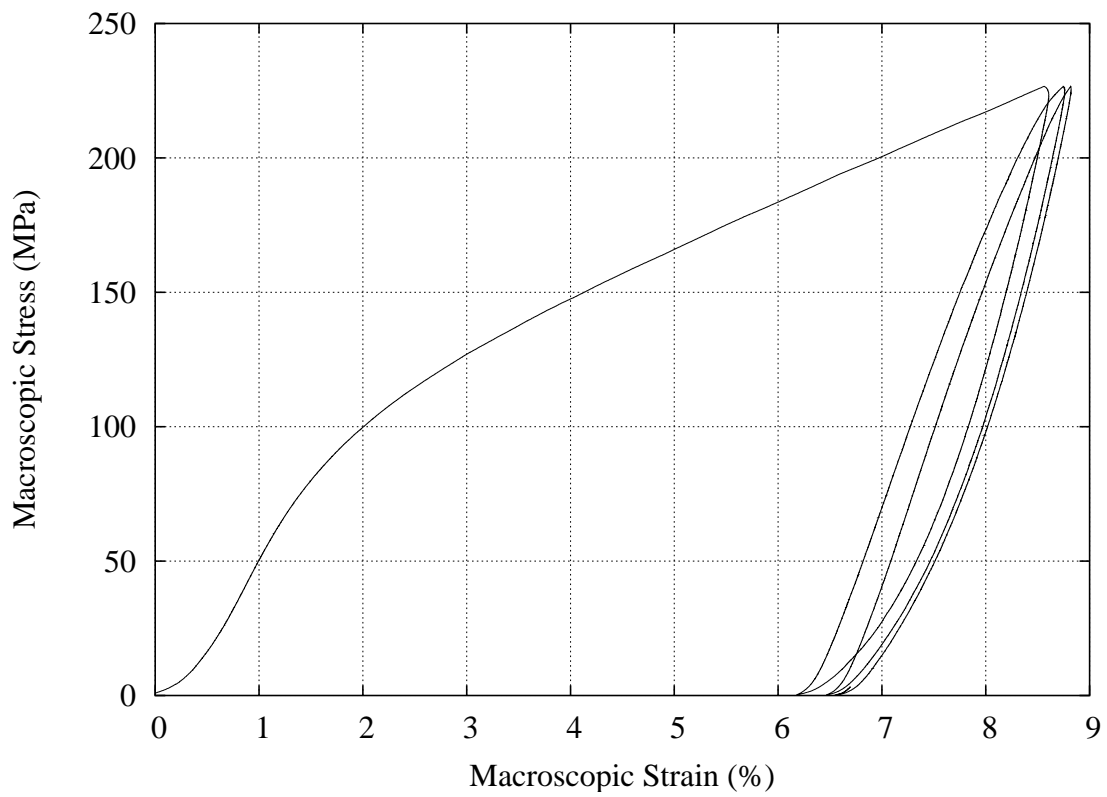
Fig. C-8. Stress-strain plot from pseudoelastic testing of a sample with long heat treatment after heating to 500°C for 0.5hr. Test temperature was 120°C, A_f was 105°C.
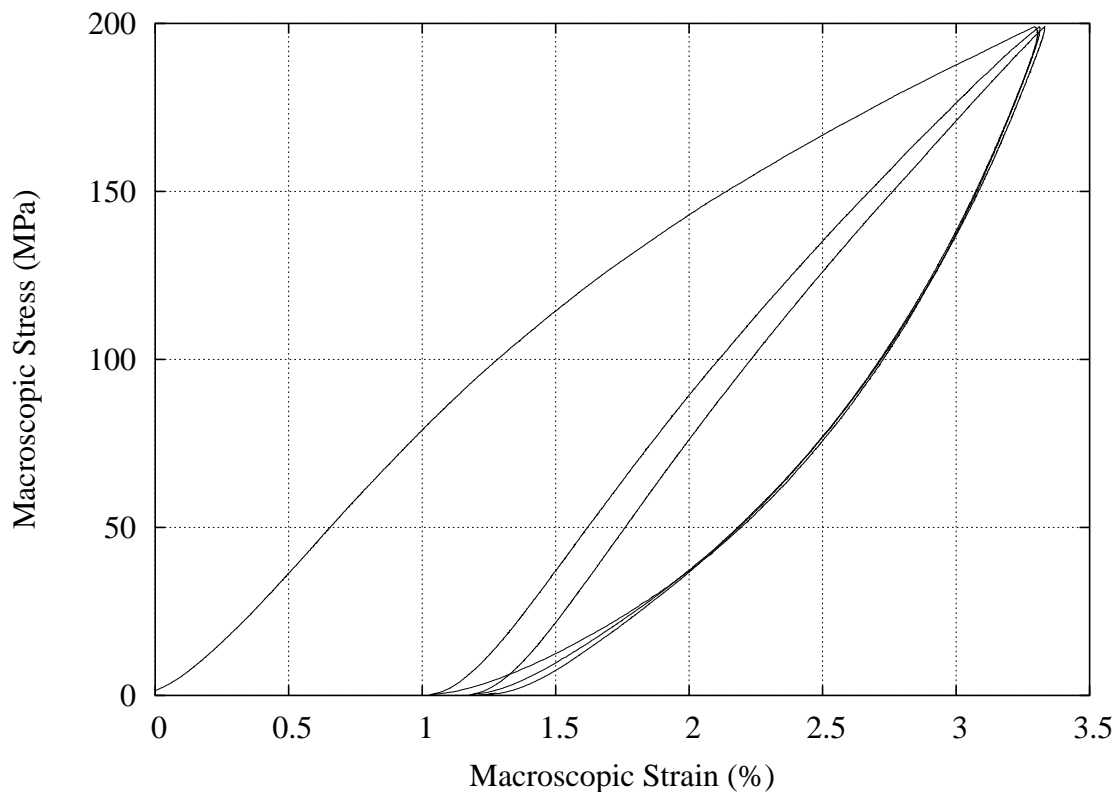
Fig. C-9. Stress-strain plot from second pseudoelastic testing of a sample with long heat treatment after heating to 500°C for 0.5hr. Test temperature was 140°C, A_f was 105°C.
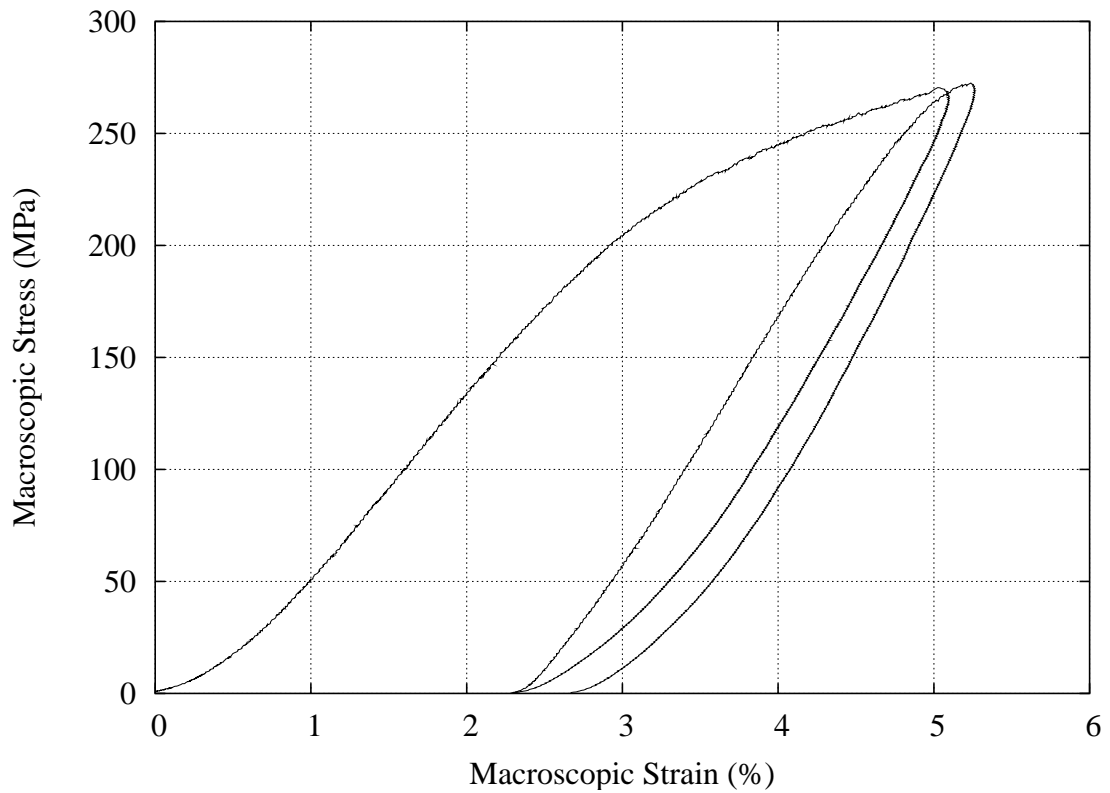
Fig. C-10. Stress-strain plot from pseudoelastic testing of a sample with long heat treatment after heating to 500°C for 0.5hr and training. Test temperature was 175°C, A_f was 105°C.

VITA

Luke Edward Penrod is the second son of Susan and Michael, and the only brother of Sean. He was raised in San Antonio, Texas. After graduating high school, Luke attended Texas A&M University and completed a B.S. in aerospace engineering in August of 2001. Later that month he continued his education in the same department. Upon completion of his degree, Luke will begin his career with Lockheed Martin Aeronautics Company in Ft. Worth, Texas. His permanent address is:

Luke Penrod

22959 Central Prairie

San Antonio, TX 78255

This document was typeset in LaTeX 2_ε by Luke Penrod.